The University of Osaka
Institutional Knowledge Archive

| Title | Nuclear structure study of heavy actinides via Coulomb excitation of the heaviest target 254Es |
|---|---|
| Author(s) | Pham, Thanh Tung |
| Citation | 大阪大学, 2023, 博士論文 |
| Version Type | VoR |
| URL | https://doi.org/10.18910/93020 |
| rights | |
| Note | |

*The University of Osaka Institutional Knowledge Archive : OUKA*

https://ir.library.osaka-u.ac.jp/

The University of Osaka

Osaka University

Doctoral Thesis

# Nuclear structure study of heavy actinides via Coulomb excitation of the heaviest target $^{254}$Es

*Author:*

Pham Thanh Tung

*Supervisor:*

Prof. Ideguchi Eiji

Research Center for Nuclear Physics

Graduate School of Science

August 31, 2023

# *Abstract*

Exploring the new elements toward the high end of the nuclear chart is one of the most interesting topics in nuclear physics. A long-lived Super Heavy Elements region with proton and neutron number near Z = 114, Z = 120, N = 184 – the so-called "island of stability" (IoS) is predicted to be one of the most promising regions in the nuclear chart still left to be discovered. Currently, the access to the IoS is limited because of very low cross sections with the present experimental techniques. Single-particle orbitals neighboring the deformed shell gaps in the actinide region with Z around 100 and N around 152 are predicted to be linked to the spherical shell in the IoS region. This provides the ability to elucidate the shell structure of the nuclei on the island of stability.

$^{254}$Es (einsteinium-254, Z = 99, N = 155) is an isotope in deformed shell gaps region and currently the heaviest target available for Coulomb excitation experiment. Studies in the region of deformed shell gaps can link to the shell structure of nuclei in the IoS. The "safe" $^{254}$Es Coulomb excitation experiment has been performed for the first time at the JAEA-Tokai Tandem accelerator using a $^{58}$Ni beam with an energy of 250 MeV. The scattered particles are detected by two CD-silicon detectors placed backward and forward to the target in coincidence with $\gamma$ rays detected by an array of $\gamma$-ray detectors.

Several new transitions of $^{254}$Es were observed, indicating a rotational band structure. The analysis of the new data permitted us to extended the $^{254}$Es level scheme. From the transition energies and spins, the moment of inertia of the ground-state band of $^{254}$Es was calculated. From the $\gamma$-ray yields, in conjunction with previously measured spectroscopic data, the electromagnetic matrix elements of the transitions are determined, using the couple channel least-squares search code, GOSIA. From these determined matrix elements, the quadrupole deformation of $^{254}$Es was determined to be $\beta_2 = 0.28^{+0.07}_{-0.05}$.

The magnitude and the evolution of the moment of inertia as the rotational frequency increases, were evaluated. The quadrupole deformation result was compared

with the deformation deduced from a very recent laser spectroscopy experiment and discussed in the systematics of the deformation of the heavy actinide nuclei. The results of moment of inertia and the quadrupole deformation were also compared with the calculations by the cranked relativistic Hartree - Bogoliubov theory (CRHB + LN(NL1)). The deformation of $^{254}$Es was applied into a single-particle energy diagram, which was calculated from the momentum dependent Wood-Saxon potential, in order to determine the ground-state configuration of $^{254}$Es and pinpoint the single-particle orbitals around Z = 100 and N = 152.

The results of the excited states and deformation of $^{254}$Es help to assign the configuration of $^{254}$Es and improve the current knowledge of single-particle orbitals in the actinide region. This new information is valuable in making more reliable predictions of the nuclear structure in the island of stability.

# *Acknowledgements*

I am immensely grateful to all those who have supported and guided me throughout my Ph.D. journey, enabling me to reach this significant milestone. Their unwavering assistance, encouragement, and understanding have been invaluable.

I am profoundly grateful to my supervisor, Professor Eiji Ideguchi, and my second guidance, Dr. Riccardo Orlandi, for giving me the opportunity to work on this exciting experiment. Their expertise, patience, and commitment have been essential in forming the direction of my research. Furthermore, they have been of great help to me with everyday matters, such as accommodation, phone number, and insurance, etc., which may seem insignificant but have been of great assistance during my stay and studies in Japan.

I am indebted to the Research Center for Nuclear Physics (RCNP), Osaka University and the Advanced Science Research Center (ASRC), JAEA for providing me with the platform and resources to pursue my Ph.D. Their excellence and fostering of an academic and scientific environment have been essential to my growth as a researcher. During my Doctoral course, I have received unwavering support from colleagues from the experimental group at RCNP and the Erotic Heavy Element group at ASRC: Professor Aoi, Dr. Nishio, Dr. Kumar, Ha san, Kohda san, Dr. Makii, Dr. Hirose, Dr. Suzaki and many others, especially when I conducted the experiment for this thesis, during the difficult times of the coronavirus pandemic.

It would be remiss if not to acknowledge the JAEA Special Research Student Program for their generous financial support, which has allowed me to focus on my research without the burden of financial constraints. Their support in my education has been a critical factor in the completion of this endeavor.

Finally, I extend my gratitude to all individuals who contributed to my academic journey – whether through insightful discussions, technical assistance, or paper work support. Your collective contributions have made this achievement possible.

In conclusion, this thesis stands as a testament to the collaborative efforts and unwavering support of many individuals. While it is not possible to acknowledge everyone by name, please know that your impact on my journey is greatly appreciated.

Thank you all for being an integral part of my Ph.D. expedition.

PHAM THANH TUNG

# Contents

# Chapter 1

# Introduction

## 1.1 History of heavy elements

Since the early times of modern chemistry and physics, the search of new elements has been one of the most motivating topic among the research community. Elements up to Uranium (Z = 92), except Technetium (Z = 43), are present, although some of them in very small quantities, in nature, while elements heavier than Uranium were produced by artificial methods. Furthermore, a region of long-lived, possibly stable nuclei in the upper-right end of the nuclear chart is predicted by several models [1], the so-called 'island of stability' (IoS).

Since the 1940s, the development of nuclear reactors and ion accelerators as well as the vast improvements in detection methods and measurement techniques led to the discovery of many new elements beyond Uranium. Although there is no universally accepted definition for their classification, elements with Z = 93 ~103 are usually referred to as heavy actinides or "very heavy" elements (VHE). Heavier elements with Z $\geq$ 104 are normally called superheavy elements (SHE). Elements heavier than uranium were synthesized using various types of reactions: neutron capture, multi-nucleon transfer or fusion reactions.

The elements from Neptunium (Z = 93) to Fermium (Z = 100) can be synthesized in a high neutron flux reactor. Through the consecutive neutron capture and $\beta^-$ decay processes, the seed nucleus (i.e., Uranium) raises its mass and atomic number. The path towards larger proton numbers stops at Fermium, as it does not $\beta^-$ decay into Z

= 101. The heaviest elements were synthesized using fusion reactions. Elements from Mendelevium, Z = 101 up to Seaborgium, Z = 106, were produced by fusion reaction between a light-ion projectile (e.g $^{12}C$, $^{18}O$). Six elements from Bohrium (Z = 107) to Nihonium (Z = 113) were produced by the "cold fusion" reaction using lead or bismuth as targets where only one or two neutrons are emitted in the reaction. It is different from the more recent "hot fusion" method, which results in a higher excitation energy of the compound system. In the hot fusion reactions, deformed actinide targets have been irradiated so far by a $^{48}Ca$ beam. The final nucleus is obtained after the emission of 3 to 6 neutrons from the highly excited compound nucleus. This reaction has been used to synthesize elements up to Oganesson (Z = 118). Figure 1.1 shows the currently known isotopes in the upper end of the nuclear chart. The region appearing in darker shades of blue on the top-right region of the Figure 1.1 roughly corresponds to the IoS. Further explanations and discussion of the IoS will be introduced in the next section.

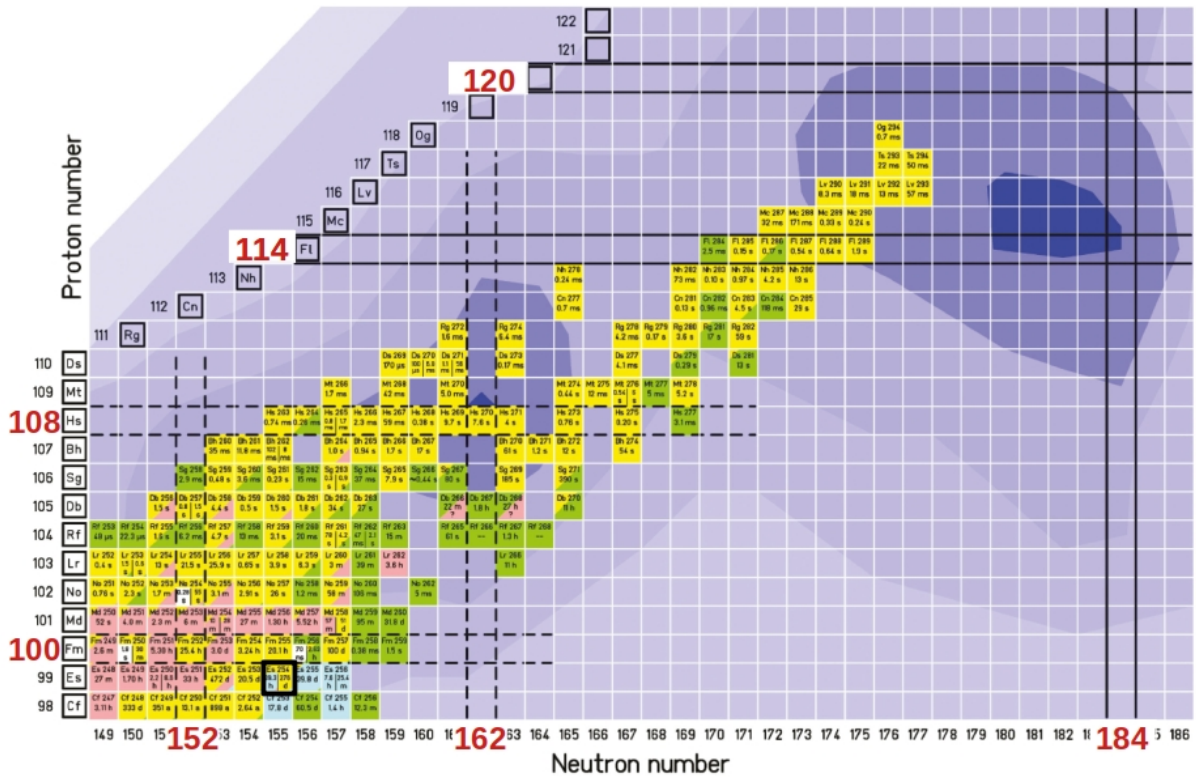


FIGURE 1.1: Upper end of the chart of nuclei showing the experimentally known nuclei. Colors correspond to their decay mode: $\alpha$-decay (yellow), electron-capture decay (red), $\beta^-$-decay (blue), spontaneous fission (green), and $\gamma$-decaying isomers (white). Proton numbers Z = 114, 120 and neutron number N = 184 are emphasized. At these magic numbers, the shell model predicts closed spherical shells or subshells, respectively. The bold dashed lines highlight proton numbers 100 and 108 and neutron numbers 152 and 162. Nuclei with that number of protons or neutrons are deformed, which increased stability. The background structure shows the calculated ground-state shell-correction energy in steps of 1 MeV from -7 MeV (dark blue) to -3 MeV (light blue) according to the macroscopic-microscopic model [2, 3]. The hypothetical spherical superheavy nuclei region, named 'island of stability' is clearly visible. The location of $^{254}$Es isotope, which is the target of this thesis, is also highlighted. Figure modified from [4]

## 1.2 Where is the island of stability?

Shell effects are strongest at certain numbers of protons and neutrons, known as "magic numbers". Currently, the largest known magic numbers are those of doubly magic $^{208}$Pb (Z = 82, N = 126). Since the 1960s, it was predicted that a region of stable, or nearly stable, nuclei could be found in proximity of the next magic numbers. These predictions started the theoretical and experimental quest for the IoS.

Early calculations of the SHE region were made using the modified oscillator potentials [5, 6, 7, 8] and of the Woods–Saxon potential [9, 10, 11]. These calculations predict Z = 114, N = 184 as spherical magic numbers.

Mean-field calculations treat nucleons as individual particles that move independently in a potential created by other nucleons. Effective forces were developed since the 1950s, like relativistic mean field (RMF) derived from meson field by Duerr [12] or the Skyrme force [13]. The 'self-consistent' calculation have been implemented by Vautherin et al. in 1970 [14, 15]. Several self-consistent mean-field calculations have been performed in the 1970s in the SHE region. These calculations were only performed for a limited number of isotopes, and in particular for $^{298}_{184}114$, simplified without pairing and for spherical nuclei only. Although some of them suggested other gaps at Z = 120, 126 or 138, these calculations initially did not really cast doubt on the magicity of $^{298}_{184}114$ [1]. In the early 1980s, RMF calculations were also made for $^{298}_{184}114$ [16, 17]. However, calculations using a Gogny force using finite range interaction in 1996 [1], predict that Z = 114 is not a magic number. There were more detailed calculations in the mid 1990s with the increased availability of spectroscopic data and computational power. In a seminal paper, Ćwiok et al. [17] performed systematic calculations using the SkP and SLy7 Skyrme forces. According to these calculations, the next magic numbers are Z = 126 and N =184 while the alleged magic gap at Z = 114 does not show up.

In general, models based on the Skyrme or Gogny interaction favor the spherical magic numbers Z = 126, N = 184, while those based on RMF force favor Z = 120 and N = 172 and the phenomenological potential calculations predict Z = 114, N = 184 [1]. According to some models, the magic character of the SHE region is predicted not to be confined to a single nucleus as in the case of $^{208}$Pb or in lighter doubly magic nuclei, but spread in a wider region. Therefore, the island of stability would therefore exhibit rather soft or washed out limits. It has been also suggested that the presence of several proton gaps in the single-particle diagrams could be interpreted as a magicity spread across Z = 114, 120, 126 [18].

The location of the island of stability is still uncertain since it cannot yet be reached experimentally, and model predictions show the large discrepancies. Fortunately, some excited states in the nuclei in the region of deformed heavy actinide are built on substates of the same orbits which are connected to the rise of the spherical shell gaps in the IoS. This link between heavy actinides and the IoS is further explained in the next section. Thus, the spectroscopy of these deformed nuclei, which are much more accessible, can help to obtain more reliable predictions of the island of stability.

## 1.3 The link between the heavy actinide region and the IoS

In the region of heavy actinides, the shape of nucleus is found to deviate from sphericity. Several experiments indicate that most heavy actinides are prolate deformed. In turn, due to deformation, the nucleon orbits split into several substates, with a significant rearrangement of the orbital orderings. Another consequence is that energy gaps appear near Z = 100, 108 and N = 152, 162. These gaps, in spite of the much smaller size (about 10-15%) compared to the spherical shell gaps, at Z = 82 or N = 126, significantly enhance the stability of isotopes in their proximity, by effectively increasing the fission barrier. For this reason, they are usually referred to as deformed shell gaps.

The first experimental evidence for a shell at N = 152 was discussed in a paper published in 1954 by Ghiorso et al., based on systematics of $\alpha$-decay energies [21]. The more recent results of $\alpha$-decay energies are plotted in Figure 1.2. This figure shows that the value of $Q_\alpha$ is lower for several isotopes at N = 152 and N = 162, indicating the shell effect at these neutron numbers. Other manifestations of Z = 100 and N = 152 shell gap were also found in the systematics of the spontaneous fission lifetime or two-nucleons separation energy. The N = 152 and Z = 100 deformed shell gaps arise as a consequence of nuclear deformation. As presented in detail in the following paragraph, these gaps can be explained in the framework of the deformed shell model based on a modified oscillator potential developed by Nilsson [22].

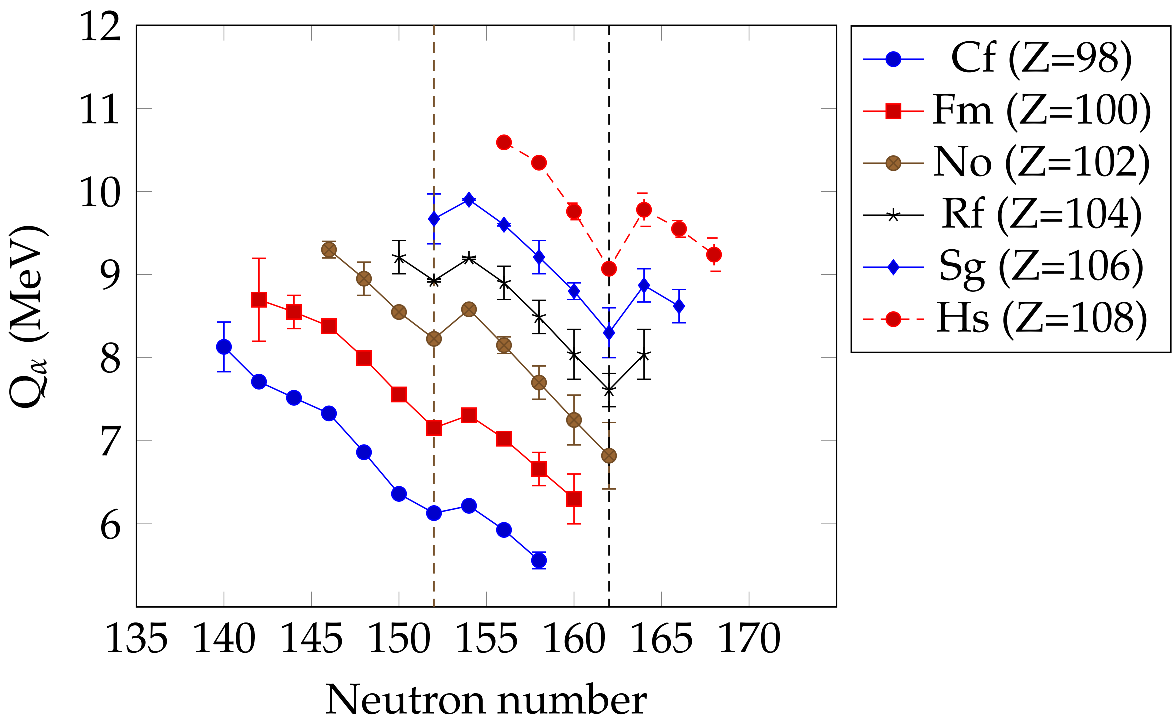


FIGURE 1.2: $Q_\alpha$ values for even-even isotopes from Californium (Z = 98) to Hassium (Z = 108). The dashed vertical lines correspond to the deformed subshell N = 152, 162. Data are taken from [19] and ENSDF database [20]

As a consequence of the deformed potential, the spherical single-particle orbits of spin j are split into $(2j + 1)/2$ orbits, whose energy can either increase or decrease as a function of deformation (see Fig. 1.3, 1.4). In axially symmetric nuclei, the projection of the nucleon orbital angular momentum j on the symmetry axis becomes a good quantum number, Ω. The down-sloping orbitals with a small Ω concentrate mainly along the symmetry axis, which results in a driving force towards prolate shapes. Conversely, up-sloping orbitals have a large Ω concentrate mainly in a plane perpendicular to the symmetry axis, driving oblate deformation. The crossing and reorganization of orbits as a function of deformation in some cases gives rise to relatively large energy gaps among neighboring orbits, generates new shell gaps. As shown in Figures 1.3 and 1.4, for a deformation parameter of approximately 0.3, gaps can be observed at Z = 100 and N = 152.

An interesting feature of deformed nuclei near Z = 100, N = 152 is that their structure involves down-sloping Ω orbitals which originate from the spherical shell gap of superheavy elements. For instance, the neutron $h_{11/2}$, $k_{17/2}$ orbitals have often been

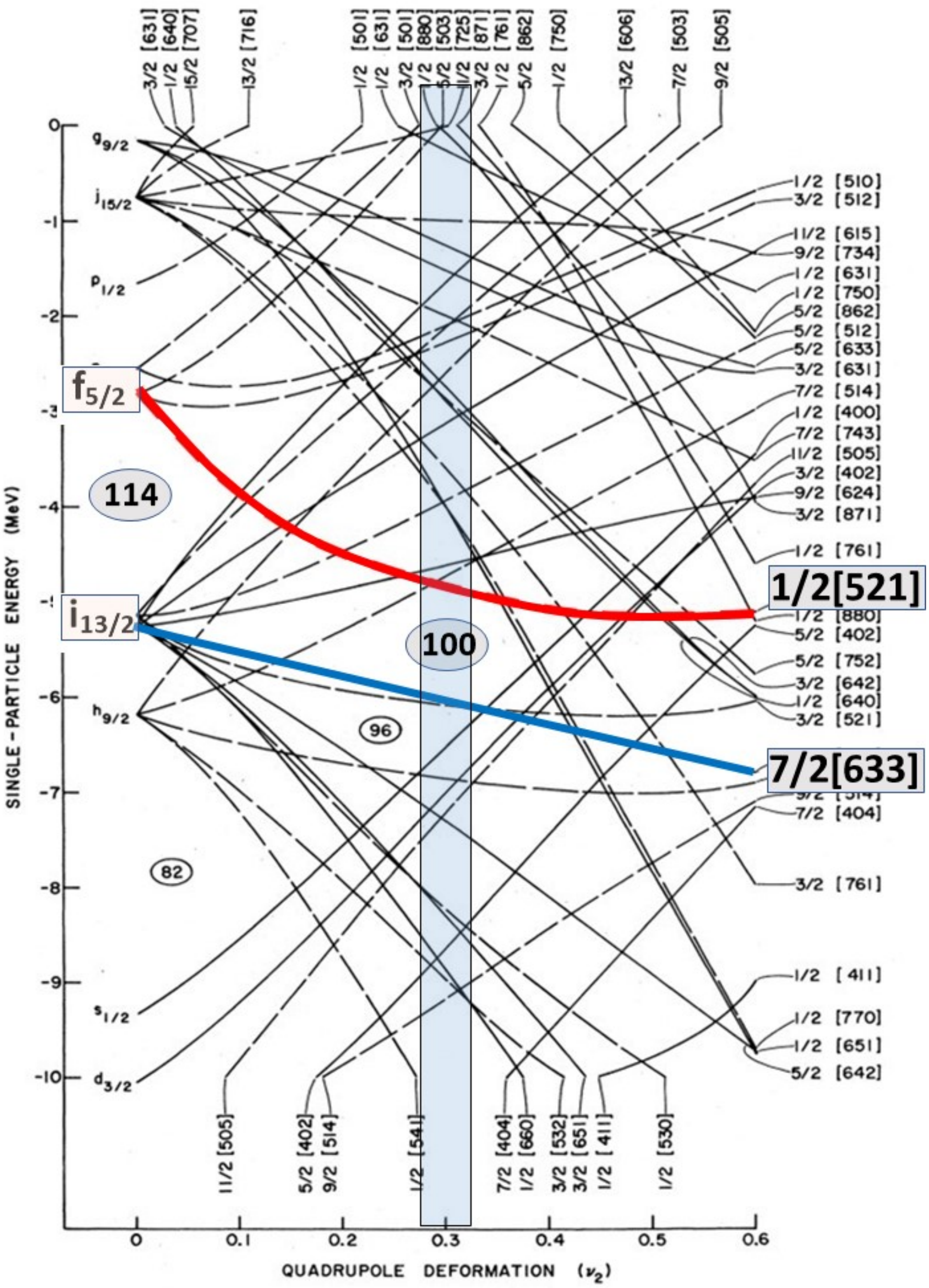


FIGURE 1.3: Proton single particle level of actinides obtained from momentum dependent Woods-Saxon potential as a function of quadrupole deformation. Proposed spherical shell gap at Z = 114 and deformed shell gap at Z = 100 are indicated. The red curve in the figure corresponds to $vf_{5/2}$ orbital supposed to associate with the Z = 114 shell gaps. The blue curve corresponds to $vi_{13/2}$ orbital, which has been suggested to be the location of the odd-proton in the ground-state configuration of $^{254}$Es p : 7/2[633] $\otimes$ n : 7/2[613]. The shaded blue part indicates the deformation of isotopes in the region around Z = 100. Figure taken from [23].

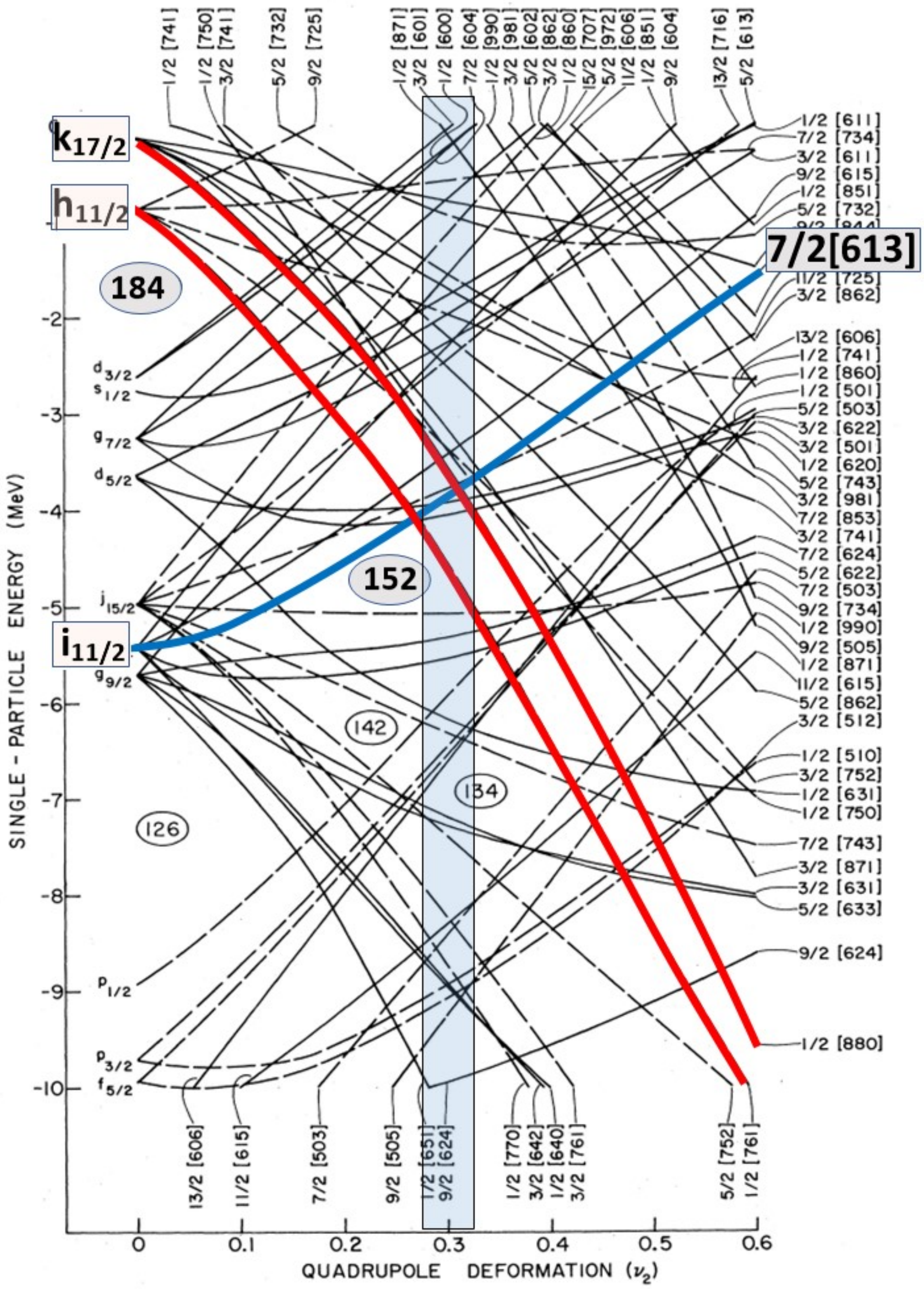


FIGURE 1.4: Neutron single particle level obtained from momentum dependent Woods-Saxon potential as a function of quadrupole deformation. The predicted spherical shell gap at N = 184 and deformed shell gap at N = 152 are indicated. The red curves correspond to $\pi h_{11/2}$, $\pi k_{17/2}$ orbitals. The blue curve corresponds to $\pi i_{11/2}$ orbital that which has been suggested to be the location of the odd-neutron in the ground-state configuration $^{254}$Es p : 7/2[633] $\otimes$ n : 7/2[613]. The shaded blue part indicates the deformation of isotopes in the region around N = 152. Figure taken from [23].

associated with the N = 184 spherical shell gap while the spin-orbit partner $2f_{5/2}$ is of particular interest since in some models their spin-orbit split corresponds to the size of the Z = 114 gap, (as highlighted in Figure 1.3). These orbitals have a significant effect on the shell corrections of superheavy nuclei, and it is thus important to try to locate their positions in spherical nuclei. Strongly down-sloping substates stemming from these orbits at sphericity are expected to appear near the Fermi surface of nuclei near Z = 100 and N = 152. Examples of these substates, such as the neutron $h_{11/2}$ $1/2^-[761]$, $k_{17/2}$ $1/2^+[880]$ and proton $f_{5/2}$ $1/2^-[521]$ orbitals, are highlighted in Figure 1.3. Therefore, the spectroscopy of neutron-rich actinides provides a key data for more reliable extrapolations to the IoS, providing hints of the shell structure of the heaviest spherical nuclei. The structure data of heavy actinides can be extracted to test different theoretical models. Some of the most important quantities to benchmark different models are the energies and spin-parities of excited states, and nuclear deformation.

The ground-state deformation can be deduced from the reduced E2 transition probability, B(E2) of the (I $\rightarrow$ I+2) transition (I is the ground-state spin), or the lifetime of the (I+2) state ($2^+$ state for even-even nuclei). The B(E2) values are usually measured via a "safe" Coulomb excitation method, with beam energy well below the Coulomb barrier. The advantage of this method is that the reaction process can be treated as purely electromagnetic, and it enables the usage of the well-established theory of electromagnetism. Therefore, the transition probability can be measured precisely, independent of a particular nuclear model. In the heavy actinide region, E2 transition probabilities and the lifetime of the first-excited $2^+$ state have been measured for only 10 even-even isotopes: $^{238,240,242,244}$Pu, $^{240,244,246,248}$Cm, $^{250,252}$Cf [24]. There is no available data for odd-A or odd-odd isotopes. This is unfortunate, since the nuclear structure of non-even-even nuclei is strongly affected by the specific orbitals occupied by the unpaired nucleon(s), which makes these nuclei very useful systems to obtain information on the underlying orbitals. Furthermore, improving the data about deformation in the heavy actinide region would help to complete picture of nuclear structure in this region.

The focus of this Ph.D. thesis is the nuclear structure study of $^{254}$Es (Z = 99, N = 155) via Coulomb excitation. The new data on $^{254}$Es, and comparison with the systematics of other heavy actinides, will promote a deeper understanding of deformed, neutron-rich nuclei, in order to move a small step closer to the island of stability.

## 1.4 Studies of $^{254}$Es

Einsteinium was first discovered in the hydrogen bomb test in 1952 and currently is only synthesized in high neutron flux nuclear reactor. Experimental information on $^{254}$Es level were obtained from $\alpha$-decay spectroscopy of $^{258}$Fm [25], (see Figure 1.5) which is latter re-evaluated by M. Sainath et al. [26] and very recently, via laser spectroscopy experiment [27].

$^{254}$Es decays with nearly 100% probability by alpha emission, and has a half-life of 275.7(5) days. The ground state spin-parity of $^{254}$Es is assigned to be ($7^+$). Based on the observed ground-state (g.s.) configurations of the odd-proton in $^{253}$Es and the odd-neutron in $^{253}$Cf, the ground-state configuration of $^{254}$Es is suggested to be the coupling of the $i_{13/2}$ $7/2^+$[633] proton with $i_{11/2}$ $7/2^+$[613] neutron [26].

The ground state band is only known up to ($9^+$) with 3 $\gamma$ rays observed: 80.1(2) keV, 91.0(3) keV, 171.1(2) keV. The 80.1 keV $I^\pi$ = ($8^+$) level and the 171.1 keV $I^\pi$ = ($9^+$) level fit with the description as the next two rotational members of the ($7^+$) g.s. band, with the rotational parameter A = 5.0 keV [26]. Only few spectroscopic quantities of this band are known, with quite large uncertainty. The 171.1 keV/91.0 keV relative branching ratio is 100(33)/26(16). The mixing ratio $\delta_{E2/M1}$ of the $(8^+) \rightarrow (7^+)$ (80.1 keV) transition was measured to be 1.25(25). An isomeric state at 84.2 keV was found with life-time 39.3 hours and an assigned spin-parity of $2^+$ [29]. This isomer mostly decays via $\beta^-$ to $^{254}$Fm.

In this work, the ground-state rotational band of $^{254}$Es is investigated using the Coulomb excitation. The energy of the $\gamma$-ray transitions were measured and their reduced transition probabilities B(E2) are determined. Our analysis permits us to determine the moment of inertia and quadrupole deformation of $^{254}$Es, which are key

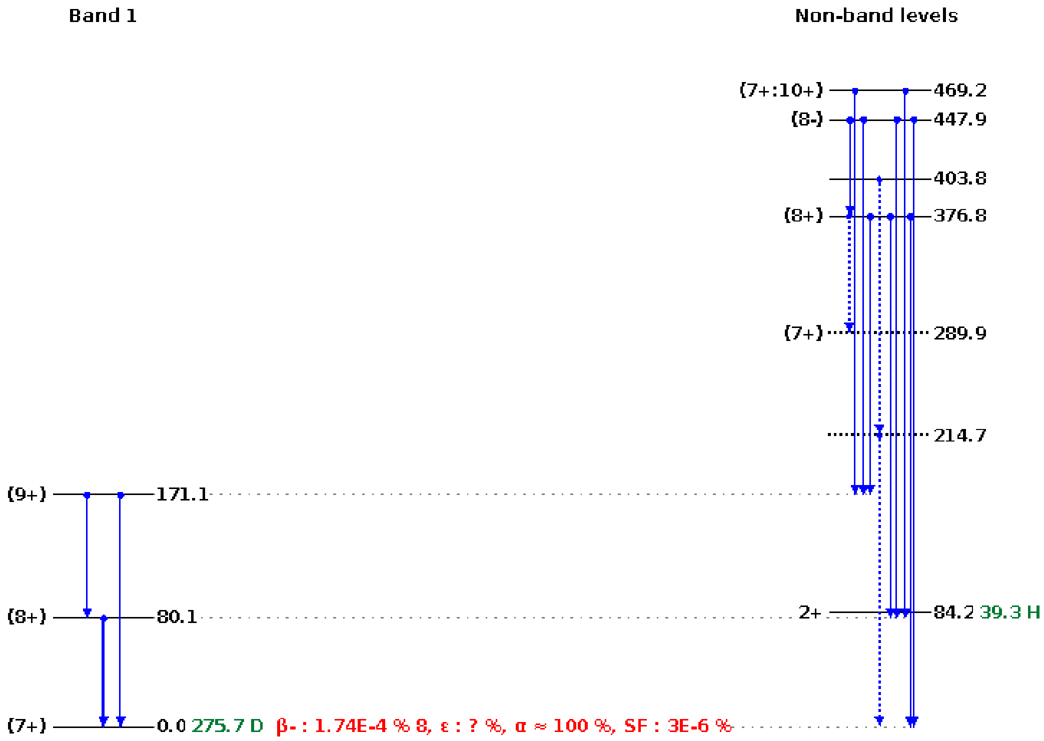


FIGURE 1.5: Level scheme of $^{254}$Es from $^{258}$Md $\alpha$-decay spectroscopy [25, 28].

properties to test theoretical models.

In this chapter, the main topic of this research and its motivation were summarized. The theoretical background is covered in Chapter 2. The experimental technique of Coulomb excitation, as well as a simplified description of the GOSIA analysis code used in this work, are given in Chapter 3. In Chapter 4, the details of the experimental apparatus, including the Einsteinium target, the accelerator, the detector setup and the data acquisition system are introduced. In Chapter 5, the analysis and results of the Coulomb excitation of $^{254}$Es are described. This explanation includes a description of how $\gamma$-ray spectra are generated and calibrated, and how structural information is obtained from these spectra. Chapter 6 discusses the moment of inertia and quadrupole deformation of $^{254}$Es in in relation to the structure of $^{254}$Es and to the structure of nuclei in the region. Finally, a short summary and outlook are given in Chapter 7.

# Chapter 2

# Theoretical background

In this chapter, the essential physics background to this work is given. The first section gives a general introduction to the theoretical models used to describe the properties of heavy and superheavy nuclei. In Section 2.2, nuclear deformation is discussed within the framework of the collective model. Magnetic dipole and electric quadrupole moments are described in Section 2.3.

## 2.1 Nuclear models

In the energy scale of nuclear structure, the atomic nucleus can be approximated to a many-body quantum system composed of protons and neutrons. A simplified, but powerful description of the nucleus is offered by the macroscopic-microscopic model, which combines a collective description of the nucleus as analogous to a liquid drop, with microscopic effects, referred to as shell effects, arising from the quantum mechanical nature of nucleon orbits and their shell structure.

In this section, the shell effects and their contribution to nuclear stability will be described. Different nuclear models are used to reproduce the properties of heavy and superheavy nuclei and to predict the next magic shell closures. The models are shortly introduced in this section, to give the background to understand these calculations and their limitation in predicting nuclear properties.

### 2.1.1 The shell model

The implementation of the atomic shell formalism into the nuclear framework or the spherical shell model, with the spin-orbit coupling term, successfully reproduced the known magic numbers for protons and neutrons.

To describe a nucleus, the Hamiltonian problem described by the time-independent Schrödinger equation, shown in Equation 2.1, has to be solved.

$$H\psi = -\frac{\hbar^2}{2M}\Delta + V(r)\psi, \tag{2.1}$$

where $V(r)$ is the nuclear one-body potential. Instead of describing the nucleon-nucleon interaction and extrapolating the nuclear behavior from this basis, each nucleon can be considered to be immersed in a mean field potential created by all the nucleons. Each nucleon feels the potential independently. Three commonly used potentials are the square-well, harmonic-oscillator, and Wood-Saxon potential, which are shown in figure 2.1. The former two potentials can be solved analytically. However, a more realistic

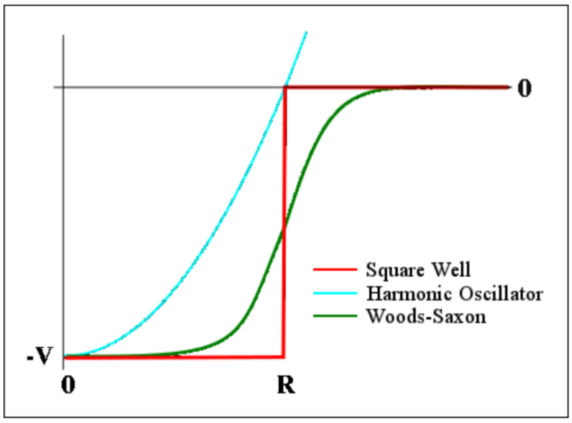


FIGURE 2.1: Shape of the different potentials. The Wood-Saxon potential falls between the infinite and the harmonic oscillator potentials

potential falls in between these two cases, as the potential drops at the surface too fast for the square-well, and too slow for the harmonic oscillator. The Woods-Saxon potential includes the drop of the potential near the surface through the surface diffuseness parameter $a$:

$$V_r(r) = \frac{V_0}{1 + exp\left[\frac{r-R_0}{a}\right]}, \tag{2.2}$$

with $R_0$ is the nuclear radius and $V_0$ is the potential depth.

The Wood-Saxon potential, however, cannot be used analytically in the calculations. The Modified harmonic-oscillator potential was developed to reproduce the results obtained with the Wood-Saxon potential while preserving the possibility of analytic solutions.

### 2.1.2 The Nilsson model

Nuclei with several nucleons outside closed shells are generally deformed (see section 2.2). As a consequence, the nucleons move in an anisotropic potential, and degeneracy of states with the same angular momentum j, but different projection quantum number $m$ is broken. In order to extend the shell model to deformed nuclei, Nilsson introduced a deformed potential in the Hamiltonian. The Hamiltonian takes the following form [22]:

$$V_{AMHO} = \frac{\hbar}{2M}\Delta + \frac{1}{2}M\left[\omega_x^2 x^2 + \omega_y^2 y^2 + \omega_y^2 y^2\right] - C\vec{l}\cdot\vec{s} - D\vec{l}^2. \tag{2.3}$$

where $(x, y, z)$ are particle coordinates in the body-fixed coordinate system. The three different rotational frequencies $\omega_x$, $\omega_y$, $\omega_z$ correspond to the different deformation axes. C and D are constants to specify the strength of the $\vec{l}\cdot\vec{s}$ and $\vec{l}^2$ terms. In the case of axially symmetric nuclei, the oscillator frequencies $\omega_x$, $\omega_y$, $\omega_z$ can be replaced by $\omega_\perp$ and $\omega_z$:

$$\omega_x = \omega_y = \omega_\perp = \omega_0(\epsilon)\left(1 + \frac{1}{3}\epsilon\right). \tag{2.4}$$

$$\omega_z = \omega_0(\epsilon)\left(1 - \frac{2}{3}\epsilon\right). \tag{2.5}$$

The elongation parameter $\epsilon$ gives a measure of the deformation and $\omega_0$ is the oscillator frequency for the spherical harmonic oscillator. The model can be extended to higher multipoles order of deformation.

The energies and eigenfunction can be calculated as a function of deformation $\epsilon$. A plot of single-particle energies versus nuclear deformation is called a Nilsson diagram. In a deformed potential, the necessary quantum numbers are the parity $\pi$ and the projection of the angular momentum onto the symmetry axis $\Omega$. $\Omega$ is the sum of spin and orbital angular momentum projection quantum numbers of the valence nucleons. Nilsson states are normally labeled with the so-called asymptotic quantum numbers:

$$\Omega^{\pi}\left[Nn_z\Lambda\right], \tag{2.6}$$

where N is the principal quantum number, which defines the shells in the spherical case, $n_z$ is the number of nodes of the wave function in the z direction, and $\Lambda$ the projection of the orbital angular momentum onto the symmetry axis.

## 2.2 Deformation and rotational motion

In a simple representation, the nucleus can be regarded as a sphere with isotropic distributions of neutrons and protons. Indeed, some nuclei, and in particular doubly magic nuclei and isotopes in their vicinity, exhibit a spherical shape. However, that is often the exception, since most nuclei have relatively large number of valence nucleons. In order to gain stability, spherical symmetry is broken and nuclei deform.

In many cases, the nucleus with an elongated shape can be approximated as an ellipsoid with axial symmetry. In such a case, the monopole and quadrupole terms can describe the nuclear shape.

The nuclear shape can be expressed through the following parametrization of the nuclear radius, usually expanded in spherical coordinates:

$$R(\theta,\phi) = R_0 \left[ 1 + \sum_{\lambda=1}^{\infty} \sum_{\mu=-\lambda}^{\lambda} \alpha_{\lambda\mu} Y_{\lambda\mu}(\theta,\phi) \right], \tag{2.7}$$

where: $\theta$ and $\phi$ are the polar angles and $R_0$ is the radius of a sphere of the same volume. The parameters $\alpha_{\lambda\mu}$ represent the shape deformation, where $\lambda$ denotes the degree of deformation :

$$\begin{cases} \lambda = 0 & \text{monopole deformation (volumic variation).} \\ \lambda = 1 & \text{dipole deformation.} \\ \lambda = 2 & \text{quadrupole deformation (axial symmetric: prolate, oblate).} \\ \lambda = 3 & \text{octupole deformation.} \\ \lambda = 4 & \text{hexadecapole deformation.} \end{cases}$$

For a pure quadrupole deformation, after a transformation in the body-fixed frame described by the Euler angles, the symmetry properties impose the disappearance of the $\alpha_{\lambda\mu}$ coefficients except $\alpha_{2-0}$ and $\alpha_{22}$ with $\alpha_{2-2} = \alpha_{22}$ . The two intrinsic variables of the deformation $\alpha_{20}$ and $\alpha_{22}$ can be re-expressed with the $\beta$ and $\gamma$ deformation parameters formulated by Hill and Wheeler [30]:

$$\alpha_{20} = \beta cos\gamma,$$
$$\alpha_{22} = \frac{1}{\sqrt{2}}\beta sin\gamma.$$

For small oscillations of the ellipsoid, using the Hill and Wheeler deformation parameters, the nuclear radius becomes:

$$R = R_0 \left( 1 + \beta\sqrt{\frac{5}{16\pi}} cos\gamma(3cos^2\theta - 1) + \sqrt{\frac{5}{16\pi}} sin\gamma sin^2\theta cos(2\phi) \right), \tag{2.9}$$

where $\beta$ is the amplitude of the deformation and $\gamma$ gives the strength of axial asymmetry. In the extreme case of axial symmetry, the $\alpha_{\lambda\mu}$ simplifies to only one term $\alpha_{20} = \beta$.

A summary of the different possible configurations in the $(\beta, \gamma)$ plane are shown in

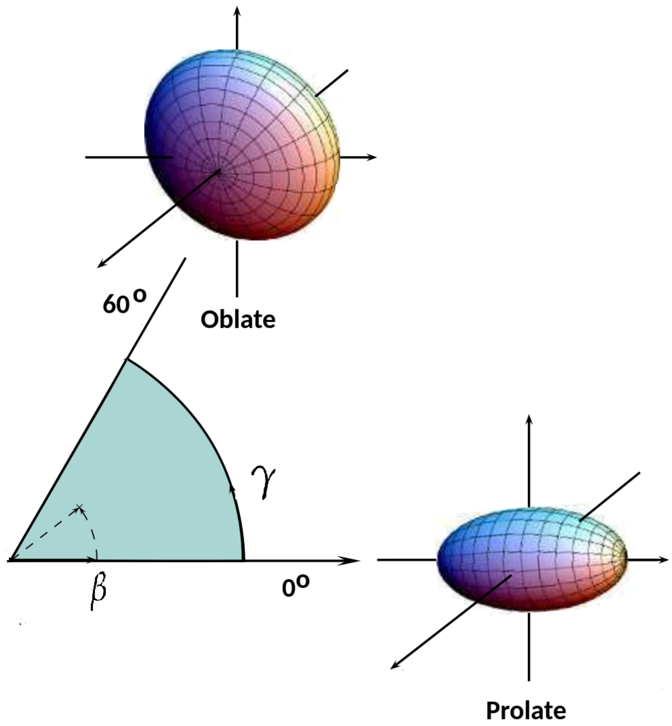


FIGURE 2.2: Deformation parametrization of Hill and Wheeler [30]

Fig. 2.2.

### 2.2.1 The particle(s)-rotor model

A very important consequence of deformation is nuclear rotational motion, since in quantum mechanics a spherical object cannot rotate. The *particle-rotor model* consisting of the valence particle(s) couple to a rotor can illustrate various general features of the deformed nuclei. To a simplified picture, only axially symmetric nuclei are considered. In order to determine the nuclear orientation, the body-fixed coordinate system is labeled with numbers 1, 2, 3, where 3 coincides with the symmetry axis of the nucleus and the subscript number (i.e 3) will be used to specify the projection $\vec{x}_3$ of the vector $\vec{x}$ to the 3-axis. The Hamiltonian is separated in two different parts:

$$H = H_{core} + H_{valence}. \tag{2.10}$$

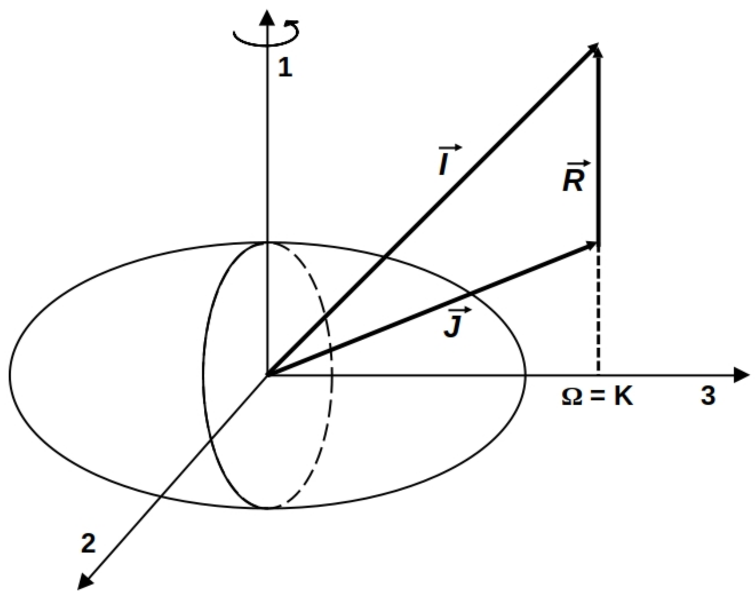


FIGURE 2.3: Coupling scheme of the valence nucleons and the core. **1** axis is the rotational axis and **3** axis is the symmetrical axis. The total angular momentum $\vec{I}$, the rotational angular momentum $\vec{R}$, and the intrinsic angular momentum $\vec{J}$. **K** is defined as the projection of $\vec{I}$ onto the symmetry axis, while Ω is projection of $\vec{J}$.

The coupling of the angular momenta is shown in Figure 2.3. Angular momenta are labeled by $\vec{I}$ for the total angular momentum, $\vec{R}$ for the rotational angular momentum and $\vec{J} = \sum j_n$ for the sum of the intrinsic angular momenta of the valence nucleons outside the deformed core. The projection of $\vec{J}$ to the symmetry axis is $\Omega = \sum \Omega_n$, with $\Omega_n$ is the projection of each valence nucleon. The vector $\vec{R}$ is perpendicular to the symmetry axis, and Ω coincides with K, the projection of the total angular momentum I: K = Ω = $\sum \Omega_n$. $\vec{R}$ and $\vec{J}$ are summed up to $\vec{I}$:

$$\vec{I} = \vec{R} + \vec{J}. \tag{2.11}$$

For an axially symmetric nucleus, the component $R_3 = 0$, then the Hamiltonian can be described as a rigid rotor at the first order with the form:

$$H_{core} = H_{rotor} = \frac{\hbar^2(R_1^2 + R_2^2)}{2\mathscr{I}} = \frac{\hbar^2 \vec{R}^2}{2\mathscr{I}}, \tag{2.12}$$

with $\mathscr{I}$ is the inertia momentum with respect to the rotation axis. According to the equation 2.11, $\vec{R} = \vec{I} - \vec{J}$ we can re-express the rotor Hamiltonian as

$$H_{rotor} = \frac{\hbar^2}{2\mathscr{I}}(\vec{I}^2 + \vec{j}^2 - 2\vec{I}\cdot\vec{j}). \tag{2.13}$$

From the Eq. 2.13 and with the notation $I_\pm = I_1 \pm iI_2$ and $J_\pm = J_1 \pm iJ_2$, the Hamiltonian can be separated in three components:

$$H_{rotor} = \frac{\hbar^2}{2\mathscr{I}}\left(\underbrace{\vec{I}^2 - \vec{I}_3^2}_{\text{Core rotation}} + \underbrace{\vec{J}^2 - \vec{J}_3^2}_{\text{Single Nucleon(s) Rotation}} - \underbrace{(I_+J_- + I_-J_+)}_{\text{"Coriolis Effect"}}\right). \tag{2.14}$$

The "Core Rotation" term is the angular momentum of the core. The second term describes the characteristics of the single nucleon. The last term describes the coupling between the core (with a collective rotation) and the valence part, it has been called Coriolis effect due to its strong similarity with the classical Coriolis effect.

The expectation value of the rotation energy (same as excitation energy in case of ground state band) depend on spin value, I (I $\geq$ K), can be written as:

$$E_{rot}(I) = \frac{\hbar^2}{2\mathscr{I}}\left(I(I+1) - K^2 + a(-1)^{I+1/2}(I+1/2)\delta(K,1/2)\right). \tag{2.15}$$

with $a$ is decoupling parameter.

Rotational band states can be ordered into 3 sequences according to their K values and signature. The signature $\alpha$ is related to the operator for rotation around the 1-axis perpendicular to the symmetry axis (see Figure 2.3) and I takes the values:

$$I = \begin{cases} 0, 2, 4, \ldots & \text{for } K = 0, \alpha = 0 \\ 1, 3, 5, \ldots & \text{for } K = 0, \alpha = 1 \\ K, K+1, K+2, \ldots & \text{for } K \neq 0. \end{cases} \tag{2.16}$$

The ground-state bands with K = 0 are exceptional with respect to the signature partners. The ground-state bands with K = 0 only show the even branch of the rotational band, a sequence with spins of I = 0, 2, 4, . . .

### 2.2.2 Moment of Inertia

In nuclear physics, the moment of inertia refers to a property that characterizes the resistance of a nucleus to changes in its rotation. The moment of inertia of a nucleus is usually less than that of a rigid body, but larger than the moment of inertia of a fluid, revealing the special nature of nuclear matter. For an even-even nucleus, at rest and slow rotation, all nucleons are paired, such that they move like a fluid. As the rotation increases, the Coriolis force breaks pairs, which causes the moment of inertia to increase, until it approaches the rigid body value at very fast rotation. The dependence of the moment of inertia on nuclear rotation reflects the large contribution of the pairing correlation, and thus reveals some structure inside the nucleus.

To visualize the variation of the moment of inertia with spin, the kinematic moment of inertia $\mathscr{I}^{(1)}$ and the dynamic moment of inertia $\mathscr{I}^{(2)}$ are introduced. Experimental measurement values in a typical rotational band with spin difference $\Delta I = 2$ are transition energy $E_\gamma$ and spin $I$. The moments of inertia $\mathscr{I}^{(1)}$ and $\mathscr{I}^{(1)}$ depend on these values as follows:

$$\mathscr{I}^{(1)}(I-1) = \frac{\hbar(2I-1)}{E_\gamma(I \rightarrow I-2)} \quad , \tag{2.17}$$

$$\mathscr{I}^{(2)}(I) = \frac{4\hbar^2}{E_\gamma(I+2 \rightarrow I) - E_\gamma(I \rightarrow I-2)} \quad . \tag{2.18}$$

Usually, the moments of inertia are plotted versus the rotational frequency. The rotational frequency is the derivate of rotational energy with respect to spin:

$$\omega(I) = \frac{1}{\hbar}\frac{\partial H}{\partial I} = \frac{1}{\hbar}\frac{E_I - E_{I-2}}{[I(I+1)]^{1/2} - [(I-2)(I-1)]^{1/2}}. \tag{2.19}$$

## 2.3 General Structure of Matrix Elements

### 2.3.1 E2-Matrix Elements within Band

Nuclear deformation can be determined from the study of appropriate matrix elements connecting the members of a rotational band. The occurrence of a stable deformation implies that these rotational matrix elements are large compared to the corresponding matrix elements associated with fluctuations in the deformation parameter (vibrational or single-particle transitions). The observed nuclear shape deformations are mainly of quadrupole type, and the most detailed evidence on these deformations is provided by the measurement of E2-matrix elements within a rotational band.

The collective $E2$ moment connects states (with $\Delta I \leq 2$) belonging to the same rotational band. The E2-matrix elements between two such states can be evaluated by employing the relations for the reduced matrix elements and transition probabilities to the intrinsic quadrupole moment $Q_0$ [31]

$$\langle KI_2||(E2)||KI_1\rangle = (2I_1+1)^{1/2}\langle I_1K20|I_2K\rangle \left(\frac{5}{16\pi}\right)^{1/2} eQ_0. \tag{2.20}$$

$$B(E2; KI_1 \rightarrow KI_2) = \frac{5}{16\pi}e^2Q_0^2\langle I_1K20|I_2K\rangle^2. \tag{2.21}$$

The vector addition coefficient $\langle I_1K20|I_2K\rangle$, (so-call Clebsch-Gordan coefficient) represents the coupling of the angular momenta in the intrinsic frame.

The diagonal matrix elements ($I_1 = I_2$) give the static moment relation with static quadrupole moment Q:

$$Q = \sqrt{\frac{16\pi}{5}} \begin{pmatrix} I & 2 & I \\ -I & 0 & I \end{pmatrix} \langle KI||E2||KI\rangle. \tag{2.22}$$

And, and lead to the relation to $Q_0$:

$$\begin{aligned} Q &= \langle IK20|IK\rangle\langle II20|II\rangle Q_0 \\ &= \frac{3K^2 - I(I+1)}{(I+1)(2I+3)} Q_0. \end{aligned} \tag{2.23}$$

For the particular case of $I = K$ (which usually applies to the ground state), one obtains

$$Q = \frac{I(2I-1)}{(I+1)(2I+3)} Q_0. \tag{2.24}$$

For the first $E2$-transition of deformed nuclei ($\Delta I = 2$), the electric quadrupole transitions strengths ($B(E2)$ values) related to the magnitude of quadrupole deformation, defined by the $\beta_2$ parameter of the Bohr Hamiltonian

$$\beta_2 = \frac{4\pi}{3ZR_0^2} \sqrt{\frac{B(E2\uparrow)}{e^2}}. \tag{2.25}$$

Here, $R_0 = 1.2A^{1/3}$ fm and the $B(E2\uparrow)$ is exciting probability and in units of $e^2b^2$ or $e^2$ fm$^4$, where the assumption is that the charge and mass distributions are the same.

### 2.3.2 M1-Matrix Elements within Band

The magnetic moment produced by the intrinsic motion vanishes, as a result of time-reversal symmetry, and the leading-order M1 moment is proportional to the rotational angular momentum. To this order, the static moments are given by:

$$\mu = g_R I, \tag{2.26}$$

where the parameter $g_R$ is the effective $g$ factor for the rotational motion. The higher-order terms can be included by treating $g$ as a function of $I(I+1)$. No M1 transitions occur within the band, since successive states have $\Delta I = 2$.

The $g_R$ factors for even-even nuclei are determined from the observed precession of the $2^+$ first rotational states in a magnetic field. The measured $g$ values are comparable to, though in most cases somewhat smaller than, the value Z / A, which would apply to a uniform rotation of a charged body.

The rotational angular momentum is primarily associated with the orbital motion of the nucleons. The relative contribution of the spins is even smaller than the ratio of spin to orbital angular momentum quantum numbers of the individual nucleons, because the splittings of the single-particle levels produced by the spin-orbit force is on the average smaller than the splittings caused by the deformation. The fact that the $g$, values are somewhat smaller than Z/A, thus provides an indication that the protons contribute less effectively than the neutrons to the rotational motion. Such an effect results from the pair correlations, which are somewhat larger for protons than for neutrons.

**Bands with K $\neq 0$ Intrinsic magnetic moment**

For a band with K $> 1/2$, the static moments and M1-transition probabilities can be written as:

$$\mu = g_R I + (g_K - g_R)\frac{K^2}{I+1}. \tag{2.27}$$

$$B(M1; KI_1 \rightarrow K, I_2 = I_1 \pm 1) = \frac{3}{4\pi}\left(\frac{e\hbar}{2Mc}\right)^2 (g_K - g_R)^2 K^2 \langle I_1 K 1 0 | I_2 K\rangle^2. \tag{2.28}$$

The expression for $\mu$ has the simple classical limits $\mu \rightarrow g_R I$ for $I \rightarrow \infty$, K is fixed, and $\mu \rightarrow g_R I$ for $I = K \rightarrow \infty$. The transition probability vanishes for $g_K = g_R$ since then the magnetic moment is proportional to the total angular momentum and hence is a constant of the motion.

# Chapter 3

# Coulomb excitation

Coulomb excitation is a reaction induced by the collision between two nuclei. In such a reaction, if the kinetic energy lower than the Coulomb barrier, the nuclear interaction can be neglected or treated as a perturbation and the reaction process can be understood as mainly electromagnetic in nature. The strength of the Coulomb excitation technique in nuclear structure research, especially the low-energy Coulomb excitation, referred to as "safe", is that the interaction between the two nuclei is described by well-established theory. The interaction probabilities, i.e., the probability that certain energy levels be excited in the beam and target nuclei and subsequently the electromagnetic transition matrix elements involving the populated states, can be precisely determined.

Coulomb excitation was first recognized to be an effective tool for studying nuclear structure in the early 1950s [32]. Light-ion beams were exploited extensively to measure the reduced excitation probabilities and quadrupole moments of the first or second excited states of the target nuclei. Since only one- and two-step excitation processes need to be taken into account, experiments using light-ion beams can be interpreted relatively easily using only first and second order perturbation theory [33]. This approach is no longer viable for heavy-ion beams (typically clarify as $Z_{projectile} \geq 6$ and $Z_{target} > 10$ ), since multiple-steps Coulomb excitation occurs with the involvement of a large number of electromagnetic matrix elements. The complexity of describing multiple Coulomb excitation led to the development of computer programs, among which the GOSIA code [34] is the most widely used.

In this chapter, Coulomb excitation will be briefly described in Section 3.1 and the essential details of the GOSIA code, which was used to analyze experimental data in this research, will be described in Section 3.2

## 3.1 Electromagnetic interaction in Coulomb excitation

At its most basic, Coulomb excitation is a process in which kinetic energy from the beam projectile particles is transferred via electromagnetic interactions to either beam or target nuclei, in the form of excitation energy. In this section, the theoretical description of the reaction process in terms of solvable approximations to the full quantum-mechanical treatment will be presented.

### 3.1.1 The Semiclassical approximation

The condition upon which Coulomb excitation can be called "safe" can be expressed in terms of a classical picture using the distance of closest approach, $b$, for a head-on collision. It has been shown [35] that the beam and target nuclear surfaces should be separated by a distance of 5 fm so that nuclear interactions are conservatively below 0.1 % of the total excitation. This approximation suggests a simple relation between the maximum safe bombarding energy for head-on collisions and the minimum distance of closest approach, i.e.:

$$R_0 \left( A_p^{1/3} + A_t^{1/3} \right) + 5fm > b = \frac{Z_p Z_t e^2}{E_p}, \tag{3.1}$$

where $R_0$ (= 1.20 fm) is the average nucleon radius, $A_{p/t}(Z_{p/t})$ are the mass (charge) numbers of the projectile (p) and target (t) nuclei and $E_p$ is the kinetic energy of the projectile. For the incoming particle to be safely treated classically, the size of the wave packet must be much smaller than the relative distance between the two nuclei. This

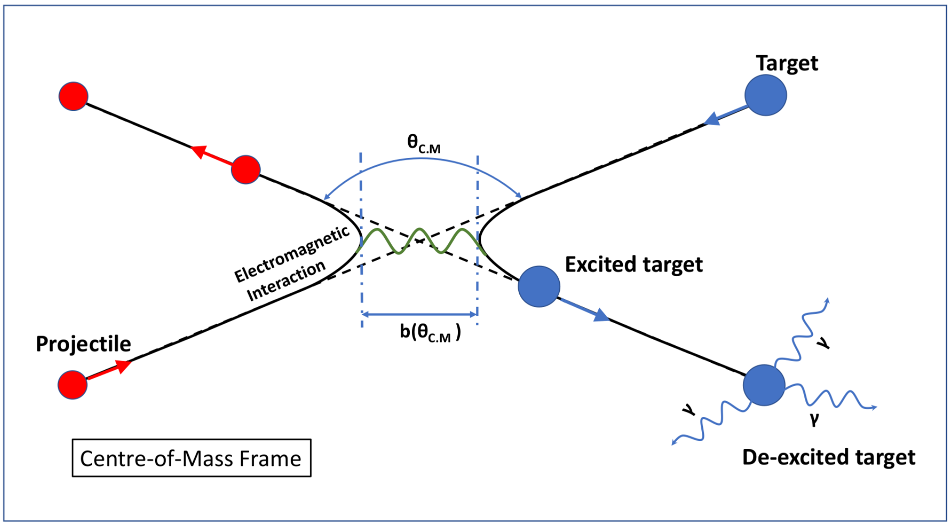


FIGURE 3.1: Coulomb excitation kinematics in the Center of Mass Frame. The hyperbolic orbit is essentially the same as that in Rutherford scattering.

is achieved when the Sommerfeld parameter, $\eta$, is much greater than unity:

$$\eta = \frac{2\pi}{\lambda} = \frac{Z_p Z_t e^2}{\hbar v_p} \gg 1, \tag{3.2}$$

where a = b/2, half the distance of closest approach, $\lambda$ is the de Broglie wavelength of the projectile with a velocity $v_p$ and $Z_p e$ and $Z_t e$ are the respective charges of the projectile and target nuclei. For typical heavy-ion induced Coulomb excitation, equations 3.1 and 3.2 yield values of $\eta$ ranging from 10 to 500 for $Z_{projectile} \geq 6$ and $Z_{target} > 10$.

The hyperbolic trajectory depicted in Figure 3.1 is symmetric, which is only true if the incoming and outgoing energies are similar, i.e., the inelastic scattering can be approximated to elastic scattering. This introduces another requirement, that the energy transfer, ΔE, must be much smaller than the projectile energy, $E_p$, i.e.,

$$\frac{\Delta E}{E_p} \ll 1. \tag{3.3}$$

For heavy projectiles ($Z \geq 6$) at low energy, the condition $\eta \gg 1$ is fulfilled, and, usually, the excitation energy is small compared to the incoming beam energy. As a consequence, the semi-classical approximation is valid for the analysis of heavy-ion Coulomb excitation. Then the Coulomb-excitation cross section can be represented as a product of the "Rutherford" cross section, $\sigma_R$, and the probability, $P_n$, of exciting a given state, $|n\rangle$:

$$\frac{d\sigma_n}{d\Omega} = P_n \frac{d\sigma_R}{d\Omega}. \tag{3.4}$$

Here, the standard Rutherford cross-section is given by

$$\frac{d\sigma_n}{d\Omega} = \frac{a^2}{sin^4(\upsilon/2)}, \tag{3.5}$$

where $\upsilon$ is the center of mass scattering angle and $a$ is half the distance of closest approach, $b$, defined in equation 3.1.

The semiclassical approach elucidates the time evolution of the excitation of the excited states as the projectile moves along the classical hyperbolic trajectory. Since the most of the excitation occurs within some tens of femtometers off the turning point, the timescale of the excitation is in the order of $10^{-21}$ s, i.e., is $10^8$ times shorter than lifetimes for $\gamma$-ray decay which typically are in the order of $10^{-13}$ - $10^{-12}$ s [35]. Thus, the excitation and de-excitation processes can be treated separately and sequentially.

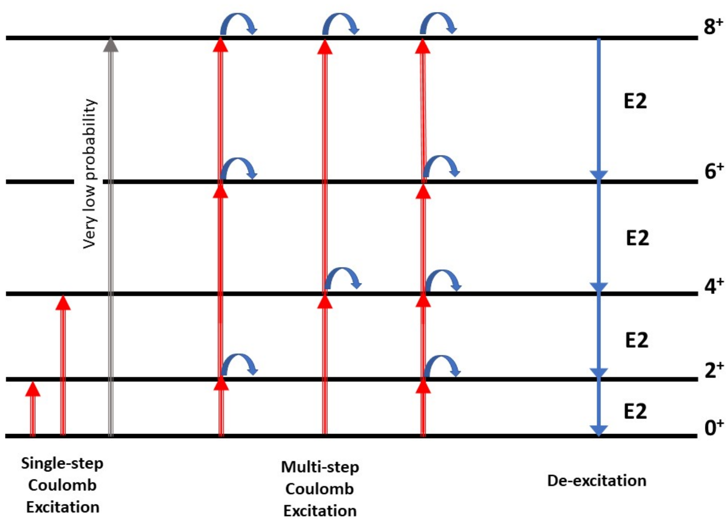


FIGURE 3.2: Schematic diagram of Single/ Multiple-step Coulomb excitation followed by $\gamma$-ray de-excitation.

These processes are schematically represented in Figure 3.2 for an even-even nucleus with a $0^+$ ground state. Assuming that $8^+$ is the highest spin state populated in the reaction, a single-step excitation process is defined as the direct excitation path $0^+ \to 8^+$ while the multiple-step excitation process which become dominant in heavy-ion induced Coulomb excitation, represents the summation of every excitation path connected to the $8^+$ state. After the excitation, the nucleus decays by emitting $\gamma$ rays that, in this case, are mostly characterized by E2 multipolarity. The blue turn arrow shows the involvement of the static moment in the excitation process. The following sections will briefly describe how to treat these processes under the classical approximation.

### 3.1.2 Single-step Coulomb excitation

A simple way of viewing the excitation is to treat it as a first-order perturbation to the time-dependent Schrödinger equation [32]:

$$i\hbar = \frac{\delta}{\delta t}|\psi(t)\rangle = [H_0 + V(t)]|\psi(t)\rangle, \tag{3.6}$$

where $H_0$ is the intrinsic free Hamiltonian which treats the elastic ("Rutherford") scattering and the classical trajectory, and where V(t) is the electromagnetic interaction, responsible for the excitation of either the projectile or the target nucleus. In Coulomb-excitation experiments, it is good to choose one of the colliding nuclei to have ground-state spin zero and high-lying first excited state. By doing so, in fact, the probability of mutual excitation of both target and projectile is small and can be neglected.

Assuming that the target nucleus is in initial state $|i\rangle$ at $t = -\infty$, the final (excited) state $|f\rangle$ does not decay before the end of collisions, taken to be at $t = +\infty$ and with angular momenta $I_{i,f}$. The solution of equation 3.6 consists of a sum of excitation amplitudes $a_{i,f}$ and should consider all magnetic substates, but by summing and averaging over final and initial magnetic substates, the amplitudes can be found for the full degenerate energy level. The transition amplitudes can then be defined in terms of the nuclear frequency related to excitation energy as $\omega = (E_f - E_i)/\hbar$, and the interaction strength between the two states:

$$a_{if} = \frac{i}{\hbar} \int_{-\infty}^{\infty} \langle f|V(r(t))|i\rangle e^{i\omega t} dt. \tag{3.7}$$

This perturbation approach is valid when the excitation energy is small compared to the total energy of the system.

In the non-relativistic regime, the magnetic multipoles can be neglected, since magnetic excitations are proportional to $(v/c)^2$ and are much smaller than their electric counterparts. Therefore, the matrix element in equation 3.7 can be evaluated by expanding the monopole-multipole interaction into the constituent multipole components:

$$V(r(t)) = \sum_{\lambda=1}^{\infty} \sum_{\mu=-\lambda}^{\lambda} \frac{4\pi Z_0' e}{2\lambda+1} S_{\lambda\mu} T(E\lambda, \mu), \tag{3.8}$$

with

$$S_{\lambda\mu} = \frac{Y_{\lambda\mu}(\theta(t), \phi(t))}{r(t)^{\lambda+1}}, \tag{3.9}$$

where $Z_0'$ is the atomic number of the other collision partner, $Y_{\lambda\mu}(\theta(t), \phi(t))$ are the normalized spherical harmonics with angles $\theta$ and $\phi$ in the center of mass frame and $T(E\lambda, \mu)$ is the electric multipole moment of the nucleus undergoing excitation.

Substituting equation 3.8 into equation 3.7, the excitation amplitudes can be evaluated in terms of the nuclear matrix elements as:

$$a_{if} = \frac{4\pi Z' e}{i\hbar} \sum_{\lambda\mu} \frac{1}{2\lambda+1} \langle I_f M_f|T(E\lambda, \mu)|I_i M_i\rangle R_{\lambda,\mu}, \tag{3.10}$$

with

$$R_{\lambda,\mu} = \int_{-\infty}^{\infty} e^{i\omega t} S_{\lambda\mu} dt = \int_{-\infty}^{\infty} e^{i\omega t} \frac{1}{r(t)^{\lambda+1}} Y_{\lambda\mu}(\theta(t), \phi(t)) dt, \tag{3.11}$$

and where the reduced matrix elements are given by Wigner-Eckart theorem:

$$\langle I_f M_f | T(E\lambda, \mu) | I_i M_I \rangle = (-1)^{I_f - M_f} \begin{pmatrix} I_f & \lambda & I_i \\ -M_f & \mu & M_i \end{pmatrix} \langle I_f || E\lambda || I_i \rangle. \tag{3.12}$$

The probability $P_n$ in equation 3.4 can be generalized for any given excitation path connecting an initial state $|i\rangle$ and final state $f\rangle$ :

$$P_{if} = \frac{1}{(2I_i + 1)} \sum_{M_i M_f} |a_{if}|^2. \tag{3.13}$$

Substituting $a_{if}$ described in equation 3.10 into equation 3.13 and, in turn, $P_{if}$ into equation 3.4, we obtain the differential Coulomb-excitation cross-section, for each electric multipole:

$$\frac{d\sigma_{E\lambda}}{d\Omega} = \left( \frac{2\pi Z' e a}{\hbar} \right)^2 \frac{B(E\lambda)}{sin^4 \left( \frac{v}{2} \right)} \sum_{\mu} |R_{\lambda,\mu}|^2. \tag{3.14}$$

with the total differential cross-section for Coulomb excitation being the sum over all multipoles:

$$\frac{d\sigma_{CE}}{d\Omega} = \sum_{\lambda=1}^{\infty} \frac{d\sigma_{E\lambda}}{d\Omega}. \tag{3.15}$$

### 3.1.3 Multiple-step Coulomb excitation

When describing multiple-step Coulomb excitation, the treatment of the excitation probability can be represented as a coupled set of differential equations, where all possible paths are considered. The amplitude of an excitation to a state $k$ now depends on the couplings to all states $n$, namely the matrix elements defined in equation 3.12 and the energy difference between the levels, $E_k - E_n$. Of course, the probability, or more precisely, the amplitude for exciting the state $n$, $a_n$, is a crucial factor, one which further depends on couplings to all other states, including the state $k$,

$$\frac{da_k}{dt} = -i\frac{4\pi Z'e}{\hbar}\sum_n a_n(t) exp\frac{it}{\hbar}(E_k - E_n)\sum_{\lambda\mu}(-1)^\mu S_{\lambda\mu}(t)\cdot\langle I_k M_k|T(E\lambda,\mu)|I_n M_n\rangle. \tag{3.16}$$

Integration of these coupled differential equations is complex and requires a numerical approach. The solution to such a problem has been refined in the coupled-channel computer code, GOSIA, described in Section 3.2.

### 3.1.4 Gamma ray de-excitation process

After the Coulomb-excitation process, the excited states of the nucleus decay mainly via $\gamma$-ray emission. While the Coulomb excitation process has highly dominant electric multipole components, the decay proceeds via both electric and magnetic transitions. The distribution of $\gamma$-ray emission is expressed in terms of a double-differential over a particular set of emission angles of the scattered particle ($d\Omega_p$), and the emission angles of the $\gamma$ ray ($d\Omega_\gamma$):

$$\frac{d^2\sigma}{d\Omega_p d\Omega_\gamma} = \sigma_R(\theta_p)\sum_{k\chi} R_{k\chi}(I_i, I_f) Y_{k\chi}(\theta_\gamma, \phi_\gamma), \tag{3.17}$$

where $I_i$ is the spin of the excited state, $I_f$ is the spin of the final state, $\theta_p$ is the scattering angle of the particle relative to the beam $(z)$ axis, $\theta_\gamma$ is also with respect to the beam axis, and $\phi_\gamma$ extends around the $z$-axis, defined such that the scattering trajectory of the beam particle lies in the $+x - z$ plane.

The function $\sigma_R(\theta_p)$ represents the Rutherford scattering cross-section dependence on scattering angle $\theta_{cm}$ (where the subscript $'cm'$ stands for the center of mass frame):

$$\sigma_R(\theta_p) \equiv \left(\frac{d\sigma}{d\Omega}\right)_R = \left(\frac{e^2}{16\pi\epsilon_0}\frac{Z_p Z_t}{E_{cm}}\right)^2 \frac{1}{sin^4(\theta_{cm}/2)} \quad . \tag{3.18}$$

The $Y_{k\chi}(\theta_\gamma, \phi_\gamma)$ term are normalized spherical harmonic functions. The index $k$ in equation 3.17 defines a summation over a series of spherical harmonic functions and

$\chi$ is the magnetic substate (polarization) index. The functions $R_{k\chi}(I, I_f)$ are the decay statistical tensors describing the decay process. To first-order, they are given by the equation

$$R_{k\chi}(I, I_f) = \frac{1}{2\gamma(I)\sqrt{\pi}} \rho_{k\chi}(I) \sum_{\lambda\lambda'} \sigma_\lambda \sigma^*_{\lambda'} F_k(\lambda\lambda', I_f I). \tag{3.19}$$

The function $\gamma(I)$ is the emission probability in the $I \to I_f$ transition for a particular multipolarity $\lambda$. It is defined by the transition amplitudes $\sigma_\lambda$:

$$\gamma(I) = \sum_{\lambda_n} |\sigma_\lambda(I \to I_n)|^2, \tag{3.20}$$

with transition amplitude $\sigma_\lambda$ given by:

$$\sigma_\lambda = i^{n(\lambda)} \frac{1}{(2\lambda+1)!!\hbar^{\lambda+1}} \left(\frac{8\pi(\lambda+1)}{\lambda}\right)^{1/2} \left(\frac{E_\gamma}{c}\right)^{\lambda+1/2} \frac{\langle I_f||E(M)\lambda||I\rangle}{(2I+1)^{1/2}}, \tag{3.21}$$

where

$$n(\lambda) = \begin{cases} \lambda \text{ for E}\lambda \text{ transition,} \\ \lambda + 1 \text{ for M}\lambda \text{ transition.} \end{cases}$$

The second term $\rho_{k_\chi}(I)$ is a statistical tensor describing the magnetic substate distribution of the excited state (see Ref [36]). Given a magnetic quantum number $M_0$ for a particular substate of the ground state, an excited substate $|IM\rangle$, and excitation amplitudes of these substates $a_{IM}$ ,

$$\rho_{k_\chi}(I) = \frac{\sqrt{2I+1}}{2I_0+1} \sum_{M_0 M M'} (-1)^{I-M'} \begin{pmatrix} I & k & I \\ -M' & \chi & M \end{pmatrix} a^*_{iM'}(M_0) a_{IM}(M_0). \tag{3.23}$$

The functions $F_k$ are $\gamma - \gamma$ correlation coefficients (as defined, i.e., in [37], in terms of Wigner 3-j and 6-j symbols as

$$F_k(\lambda\lambda', I_f I) = (-1)^{(I_f+I+1)} \sqrt{(2k+1)(2I+1)(2\lambda+1)(2\lambda'+1)} \begin{pmatrix} \lambda & \lambda' & k \\ 1 & -1 & 0 \end{pmatrix} \begin{Bmatrix} \lambda & \lambda' & k \\ I & I & I_f \end{Bmatrix}. \quad (3.24)$$

To reproduce the experimentally observed $\gamma$-ray intensities for a given beam energy and scattering angle $\theta_p$, the double-differential cross-sections in equation 3.17 should be integrated over the $\phi_p$ angular range of the particle detector for each $\theta_p$ scattering angle:

$$Y_{point}((I \to I_f), \theta_p, E) = \int_{\phi_p} \frac{d^2\sigma(I \to I_f)}{d\Omega_p d\Omega_\gamma} d\phi_p. \quad (3.25)$$

## Cascade de-excitation feeding

The angular distribution tensor described in equation 3.19 applies to a $\gamma$-decay of a level fed directly, and exclusively, by a single-step Coulomb excitation prior to decay. For multi-step Coulomb excitation, significant feeding from the de-excitation cascade of higher-lying levels must be taken into account. The modification of the angular distribution tensor is expressed as :

$$R_{k\chi}(I, I_f) \to R_{k\chi}(I, I_f) + \sum_n R_{k\chi}(I_n, I) H_k(I, I_n), \quad (3.26)$$

where the summation extends over all levels $I_n$ directly feeding level I. The explicit formula for the $H_k$ coefficients is:

$$H_k(I, I_n) = \frac{[(2I+1)(2I_n+1)]^{1/2}}{Y(I)} \sum_\lambda (-1)^{I+I_n+\lambda+k} |\delta_\lambda|^2 (1 + c(\lambda)) \begin{Bmatrix} I & I & k \\ I_n & I_n & \lambda \end{Bmatrix}, \quad (3.27)$$

where $c(\lambda)$ is the internal conversion coefficient for the $I \rightarrow I_n$ transition. This formula is used to sequentially modify the de-excitation statistical tensors, starting from the highest level having non-negligible population.This operation transforms the de-excitation statistical tensors, which are inserted into equation 3.17 to give the unperturbed angular distributions following Coulomb excitation.

### 3.1.5 Sensitivity to observables

Coulomb excitation is most sensitive to the $E1$, $E2$ and $E3$ excitation multipoles, but usually the $E1$ excitation is negligible because the $E1$ strength is almost exhausted by the high-lying giant dipole resonance which is not populated via Coulomb excitation due to its high excitation energy. Thus, $E2$ and $E3$ are the multipoles studied, since typically the $E4$ excitation mode can be also neglected [34].

The reorientation effect in multiple-Coulomb excitation provides sensitivity to the sign and magnitude of static $E2$ moments of excited states. The sensitivity results from the interaction of the static $E2$ moment with the strong electric field gradient existing during Coulomb excitation. The modification to the angular distribution of the observed $\gamma$-ray yields from this effect can be small, but in high-statistics experiments the analysis of the change in distribution can provide measurements of static moments.

Magnetic excitation is also negligible for sub-barrier Coulomb excitation. However, $B(M1)$ strengths parameters can be fitted to a large set of $\gamma$-ray yield data plus $\gamma$-ray branching ratios and mixing ratios determined.

Coulomb excitation process at bombarding energies below the Coulomb barrier is not sensitive to M1 static moments. The magnetic interaction between the magnetic dipole moments of the excited nuclear states and the $\sim 10^4$ T atomic hyperfine magnetic fields produce the dominant hyperfine interaction responsible for the de-orientation effect that greatly perturbs the $p-\gamma$ angular correlations. Unfortunately, the atomic hyperfine fields involve complicated stochastic processes that currently cannot be predicted. The current version of GOSIA uses a common $g$-factor for all states.

## 3.2 The GOSIA Analysis Code

The earliest computer code to analyze of multiple Coulomb excitation data was developed by Winther and de Boer in 1965[38]. The program calculates the expected $\gamma$-ray yields resulting from a heavy-ion Coulomb-excitation experiment based on the input of a set of fixed matrix elements. The input requires a certain knowledge of the quadrupole properties of the nucleus and, as such, depends on the use of nuclear models. This issue and many more, such as the treatment of higher multipole orders, was overcome by Czosnyka, Cline and Wu with the introduction of the GOSIA code [34].

The GOSIA code is an experiment-oriented program whose purpose is to design and analyze experiments that fit matrix elements to the best reproduction of a large experimental data set. These data include the de-excitation $\gamma$-ray yields observed in Coulomb excitation experiments and available spectroscopic information such as branching ratios, $E2/M1$ mixing ratios, level lifetimes and previously measured matrix elements. It allows one to determine the full set of matrix elements for the investigated nucleus with a realistic estimate of the errors of the fitted matrix elements.

### 3.2.1 Yield determination

The calculation of *point*-yields $Y_{point}(I \rightarrow I_f)$ for every transition of interest, with a particular combination of particle scattering angle and $\gamma$-ray emission angle, relies on solving equation 3.25. The GOSIA code numerically integrates this equation around the possible $\phi_p$ particle scattering angles to determine these values, and sums over spherical harmonics from k = 1 to k = 8 in equation 3.17, which generally provides sufficient accuracy [34]. These calculations depend on the initial values of the matrix elements for the transitions that affect the interested $\gamma$-ray yields. Details of these required inputs are provided in section 3.2.2 and 3.2.3. A small correction is performed to account for the energy loss during the Coulomb excitation inelastic scattering by averaging between the perturbed and unperturbed orbits. Also, the angular attenuation factors, which describe the efficiency of the $\gamma$-ray detectors as a function of angle, are an essential input. The details of the GOSIA inputs for this work will be described in Section 5.4.

### 3.2.2 Angular attenuation factors

In order to reproduce an experimental $\gamma$-ray angular distribution accurately, it is necessary to take into account the efficiency of each $\gamma$-ray detector, its finite size, as well as $\gamma$-ray absorption in absorbers and the detector. All these effects attenuate and smooth down the observed $\gamma$-ray angular correlations [36].

The probability of detection of a $\gamma$-ray at a particular location needs to be determined. This is accomplished by introducing angular attenuation factors (Q) to the yield integration. To deduce angular attenuation factors, the location, and geometry of the $\gamma$-ray detectors, and $\gamma$-ray efficiency as a function of angle, need to be identified. In general, GOSIA assumes that all $\gamma$-ray detectors have cylindrical symmetry about the unit vector $\vec{r}_i$ from the nucleus emitting the $\gamma$-ray and the detector $i$. The attenuation factors Q are expressed as

$$Q_k(E_\gamma) = \frac{J_{k0}(E_\gamma)}{J_{00}(E_\gamma)}, \tag{3.28}$$

with

$$J_{k0}(E_k) = \int_0^{\alpha_{max}} P_k(cos\alpha)\xi K(\alpha)(1 - exp(-\tau(E_\gamma)x(\alpha))sin(\alpha)d\alpha, \tag{3.29}$$

where $E_\gamma$ is the $\gamma$-ray energy, $\alpha$ is the angle between detector symmetry axis and the $\gamma$-ray direction, $\tau$ is an energy-dependent absorption coefficient of the active germanium layer, $x$ stands for the angle-dependent path length in the detector, and $\xi$ is the photo-peak efficiency. $P_k(cos(\alpha))$ are the Legendre polynomials, while the function $K(\alpha)$ is to account for the effect of the $\gamma$-ray interactions in the inactive core of the detector, as well as other absorbers including target chamber wall and detector end cap. The function $K(\alpha)$ can be written as,

$$K(\alpha) = 1 - \frac{1}{exp(\sum_i \tau_i(E_\gamma)x_i(\alpha))}, \tag{3.30}$$

where the summation extends over various absorbers, the p-core, in case of coaxial detector. The $Q_k$ factors for the total-energy peak efficiency, resulting from equation 3.28, have to be evaluated numerically using a Monte Carlo code. In order not to repeat this procedure for other $\gamma$-ray energy, it is practical to fit a simple analytic function describing the energy dependence, given by following equation [34]:

$$Q_k(E_\gamma) = \frac{C_2 Q_k(E_0) + C_1(E_\gamma - E_0)^2}{C_2 + (E_\gamma - E_0)^2}, \tag{3.31}$$

The $E_0$ is low energy cut-off, set to be 50keV with no graded absorbers or with specified combination of Al, C, and Fe, while $E_0$ = 80, 100, or 150 keV if Cd/Sn, Ta, or Pb absorber layer are employed, respectively. $C_1$ and $C_2$ are the fitted parameters to reproduce the energy dependence obtained using this formalism.

In practice, the $\gamma$-ray detector can have more complex crystal shapes and assemblies, such as Clover (rounded-edge square shape) or GRETINA (hexagon shape) detectors. Table 3.1 illustrates the $Q_{k\chi}$ for different detector shapes covering the same solid angle [34]. It has been shown that for both hexagonal and square shape the $Q_{k0}$ values differ by the order of $\leq 2 \times 10^{-3}$ from the values evaluated for cylindrical symmetry, while higher $\chi$ terms of $Q_{k\chi}$ are negligible. Thus, the cylindrical shape approximation is good for axially-symmetric geometries having square or hexagonal symmetries.

### 3.2.3 Integration over target energy loss and scattering angle

As traveling through the target, the beam ions lose their kinetic energy continuously. In order to reproduce the experimentally observed $\gamma$-ray yield, it is necessary to integrate over a finite range of scattering angle and the range of the beam energy as they pass through the target material. Given point yields $Y_{point}(I \rightarrow I_f)$ as defined in

TABLE 3.1: $Q_{k\chi}$ for black-body, axially-symmetric $\gamma$-ray detectors that have a solid angle of $0.181sr$.

| | Cylinder | Hexagon | | Square | | |
|---|---|---|---|---|---|---|
| k | $\chi = 0$ | $\chi = 0$ | $\chi = \pm 6$ | $\chi = 0$ | $\chi = \pm 4$ | $\chi = \pm 8$ |
| 1 | 0.986 | 0.986 | | 0.985 | | |
| 2 | 0.957 | 0.957 | | 0.955 | | |
| 3 | 0.916 | 0.915 | | 0.912 | | |
| 4 | 0.862 | 0.861 | | 0.857 | 0.00026 | |
| 5 | 0.798 | 0.797 | | 0.791 | 0.00076 | |
| 6 | 0.725 | 0.724 | $5.2 \times 10^{-6}$ | 0.716 | 0.0016 | |
| 7 | 0.646 | 0.644 | $1.8 \times 10^{-6}$ | 0.635 | 0.0030 | |
| 8 | 0.560 | 0.560 | $2.7 \times 10^{-6}$ | 0.550 | 0.0049 | $5.5 \times 10^{-5}$ |

equation 3.25, the fully integrated yields $Y_{int}(I \to I_f)$ are given by

$$Y_{int}(I \to I_f) = \int_{E_{min}}^{E_{max}} dE \frac{1}{\left(\frac{dE}{dx}\right)} \int_{\theta_{min}}^{\theta_{max}} Y_{point}(I \to I_f) sin(\theta_p) d\phi_p. \tag{3.32}$$

In this equation, $E_{max}$ and $E_{min}$ are the initial and final beam energies respectively, and $\theta_{pmin}$ and $\theta_{pmax}$ are the minimum and maximum angles of the particle detector segment from the beam axis. GOSIA code performs this integration in two separate steps. First, the full Coulomb excitation coupled-channel calculation is done at each of the user-specified $(\theta_p, E)$ meshpoint to evaluate the *point* $\gamma$-yields. Next, the actual numerical integration is performed according to the user-defined step-sizes in both dimensions.

### 3.2.4 Coupled channel fitting

As introduced in previous sections, from a set of initial matrix elements affecting the transition of interest, the calculated yields, incorporating the physical angles of the particle detector and the energy loss of the nuclei passing through the target, can be compared to the experimental data. By searching the matrix element values that give the calculated yields best fit to the experimentally-determined yields, measurements of the matrix element values can be obtained. The searching is done by requesting the minimum of least-squares statistic defined as follows:

$$S = \frac{1}{N}\left(\sum_i \frac{1}{\sigma_i^2}\left(Y_i^{exp} - Y_i^{calc}\right)^2 + \sum_j \frac{1}{\sigma_j^2}\left(d_j^{exp} - d_j^{calc}\right)^2\right), \tag{3.33}$$

where $Y$ represents the gamma-ray yield for each measured transition in each data set, $i$, and the superscripts "exp" and "calc" are for the experimental and calculated values, respectively. The second summation accounts for the number of independent spectroscopic data such as lifetime, mixing ratio or branching ratio, $j$, where $d$ represents the value of each input value while $\sigma$ is the associated uncertainty of each input value.

The statistical method used by GOSIA is very similar to the least-squares $\chi^2$ method with the exception that it is normalized to the total number of data points, N, rather than the number of degrees of freedom. This is due to the fact that the concept of the number of degrees of freedom is based on the assumption that all the parameters are of about equal significance; while in the case of Coulomb excitation, the sensitivity of the observed $\gamma$ yields to the various matrix elements can differ by orders of magnitude. This can be illustrated by noticing that to describe a given experiment one can arbitrarily add any number of unobserved levels connected by any number of the matrix elements having no influence on either the Coulomb excitation or the $\gamma$ de-excitation, thus arbitrarily changing the number of parameters and, consequently, the number of degrees of freedom.

The least-squares statistic $S$ is used to determine a set of the matrix elements fitted to the experimental data as well as to ascribe the errors of the fitted matrix elements, which are defined by the shape of the $S$ hypersurface in the space of the matrix elements.

As a byproduct of the minimization, GOSIA provides a map of sensitivity of the calculated $\gamma$-yield or excitation probability to the matrix elements. The data obtained during the compilation of the yield sensitivity map are used to generate the correlation matrix and selecting the subsets of matrix elements that are strongly correlated for the error estimation.

### 3.2.5 Error estimation of fitted matrix elements

The commonly used methods of estimating the errors of fitted parameters (in this case the matrix elements) resulting from a least-squares minimization, do not apply to Coulomb excitation analyses using GOSIA.

It can be assumed that a set of observables, $Y_k$, measured with known and fixed experimental errors, $\sigma_k$, is used to determine the values of a set of parameters, $x_i$. We also assume that the observables are related to the parameters by an error-free functional dependence, i.e., that if the experiments were error-free each experimental point $Y_k$ could be exactly reproduced as:

$$Y_k = f_k(\overline{x}), \tag{3.34}$$

where $f_k$ stands for the functional description of the $k$-th observed data point using a given set of parameters, represented as a vector.

The assumption that a set of $n$ parameters is sufficient to reproduce $N$ experimental observables ($N \geq n$), is equivalent to assuming that only certain values of observed data forming a $n$-dimensional hypersurface in the space of observables are allowed. From this point of view, the extraction of the parameters based on a set of observables reduces to determining which point on a hypersurface of the "allowed" experimental values (referred to as a "solution locus") corresponds to the measured values. While the assignment of the closest point on a solution locus defines a "best" set of parameters, the distribution of the probability that different points belonging to the solution locus actually represents the set of observables defines the errors ascribed to the parameters. It can be shown that both the "best" set of the parameters and the corresponding errors can be found by examining the least-squares statistic if the "perfect theory" approach is assumed. Such an approach, actually employed in GOSIA, is presented below.

To simplify the notation, it is convenient to introduce the normalized observables, $y_k$, defined as:

$$y_k = \frac{Y_k}{\sigma_k}, \tag{3.35}$$

and to assume that the functional dependence also includes the normalization relative to the fixed experimental errors $\sigma_k$. Treating both the set of normalized observables and the set of normalized functional dependencies as vectors, allows a compact definition of the unnormalized least-squares statistic, $\chi^2$, as:

$$\chi^2 = \left[\overline{f}(\overline{x}) - \overline{y}\right]^2, \tag{3.36}$$

The symbol $\chi^2$ was used to distinguish the unnormalized statistic from the normalized statistic $S$ as defined by equation 3.33.

It is necessary to adopt a "worst case" approach, i.e., to use an approximation yielding overestimated error bars but allowing a reduction of the multidimensional problem to a one-dimensional one without performing the numerical integration in the multidimensional space. To construct such an approach, GOSIA introduce the concept of a "maximum correlation curve" defined as a curve in the parameter space for which an effect of varying a given parameter is, to the greatest extent, balanced by the changes of the correlated parameters to minimize an overall change of the $\chi^2$ function.

Introducing the above approximations, the error bars of a given parameter can be found by requesting that the probability that the "true" value of this parameter is contained within the error bars and is equal to an adopted confidence limit of 68.3%; this corresponds to the confidence level for one standard deviation in a Gaussian distribution. Since, neither the minimum is perfect, nor the symmetry of $\chi^2$ around the minimum is assumed, upper and lower error limits are defined independently. This is explicitly given by requiring that:

$$\frac{\int_{x_i}^{x_i+\delta x_i} exp\left(-\frac{1}{2}\chi^2(x_i)dl(\overline{x})\right)}{\int_{x_i}^{x_i(max)} exp\left(-\frac{1}{2}\chi^2(x_i)dl(\overline{x})\right)} = 0.683, \tag{3.37}$$

where $\delta x_i$ stands for the upper error limit, while $x_i(max)$ denotes the maximum allowed value of $x_i$, $l$ stands for the "maximum correlation" path and the probability distribution is treated as a function of the $i$-th parameter only; the dependence on other correlated parameters being defined by the path of integration, $l$. A similar formula is used to determine the lower error limit, with the maximum allowed value of $x_i$ replaced by the minimum allowed value of this parameter.

The error estimation formalism, presented above, fits well the needs of Coulomb excitation analysis. It is not sensitive to the redundant parameters, which will simply display no influence on the $\chi^2$ statistic. It allows the introduction of physical limits for the matrix elements just by normalizing the probability distribution to its integral between those limits.

The error estimation in GOSIA is numerically performed in two separate steps: the "diagonal" errors and the "full", or correlated, error estimation. The "diagonal" errors are the errors of individual matrix elements, with all the others kept fixed. The calculation consists of a straightforward numerical solution of equation 3.37, the fourth-order Runge-Kutta integration method is used to numerically evaluate the integrals involved. Since the influence of a given matrix element is not known a priori, a common stepsize is used. This part of the error calculation is relatively fast and provide useful information to effectively estimate the "full" errors.

The diagonal error calculation is usually repeated a few times until the minimum of the least-squares statistic S is found to be satisfactory from the point of view of individual matrix elements. The following "full" error calculation differs from the diagonal error calculation only by applying equation 3.37 along the predicted path of maximum correlation. An estimate of the diagonal error for a given matrix element is first used to evaluate an appropriate stepsize for the Runge-Kutta integration algorithm. This approach is subsequently refined by adjusting the stepsize for each matrix element individually during the full error calculation based on the diagonal error range.

## Summary

In this chapter, the Coulomb excitation reaction mechanism were presented and described using semiclassical picture. GOSIA, the publicly available code used in this work to analyze the Coulomb-excitation experimental data, was introduced. The main contents and additional essential corrections were described. In the following chapter, the experimental apparatus employed in Coulomb excitation technique will be discussed.

# Chapter 4

# Experimental setup

Coulomb excitation measurements are normally carried out using a combination of particle and $\gamma$-ray detectors. The particle detector measures the angle and energy of the scattered beam particles. The scattered ion can be identified from its kinetic energy and scattering angle. $\gamma$ rays are detected in coincidence with signals from particle detectors. The coincident detection of particle and $\gamma$ rays permits not only to determine the origin of the $\gamma$ ray, but also to perform the Doppler correction to improve the energy resolution of the gamma spectrum.

The $^{254}$Es Coulomb excitation experiment was performed at the JAEA-Tokai Tandem accelerator using a $^{58}$Ni beam with an energy of 250 MeV. The scattered nuclei were detected by CD-Silicon detectors placed at backward and forward angles from the target along the beam direction. The $\gamma$ rays were detected using 4 $LaBr_3$(Ce) scintillators, 4 coaxial and 4 Clover-type High Purity Germanium (HPGe) detectors. The details of the experimental setup will be introduced later in this chapter.

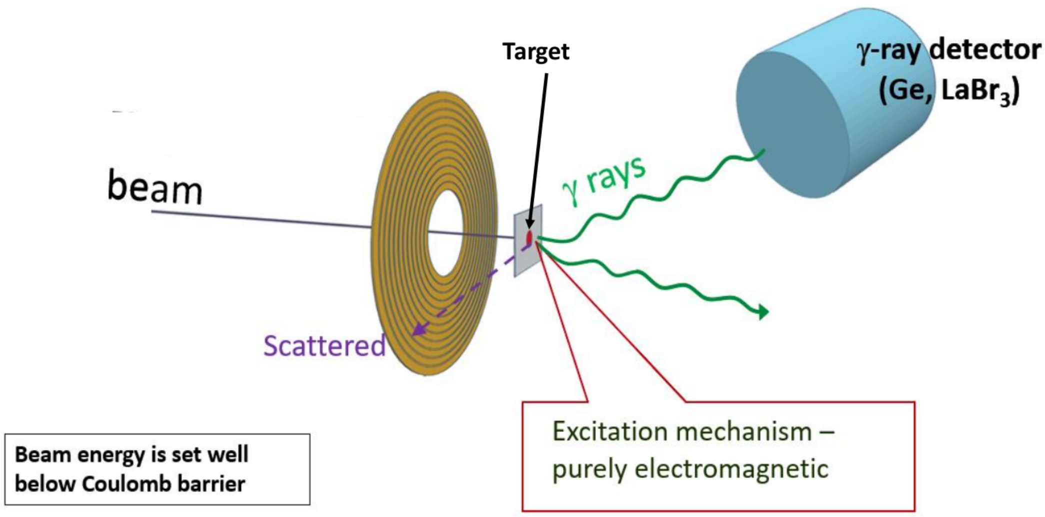


FIGURE 4.1: Coulomb excitation experiment principles

## 4.1 The Einsteinium-254 target

Einsteinium (Es, atomic number Z=99) was discovered in 1952 from hydrogen bomb testing. The $^{254}$Es sample, used in this research, was synthesized in the High Flux Isotope Reactor (HFIR) at Oak Ridge National Laboratory (ORNL), USA. Several tens of grams of americium (Am, Z = 95) and curium (Cm, Z = 96) were enclosed in a container, then irradiated by neutrons in the reactor core. The formation paths from the seed nuclei to $^{254}$Es are shown in Figure 4.2. Neutron capture and $\beta^-$ decay processes are repeated to reach $^{254}$Es. Through the reaction and decay network, only approximately one microgram of $^{254}$Es can be produced after about 6 months of irradiation.

The target was prepared at JAEA using $\sim$ 0.065 $\mu$g of $^{254}$Es (activity $\sim$ 4.5MBq). The einsteinium is chemically purified and electroplated into a backing made of natural nickel. The target spot diameter is about 1 mm (see Figure 4.3 (a)). Another layer of nickel backing is stacked up above as a protection layer. The thickness of the $^{nat}Ni$ backing is about $\sim$ 300 $\mu g/cm^2$ for both sides.

The target is mounted in a moveable ladder together with a viewer and a natural nickel target (as show in Figure 4.3 (b)). The viewer is made of a material that will glow under the beam irradiation. It is used to tune the beamline magnets and steerers for the beam transport while watching the position of the beam, to assure that the beam will

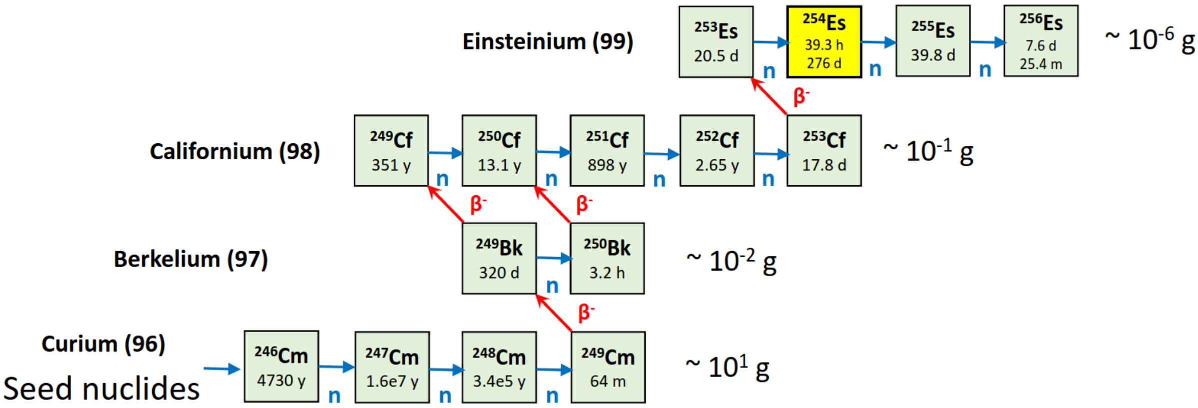


FIGURE 4.2: Path to produce $^{254}$Es in High Flux Isotope Reactor (HFIR) at Oak Ridge National Laboratory (ORNL), USA. $^{254}$Es is achieved through the consecutive neutron capture and $\beta^-$ decay processes.

(a) (b)

FIGURE 4.3: Photo of $^{254}$Es target (left) and target holder and silicon detector attached in the target chamber flange (right).The target holder was manually rotated from outside without breaking the chamber vacuum. Three positions are visible in the picture, corresponding to, from left to right, $^{nat}$Ni target, beam viewer and $^{254}$Es target.

hit the target. The nickel target was used to get a reference background particle spectrum. The energy of the scattered $^{58}$Ni nuclei that collided with $^{254}$Es nuclei is expected to be well separated from those that collided with nickel nuclei in the backing.

An experiment of $^{254}$Es is challenging since not only a small amount of material is available, but also it will decay over time (the target material almost halves its size within about 6 months). Furthermore, the large $\alpha$ and $\gamma$ radioactivity coming from the target causes a huge background in both particle and $\gamma$-ray spectra.

## 4.2 The JAEA Tandem accelerator

The tandem accelerator is a type of electrostatic accelerator that provides a two-step acceleration to ions using only one high-voltage terminal. Figure 4.4 is a schematic diagram of the JAEA-Tokai tandem accelerator. The high voltage is generated by carrying electric charges on running pellet chains to a high voltage terminal. There are two accelerator tubes from the ground to the terminal and vice versa. Negative ions produced in the negative ion source are pre-accelerated at the exit of the source. They are then transported to the entrance of the low energy accelerator tube and accelerated to the positive high-voltage terminal. A thin carbon foil, called electron stripper, is placed in the high-voltage end of the acceleration tube. Several electrons are removed from the negatively charged ions when they pass through the electron stripper. The ion, now positively charged, are accelerated again down to the exit.

The terminal voltage can be set at any value between 2.5 and 18 MV, and at this facility several ion species can be accelerated, from hydrogen to bismuth [39]. The tandem accelerator has some advantages compared with other types of accelerators:

- It is easy to vary the energy of ions, the energy can be set arbitrarily, and the energy accuracy is high (100 keV) [40].
- The beam size is small ($\sim$ 1 mm $\Phi$)[40].

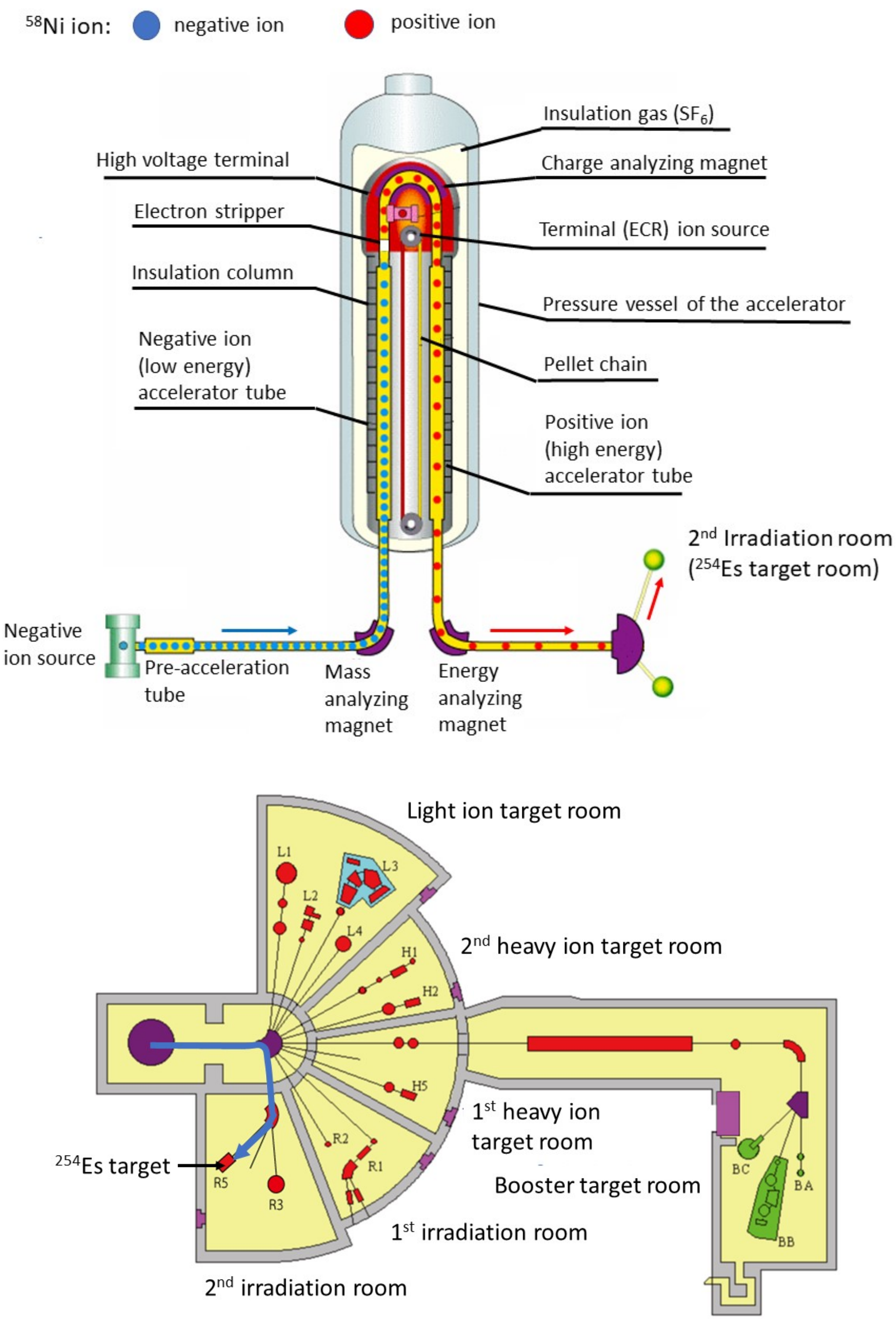


FIGURE 4.4: The structure of the tandem accelerator [39]. In this research, an 250 MeV $^{58}$Ni beam is used. The beam is transported to 2$^{nd}$ irradiation room where measurement of $^{254}$Es is performed.

## 4.3 Detector system

### 4.3.1 Gamma ray detectors


FIGURE 4.5: Experiment setup

The $\gamma$-ray detector array used in this work consists of 4 $LaBr_3$(Ce) scintillators, 4 coaxial HPGe detectors, and 4 Clover-type HPGe detectors. Figure 4.6 shows the setup of the gamma detectors array. Detectors are numbered (as shown in figure 4.6) for convenience in data storage and analysis. Clover detectors are multi-crystal detector of 4 coaxial crystal arranged like a four leaf clover (see figure 4.7). For Clover detectors, data are collected for each crystal, named S1 – S4 respectively.

The dimensions of coaxial HPGe detector crystals are 66 mm (diameter) by 75.2 mm (height). $LaBr_3$(Ce) detectors have a diameter of 101.5 mm and a height of 127 mm. They are placed in a plane perpendicular to the beam axis (see figure 4.6). Clover detectors can be approximated to a rectangular shape with dimensions of 109.6 mm $\times$ 109.6 mm $\times$ 90 mm. Clover detectors are placed in the horizontal plane at 55° and 125° with respect to the beam axis.

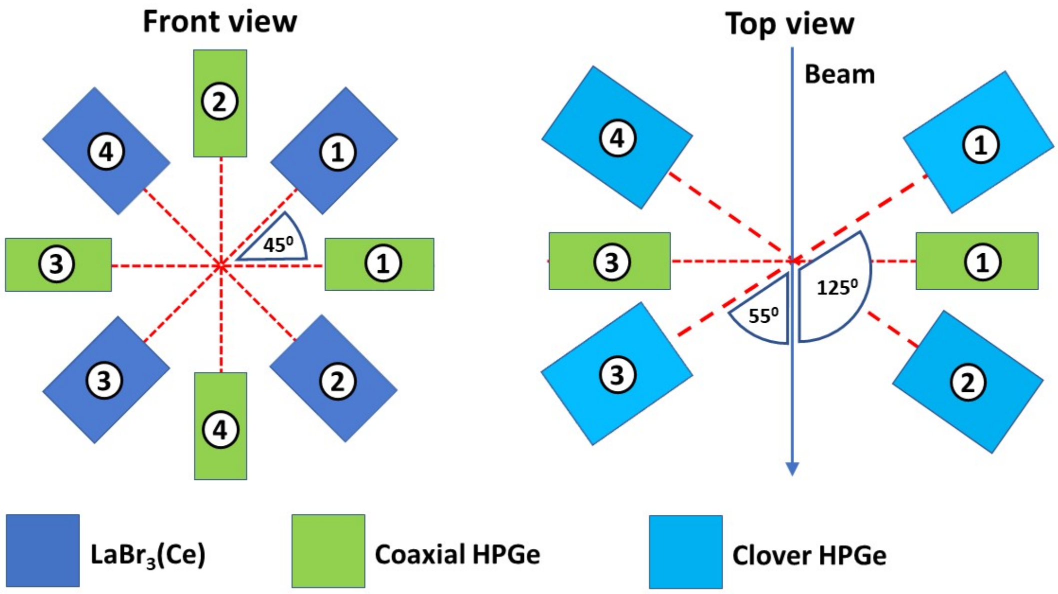


FIGURE 4.6: Gamma detectors configuration from the front view (left) and the top view (right). The number indicate the detector ID used in data storage and analysis.

HPGe detectors provide excellent energy resolution (FWHM 2.5 keV (0.26 %) ~4.2 keV (0.44 %) at 964.8 keV) which is crucial in searching for new $\gamma$-ray transitions, especially in a high-background, low-statistics experiment.

Meanwhile, the large volume $LaBr_3$(Ce) scintillators (2.36 times of the volume of coaxial HPGe detector), in spite of worse energy resolution (FWHM 22.21 keV (2.3 %) — 24.21 keV (2.5 %) at 964.8 keV) and the presence of intrinsic background, give an appreciable increase to the total $\gamma$-ray detection efficiency. The intrinsic background in the scintillator is caused by the presence of naturally occurring radioactive isotope $^{138}$La. This isotope emits $\gamma$ rays and beta particles, as shown in figure 4.8. The presence of the intrinsic background can limit the sensitivity of the detector for low-energy $\gamma$ rays, and also affect the energy resolution and linearity of the detector.

A summary of energy resolution and geometrical configuration of detectors is shown in table 4.1.

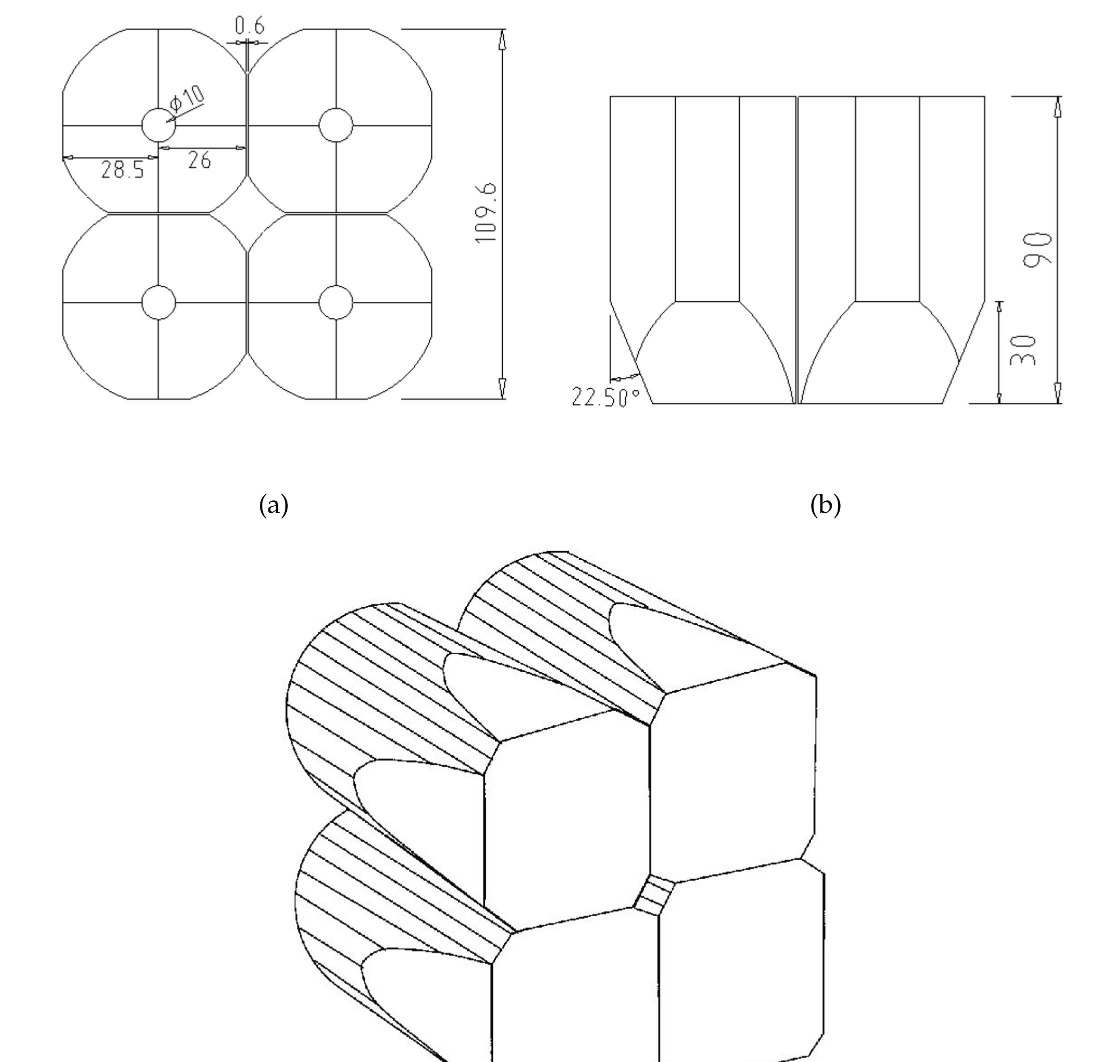


FIGURE 4.7: Geometry of Clover detector. (a) and (b) Sectional draw of Clover crystal. Dimension is in mm. (c) 3-D draw of a Clover crystal.

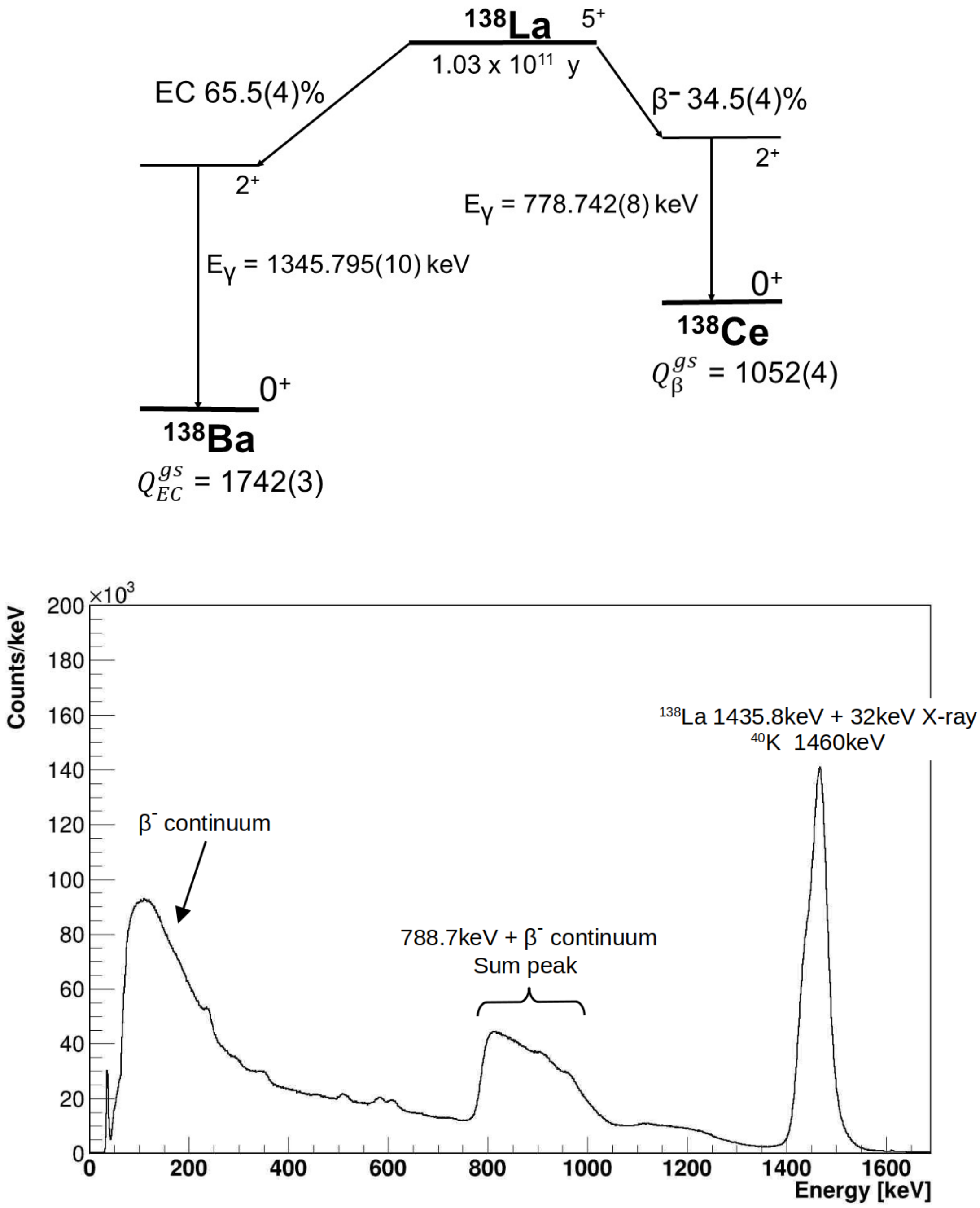


FIGURE 4.8: Decay scheme of $^{138}$La. Data taken from [41] (top) and background spectrum of LaBr3(Ce) detector used in this experiment. Intrinsic background from $^{138}$La decay is indicated (bottom).

TABLE 4.1: Energy resolution (FWHM) and geometrical configuration of $\gamma$-ray detectors (crystals). Distance from target point to the detector surface and its ($\theta$, $\phi$) angles to the beam direction are shown. Resolution values at 244 keV ($^{133}$Ba) and 964.8 keV ($^{154}$Eu) which measured at the end of the experiment, are shown.

| Detector | | Position | | | FWHM (keV) | |
|---|---|---|---|---|---|---|
| | | Distance (cm) | $\theta$ angle | $\phi$ angle | at 244 keV | at 964.8 keV |
| Coaxial HPGe | 1 | 15.8 | 0 | 0 | 2.93 | 3.47 |
| | 2 | 14.1 | 0 | 90 | 2.46 | 3.03 |
| | 3 | 16.1 | 0 | 180 | 2.64 | 3.21 |
| | 4 | 15.1 | 0 | 270 | 1.84 | 2.50 |
| Scintillator | 1 | 18.4 | 0 | 45 | 11.96 | 22.21 |
| | 2 | 18.2 | 0 | 135 | 12.51 | 22.24 |
| | 3 | 18.5 | 0 | 225 | 14.34 | 24.17 |
| | 4 | 18.5 | 0 | 315 | 14.63 | 24.21 |
| Clover HPGe 1 | S1[1] | 16.8 | 134.2 | 9.2 | 3.14 | 7.09 |
| | S2 | | 134.2 | 350.8 | 2.28 | 4.09 |
| | S3 | | 115.8 | 350.8 | 2.77 | 3.79 |
| | S4 | | 115.8 | 9.2 | 2.40 | 4.20 |
| Clover HPGe 2 | S1 | 16.8 | 64.2 | 9.2 | 2.47 | 3.46 |
| | S2 | | 64.2 | 350.8 | 3.83 | 4.13 |
| | S3 | | 45.8 | 350.8 | 2.52 | 3.32 |
| | S4 | | 45.8 | 9.2 | 2.33 | 3.40 |
| Clover HPGe 3 | S1 | 16.8 | 45.8 | 170.8 | 1.94 | 3.47 |
| | S2 | | 45.8 | 189.2 | 1.95 | 3.25 |
| | S3 | | 64.2 | 189.2 | 1.90 | 3.01 |
| | S4 | | 64.2 | 170.8 | 1.89 | 3.29 |
| Clover HPGe 4 | S1 | 16.8 | 115.8 | 170.8 | 1.98 | 2.67 |
| | S2 | | 115.8 | 189.2 | 1.95 | 2.61 |
| | S3[2] | | 134.2 | 189.2 | — | — |
| | S4 | | 134.2 | 170.8 | 2.03 | 2.75 |

[1] Crystal S1 of Clover No.1 has large energy resolution because of electronic issue

[2] Crystal S3 of Clover No.4 detector is broken

### 4.3.2 Particle detectors

The experiment used two S3-type Si detectors [42] as shown in Figure 4.6. The S3 detector type has a circular shape with a central hole, therefore is referred to as a CD detector. S3 is a double-side segmented silicon detector. On one side, referred to as the sector side, the disk is divided into 32 radial sectors of 11.25° each. On the other side, referred to as the ring side, from the 11 mm inner radius to the outer radius of 35 mm, the detector is segmented into 24 annular rings with 1-mm width of each ring (as shown in Figure 4.9). The thickness of the detector is ~300 $\mu$m, which is sufficient to stop either the beam scattered nuclei or target recoil nuclei.

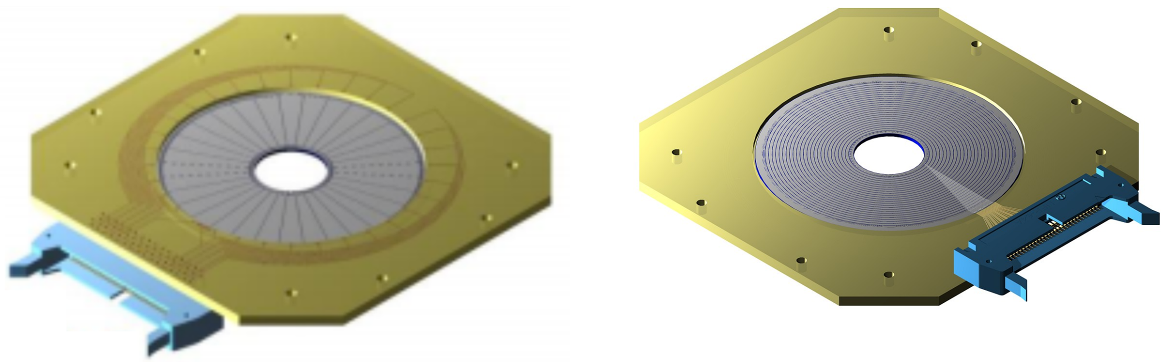

(a) Sector side

(b) Ring side

FIGURE 4.9: The S3-type CD Silicon detector [42]

Under the beam irradiation, the target is heated up, and the radioactive $^{254}$Es (and its daughter nucleus) may evaporate and sputtering into the chamber space. This posed a risk of contaminating the equipments in the target chamber. Therefore, a 0.5 $\mu$m polyethylene film was placed in front of the detector to prevent the potential radioactive contamination, meanwhile scattering particles still able to pass through with a negligible energy loss and straggling.

One thing need to be attentive when operating the particle detector is the leak current, which is the flow through the detector even in the absence of any incident particle. The leakage current is caused by the thermal generation of electron-hole pairs

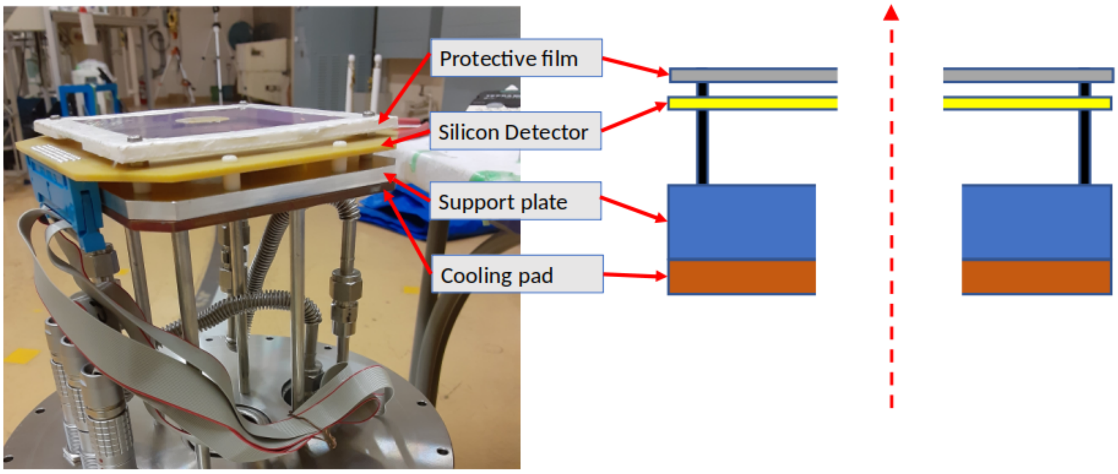


FIGURE 4.10: The installation of a backward silicon detector with protective film, support plate made of aluminum and cooling plate made of copper. Ethanol solution is used to cool the detector down to -20°C. The forward silicon detector is installed similarly without cooling plate

in the semiconductor material. It is influenced by several factors such as temperature, radiation damage, and impurities in the material. In the experiment, under continuous irradiation of the intense alpha decay and scattered beam particles, the leak current of the silicon detectors gradually builds up due to the accumulation of radiation damage and impurities in the semiconductor material. The high leak current may affect the detector performance as it contributes to the background noise in the detector, which can reduce its sensitivity and resolution. This can also damage the detector, shorten its life, and affect its stability over time.

The effects of leakage current can be reduced by reducing the detector temperature. This reduces the thermal generation of electron-hole pairs and can help to minimize the build-up of leakage current over time. In this experiment, a cooling circuit using water/ethanol solution was applied to the backward silicon detector. Due to the chamber geometrical constraints, the cooling circuit could not be installed for the forward Si detector. An approximately 60% reduction of leak current was observed with the cooling temperature of - 20°C compared to the leak current at room temperature ($\sim$ 20°C) as shown in Figure 4.11. The voltage applied to the detector need to be above a saturation value, where the depleted zone of the detector maximized, and the signal only depend on the energy of incident particle. The leak current build-up decreases the actual voltage applied and at some point will go below the saturation voltage. Therefore, the applied voltage is gradually increased to counter this effect.

The detectors were placed 30 mm forward and 27 mm backward to the target position, covering the angle from 20.13° to 48.58° and from 128.45° to 157.83°, respectively.

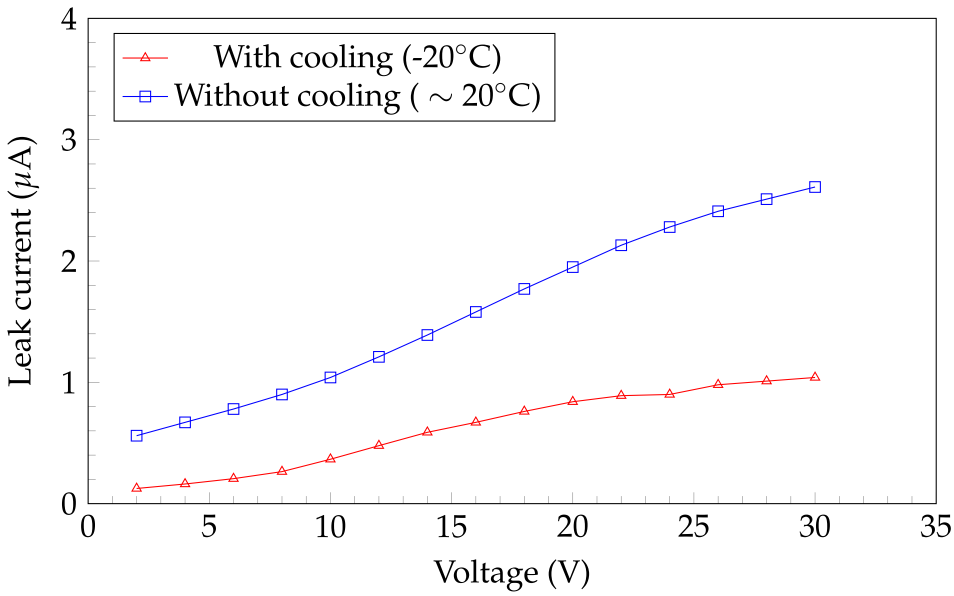


FIGURE 4.11: Leak current of Silicon detector as dependence of applied voltage with and without cooling.The measurement is taken at the beginning of the experiment. The $^{254}$Es target is mounted in the chamber; and the beam is off. The detector is only irradiated by $\alpha$ particles from $^{254}$Es decay.

The forward and backward positions are defined by the beam direction, forward corresponds to downstream and backward to upstream.

Unfortunately, only the ring-side read-out of the detectors were collected due to the limited number of channels available in the data-acquisition system. During the experiment, probably due to the large irradiation and lack of cooling, the signals from the forward detector were found to be abnormal and not sufficient for data analysis. Therefore, only the results from the backward detector data are presented in this thesis.

### 4.3.3 Data acquisition system

The data acquisition system was employed to collect both energy and timing information of each output channel of the detector system, as well as to record the beam

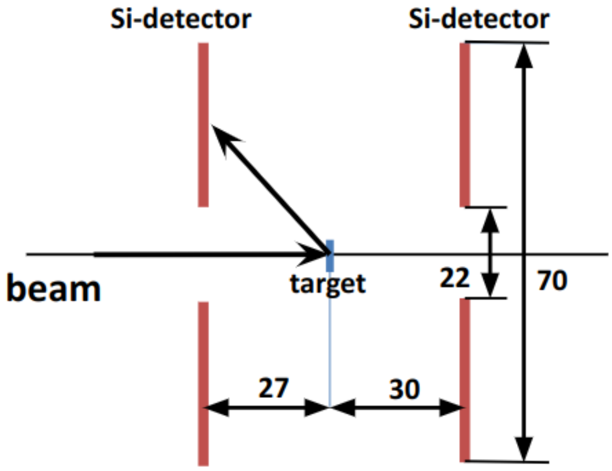


FIGURE 4.12: Silicon detector geometry

current measured by a Faraday cup placed at the end of the beam line. Figure 4.13 shows the diagram of the electronic system.

The signals from detectors after amplification via preamplifier/photomultiplier are collected by Pulse to Digital Converter(PDC) module, which records the pulse height and provides a timestamp for each signal. The time step interval of the timestamp is 200 ns.

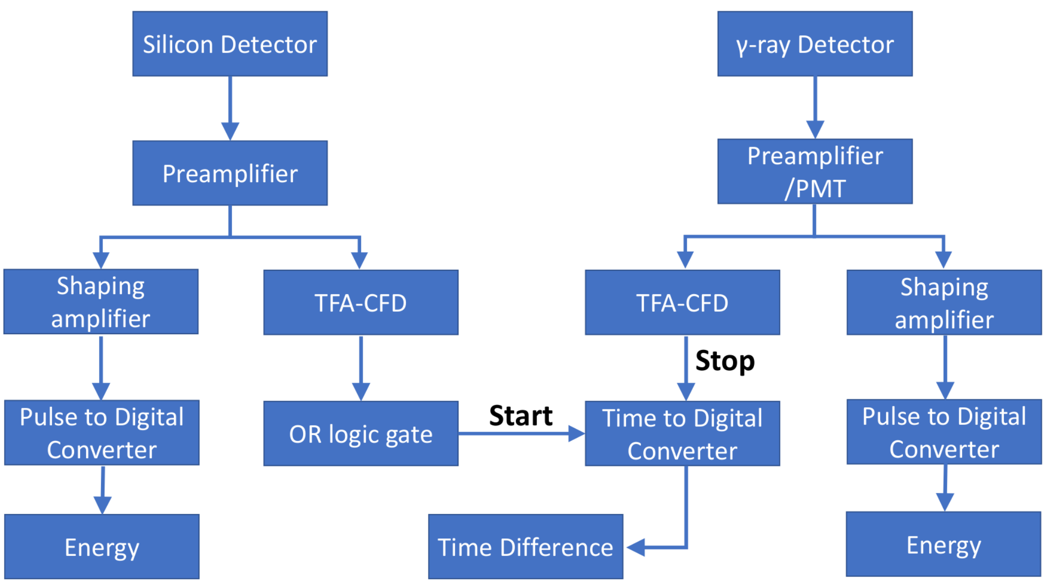


FIGURE 4.13: The block diagram of the electronic modules used in the experiment

In parallel, for more precise timing information, the signals are processed through the Timing Filter Amplifier—Constant Fraction Discriminator (TFA-CFD). The signal of silicon detectors after the preamplifier is amplified by TFA and discriminated by CFD to create timing logic signals and then go to an "OR logic gate". The output from the logic gate is used as the start signal of the Time to Digital Converter (TDC). The signal of HPGe detectors or $LaBr_3$(Ce) scintillator also go through TFA and CFD modules and then set as the stop signal of TDC. The TDC module records the time difference between a gamma detector signal and a silicon signal: pulse height $\propto |t_{particle} - t_\gamma|$. The TDC range is $\sim$1600 ns. Each TDC channel is set up to record the time relation data between one $\gamma$-ray detector/segment and one silicon detector (as sum of signal from all 24 rings).

In this chapter, the experimental facilities and apparatus used in the experiment described in this thesis were discussed. The following chapter will present how the data collected in the experiment were analyzed.

# Chapter 5

# Data Analysis and Results

In this chapter, the data analysis and results of the $^{254}$Es Coulomb excitation experiment will be presented. The first section introduces the energy and efficiency calibration of $\gamma$-ray spectra of the HPGe and LaBr$_3$(Ce) detectors, as well as and the time calibration and alignment of the time spectra obtained using TDC modules. The second section shows the event-selection methods and processes used to obtain the Coulomb excitation $\gamma$-ray spectrum of $^{254}$Es. The third section focuses on the analysis of the $\gamma$-ray spectra, and how the observed peaks were interpreted to gain information about the level scheme of $^{254}$Es. The spin-parity of the excited states connecting by the newly found $\gamma$-ray transitions were assigned. The level scheme which includes newly observed transitions is built. The final section describes the GOSIA to deduce the matrix elements involved in Coulomb excitation of $^{254}$Es.

## 5.1 Calibrations

### 5.1.1 Gamma-ray energy calibration

The energy calibration of the $\gamma$ ray spectra obtained in this experiment was performed using the standard $\gamma$ rays calibration sources $^{152}$ Eu and $^{133}$ Ba (tabulated in Table 5.2). The calibration has been tested with the linear and quadratic fit. The non-linearity of the electronic system was visible in the $\gamma$-ray spectrum of both HPGe and LaBr$_3$(Ce) detector as a deviation of the peak energies to the literature values depending on the order of the fit. For example, Figure 5.1 and 5.2 show the deviation

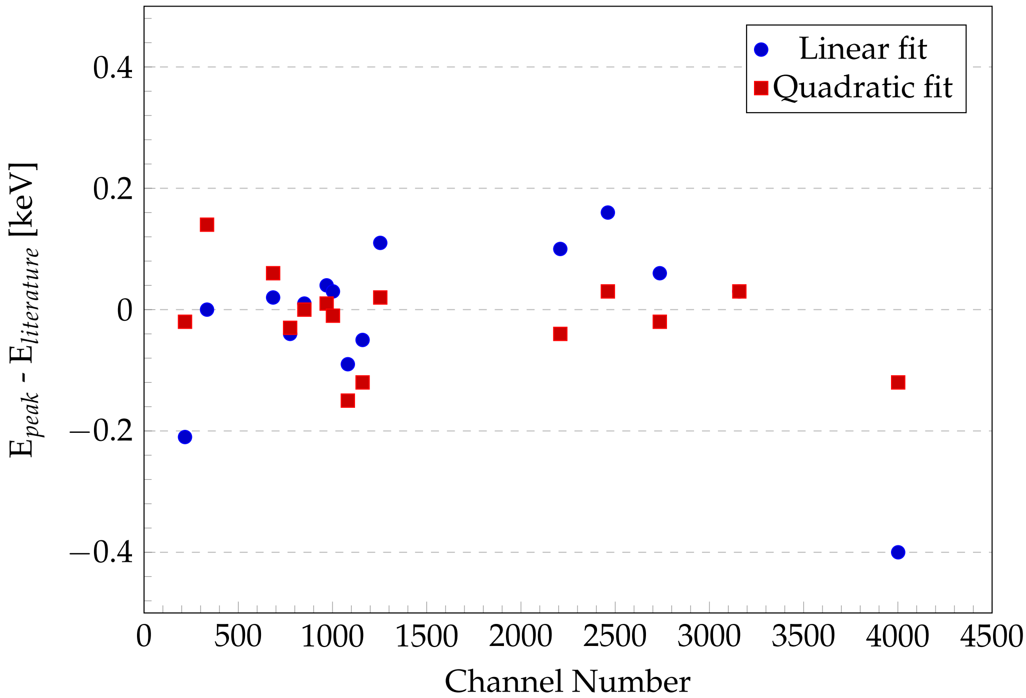


FIGURE 5.1: The deviation of the calibrated peak energies to the literature values of $\gamma$ rays of calibration sources ($^{154}$Eu and $^{133}$Ba) in the $\gamma$ ray spectrum of coaxial HPGe detector No.2. The energies $E_{peak}$ are calculated from fit with a linear and quadratic fit.

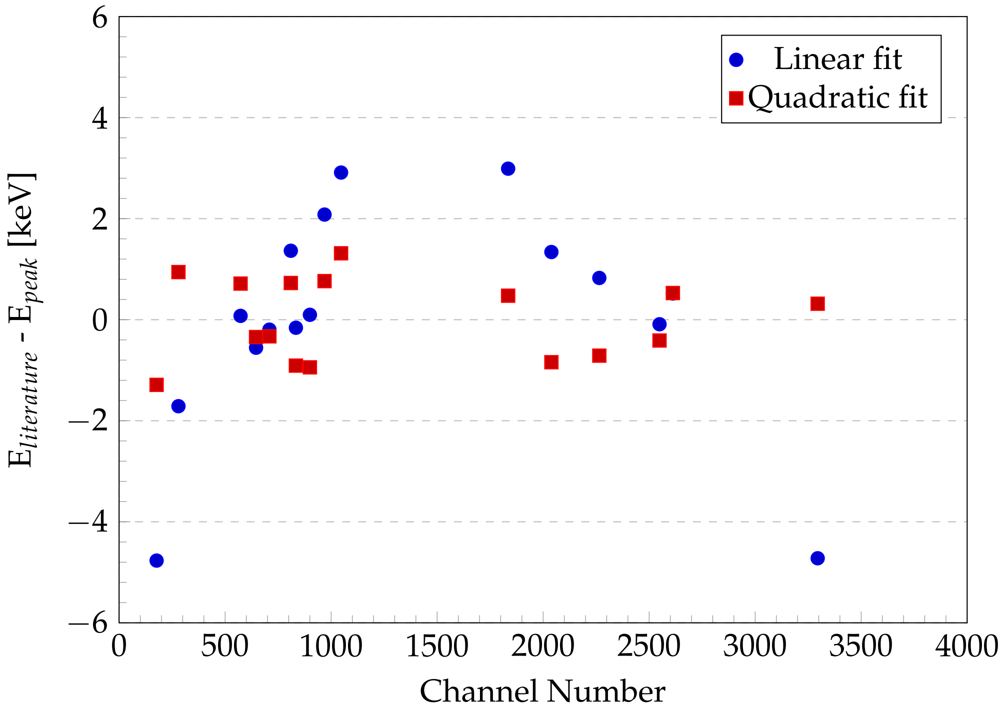


FIGURE 5.2: Same as Figure 5.1 but for $LaBr_3$(Ce) detector No.1

of between the fitted and measured energies in the coaxial HPGe detector No.2 and LaBr3(Ce) detector No.1 $\gamma$-ray spectra, respectively. The calibration with the quadratic fit gives smaller deviation than the one with linear function. Therefore, the calibration with the quadratic fit was applied to the experimental data.

TABLE 5.1: $\gamma$-rays used for $\gamma$-ray detector energy calibration

| Isotope | Energy [keV] | | Intensity [%] | |
|---|---|---|---|---|
| $^{254}$Es | 61.89[43] | 0.01 | 2.17 | 0.11 |
| $^{250}$Cf | 889.956[44] | 0.022 | 1.53 | 0.04 |
| $^{250}$Cf | 929.468[44] | 0.022 | 1.23 | 0.03 |
| $^{250}$Cf | 989.125[44] | 0.021 | 45 | |
| $^{250}$Cf | 1031.852[44] | 0.021 | 35.6 | 0.8 |
| $e^-$ - $e^+$ annihilation peak | 511 | | | |

During the experiment, however, small shifts in the gain were observed mainly for the $LaBr_3$(Ce) scintillators, more sensitive to temperature changes, but also for the HPGe detectors. If uncorrected, these shifts worsen the detector resolution and also introduce uncertainties in the measured energy of the observed peaks. As can be seen in Figs 5.3 and 5.4, due to the high radioactivity of the target, even during beam irradiation the $\gamma$-ray spectra are dominated by the radioactivity of the Es target. For example, the Figure 5.5 shows the change of the peak position of the two strongest peaks from the Es decay, respectively 1031.8 keV and 989.1 keV, for one of the $LaBr_3$(Ce) scintillators. In order to correct for the gain shift, the raw data were divided in 500-MB sub-files, and in each sub-file the shifts were corrected by recalibrating the spectra using the $\gamma$ rays tabulated in Table 5.1 and shown in Figure 5.3 and 5.4).

### 5.1.2 Gamma efficiency calibration

As described in Chapter 3, in a Coulomb excitation experiment, the intensities of the $\gamma$ rays from the excited target depend on the scattering angle of the projectile. This

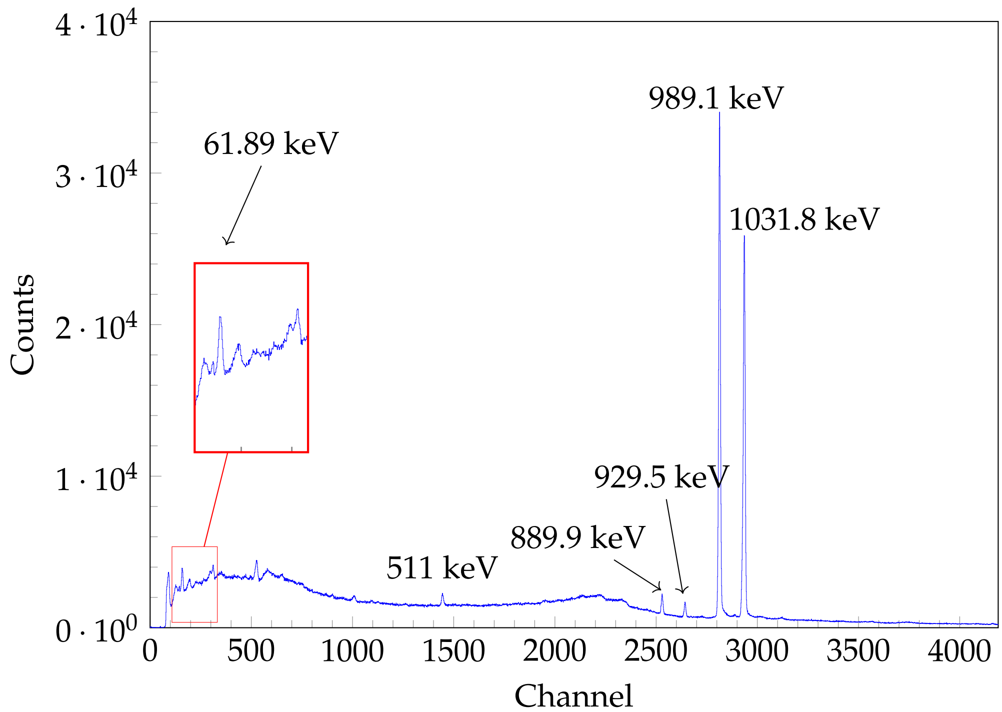


FIGURE 5.3: Spectrum of detector coaxial HPGe 1 before calibration. Peaks used for energy calibration are labeled by their energy.

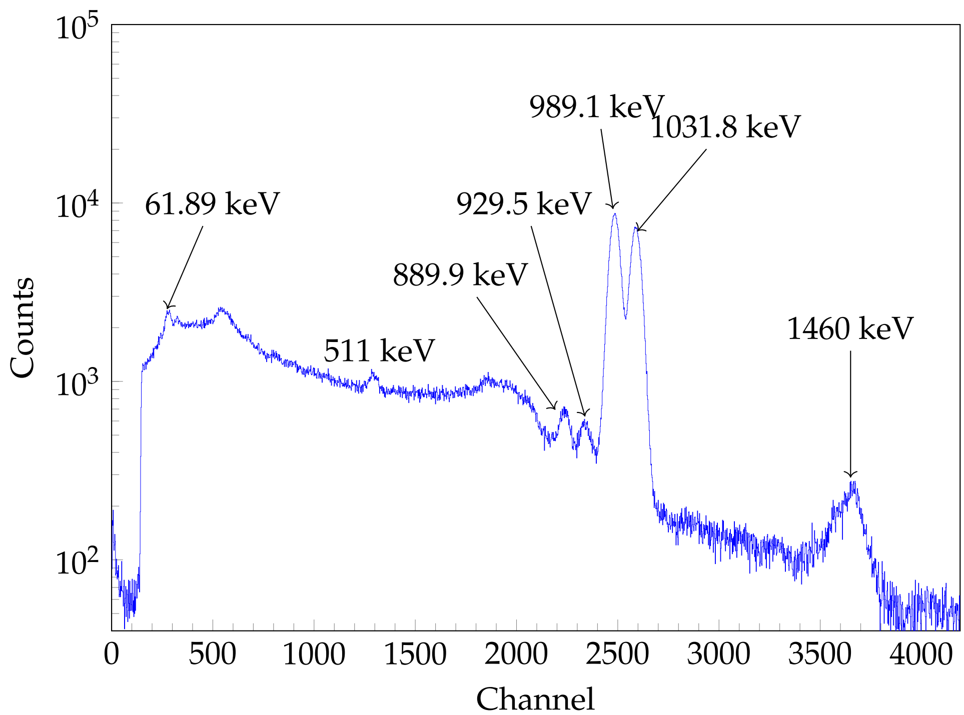


FIGURE 5.4: Spectrum of detector $LaBr_3$(Ce) 1 before calibration. Peaks used for energy calibration are labeled by their energy. The 1460-keV peak comes from the self-radioactivity of the $LaBr_3$(Ce) scintillator.

variation of intensity, or yield, as a function of angle is of primary importance to determine the transition matrix elements. In order to obtain the gated spectra for different angles, it is necessary first to determine the $\gamma$-ray detection efficiency.

The measurement was taken at the end of the experiment to determine the efficiency curve of the detector array. Sources of $^{152}$Eu and $^{133}$Ba were placed at the target position, giving data points as low as 80 keV and as high as 1408 keV (see Table 5.2). The energies and intensities are listed in Table 5.2. In addition to this standard efficiency calibration, however, the further drop in efficiency due to the coincidence detection of the scattered beam particle is necessary. Because the particle detector does not cover $4\pi$ solid angle and the particle-$\gamma$ angular distribution is anisotropic, the detection efficiency of the detector array when taking particle-$\gamma$ coincidence is smaller than that without particle-$\gamma$ coincidence. Also, the efficiency needs to be corrected for the dead time in the data acquisition caused by the high counting rates induced by the large target radioactivity. The different factors taken into account in estimating the detection efficiency are summarized in Equation 5.1.

$$\epsilon(E) = \frac{N(E)}{AI(E)t} * \frac{T_{live}}{T_{real}} * R_{p-\gamma/\gamma}(E), \tag{5.1}$$

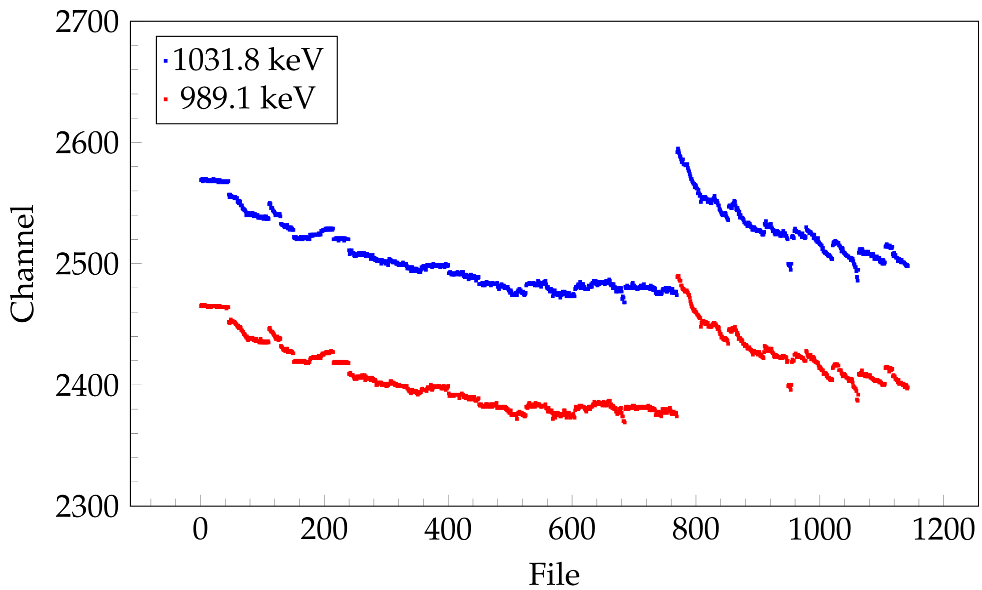


FIGURE 5.5: Gain shift of detector LaBr$_3$(Ce) 1. Peak position of the 989.1 keV and 1031.8 keV peak for each sub-file(~500 MB size) are shown.

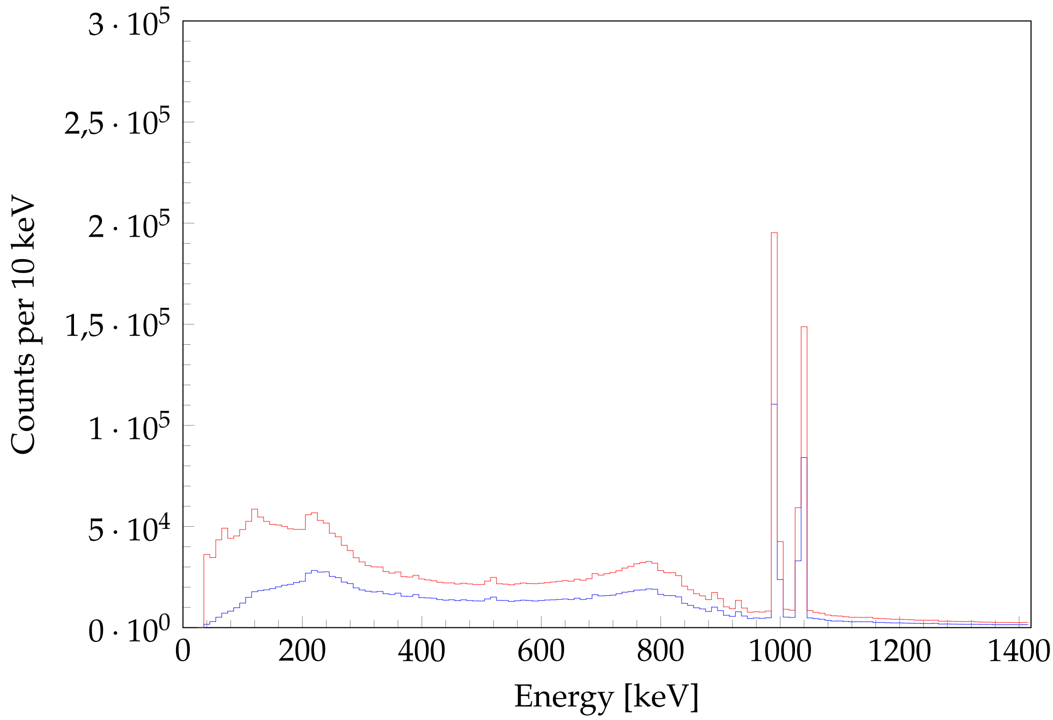


FIGURE 5.6: Comparison of $\gamma$-ray spectrum (red) and p-$\gamma$-ray spectrum (blue) of all coaxial HPGe detectors. The drop in efficiency is more severe in the low-energy region (roughly below 300 keV) of the p-$\gamma$ ray spectrum, possibly due to non-optimal settings of the CFD delays.

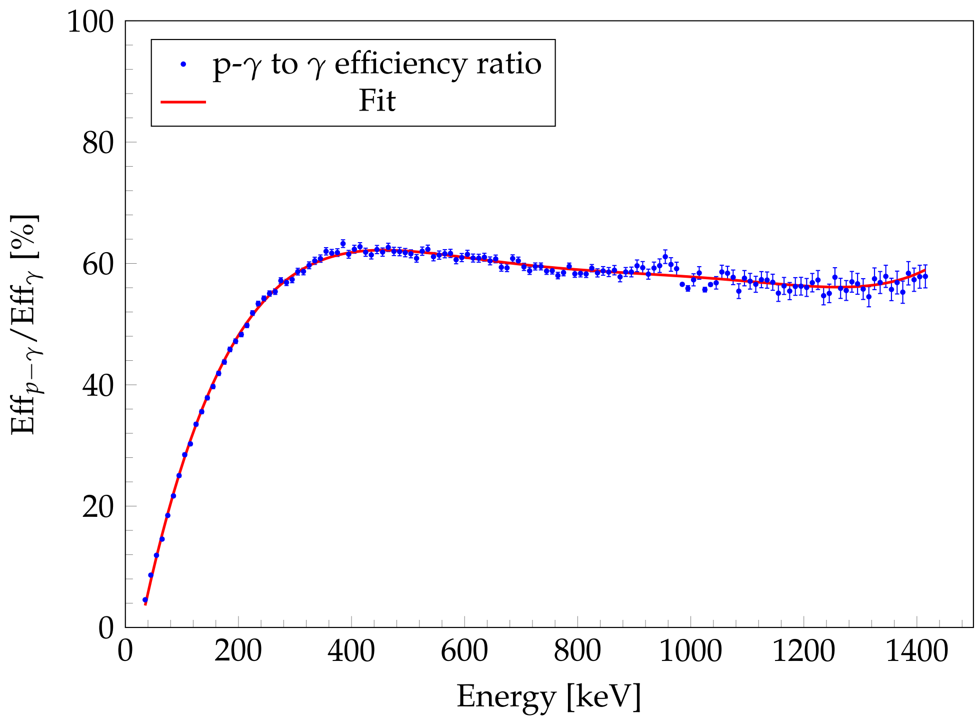


FIGURE 5.7: Estimated reduction in detection efficiency of all Coaxial HPGe detectors when requiring particle-gamma coincidences.

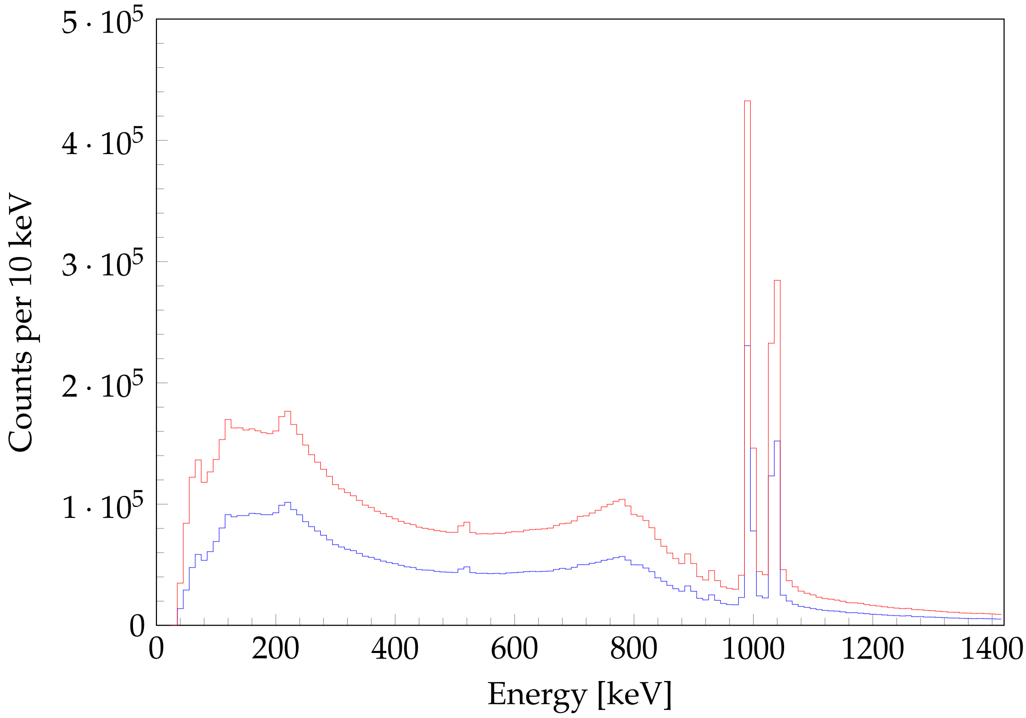


FIGURE 5.8: Comparison of $\gamma$-ray spectrum (red) and p-$\gamma$-ray spectrum (blue) of all Clover HPGe detectors.

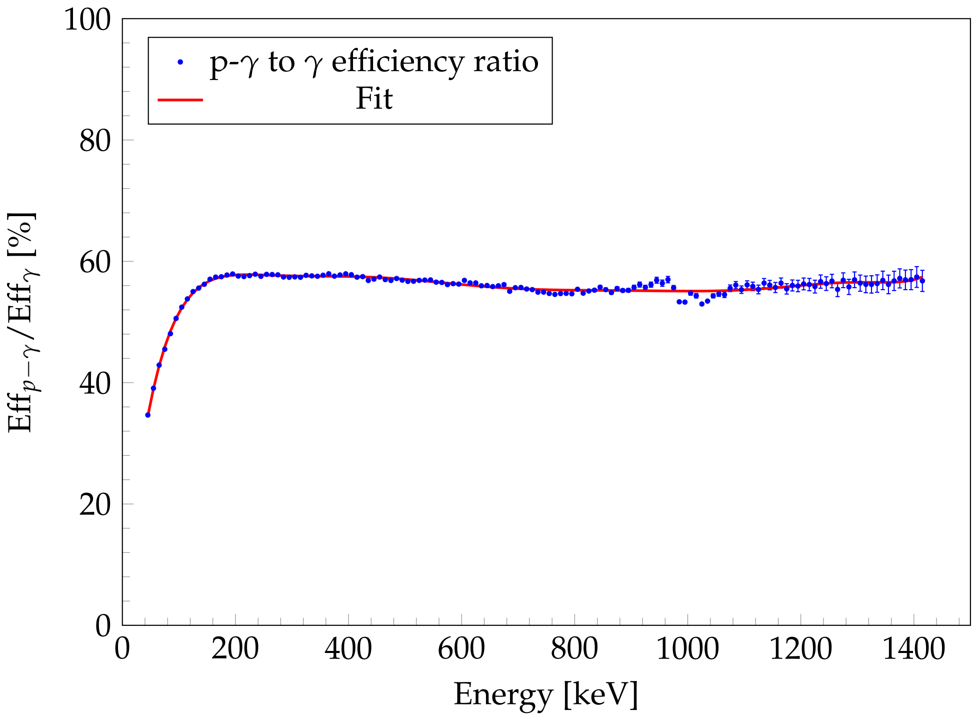


FIGURE 5.9: Estimated reduction in detection efficiency of all Clover HPGe detectors when requiring particle-gamma coincidences.

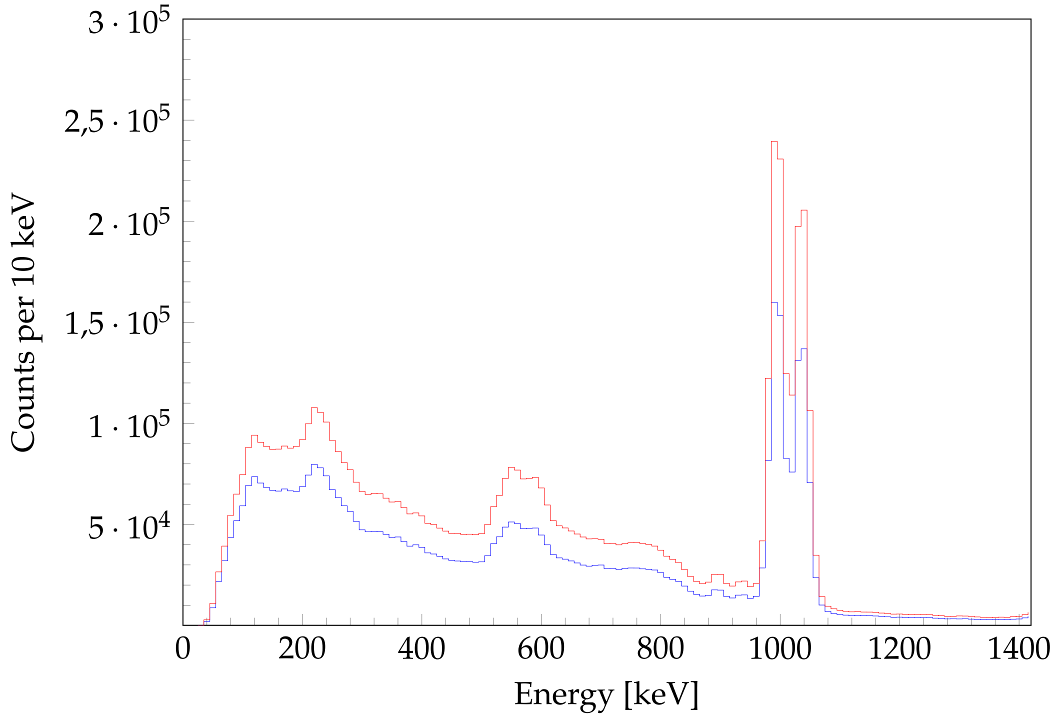


FIGURE 5.10: Comparison of $\gamma$-ray spectrum (red) and p-$\gamma$-ray spectrum (blue) of all $LaBr_3$(Ce) detectors.

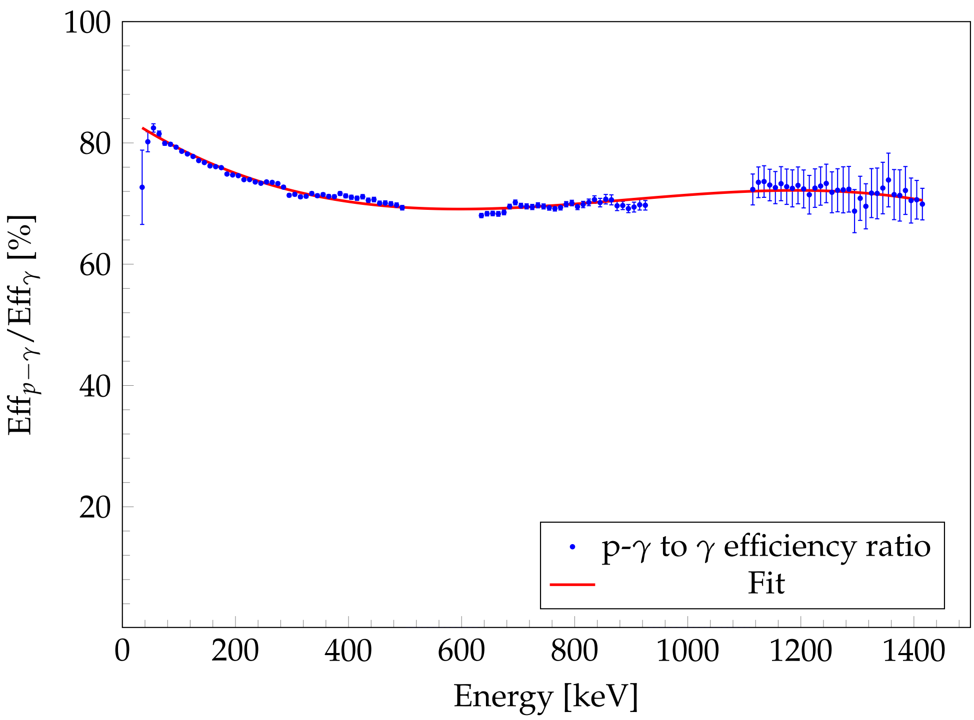


FIGURE 5.11: Estimated reduction in detection efficiency of all $LaBr_3$(Ce) detectors when requiring particle-gamma coincidences.

TABLE 5.2: Gamma-ray energies of $^{133}$Ba and $^{152}$Eu [45] used for $\gamma$-ray efficiency calibration. The 1408 keV peak is excluded in the calibration of $LaBr_3$(Ce) spectrum as it overlaps with the 1432 keV intrinsic background peak.

| Isotope | Energy [keV] | | Intensity [%] | |
|---|---|---|---|---|
| $^{133}$Ba | 81.00 | 0.0030 | 34.06 | 0.27 |
| $^{152}$Eu | 121.78 | 0.0021 | 28.58 | 0.06 |
| $^{133}$Ba | 160.61 | 0.0080 | 0.65 | 0.08 |
| $^{133}$Ba | 223.23 | 0.0120 | 0.45 | 0.04 |
| $^{152}$Eu | 244.70 | 0.0010 | 7.58 | 0.19 |
| $^{133}$Ba | 276.40 | 0.0020 | 7.16 | 0.22 |
| $^{133}$Ba | 302.85 | 0.0010 | 18.33 | 0.06 |
| $^{152}$Eu | 344.28 | 0.0020 | 26.5 | 0.40 |
| $^{133}$Ba | 356.02 | 0.0020 | 62.05 | 0.19 |
| $^{133}$Ba | 383.85 | 0.0030 | 8.94 | 0.03 |
| $^{152}$Eu | 411.12 | 0.0050 | 2.23 | 0.04 |
| $^{152}$Eu | 443.98 | 0.0050 | 2.82 | 0.19 |
| $^{152}$Eu | 778.90 | 0.0060 | 12.94 | 0.19 |
| $^{152}$Eu | 867.39 | 0.0080 | 4.25 | 0.19 |
| $^{152}$Eu | 964.13 | 0.0090 | 14.61 | 0.21 |
| $^{152}$Eu | 1112.12 | 0.0170 | 13.64 | 0.21 |
| $^{152}$Eu | 1408.01 | 0.0140 | 21.01 | 0.24 |

where

- N(E) is the number of counts in the full-energy peak.
- A is the activity of the calibration source.
- I(E) is the emission probability of the $\gamma$ ray.
- t is the calibration time.
- $\frac{T_{live}}{T_{real}}$ is the ratio between $T_{live}$: the time when the DAQ system was able to record signals and $T_{real}$ is the time passed [1]. The $T_{live}/T_{real}$ ratio takes account for the

[1] The **measurement time** is the time when the $^{58}$Ni beam hit the $^{254}$Es target and the data is recorded. This is different from **calibration time**, of which $\gamma$ ray data from calibration source is recorded.

dead time effect, which in this experiment was, on average, 82% for coaxial HPGe detectors, 72% for Clover HPGe detectors and 97% for $LaBr_3$(Ce) detectors.

- $R_{p-\gamma/\gamma}(E)$ is the ratio between the $\gamma$ ray detection efficiency with and without coincident detection of particles. During the data analysis, it was found that this ratio is strongly dependent on the $\gamma$-ray energy, especially in the case of coaxial Ge detectors. This energy-dependent ratio was obtained from the data by comparing the raw in-beam $\gamma$ ray spectra to those resulting by requiring that a coincident signal was also recorded by the TDC (a signal in the TDC means that at least 1 particle and 1 $\gamma$-ray were recorded within the TDC time window, i.e., $\sim$ 1600ns). The ratios obtained by comparing the spectra shown in Figures 5.6, 5.8, 5.10 are shown, respectively, in Figures 5.7, 5.9, 5.11.

The efficiency curves, after the correction of reductions described above, were parameterized using the function :.

$$\epsilon(E) = exp\left[\sum_{k=0}^{n} a_k \left(ln\frac{E}{E_0}\right)^k\right]. \tag{5.2}$$

where $\epsilon(E)$ is the efficiency, $a_k$ are free parameters, and $E_0$ = 50 keV is a constant. For coaxial and Clover HPGe detectors, n=3 is used and for $LaBr_3$(Ce) detectors, n=2. The resulting fit parameters and their respective errors are listed in Table 5.3 and the efficiency curves shown in Figures 5.12, 5.13, 5.14 and 5.15.

TABLE 5.3: Tabulated efficiency parameters of Equation 5.2 describing the fitted curves for all coaxial HPGe detectors, all Clover HPGe detectors, and all $LaBr_3$(Ce) detectors, shown in Figures 5.12, 5.13, 5.14 and 5.15.

| | All coaxial HPGe | All Clover HPGe | All $LaBr_3$(Ce) |
|---|---|---|---|
| $a_0$ = | -1.959 $\pm$ 0.041 | -0.618 $\pm$ 0.083 | 1.312 $\pm$ 0.0662 |
| $a_1$ = | 2.798 $\pm$ 0.098 | 1.683 $\pm$ 0.198 | -0.169 $\pm$ 0.072 |
| $a_2$ = | -1.322 $\pm$ 0.063 | -1.012 $\pm$ 0.124 | -0.030 $\pm$ 0.020 |
| $a_3$ = | 0.163 $\pm$ 0.011 | 0.143 $\pm$ 0.022 | |

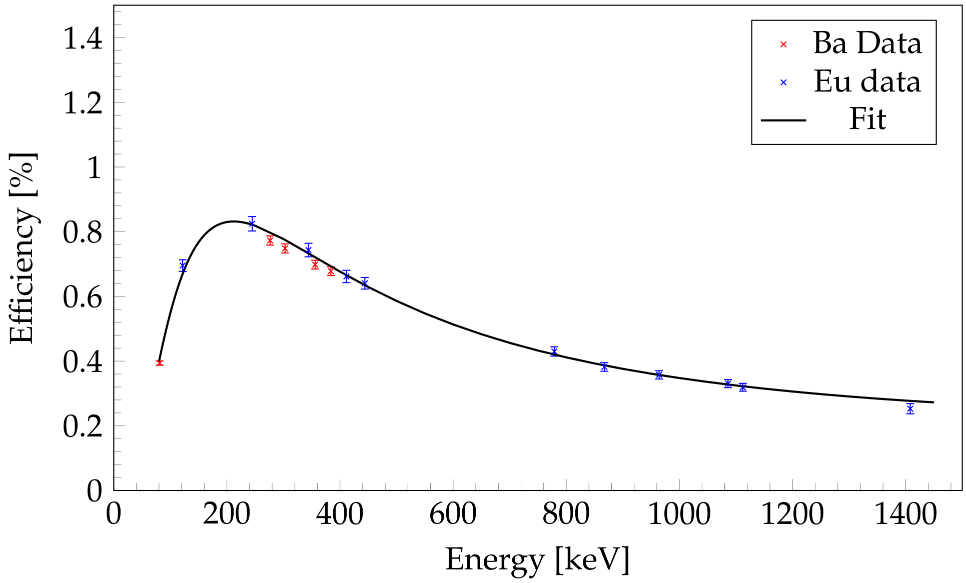


FIGURE 5.12: Efficiency curve of all $LaBr_3(Ce)$ detectors with data point for $^{133}$Ba (red), $^{152}$Eu (blue) and the fitting curve (black).

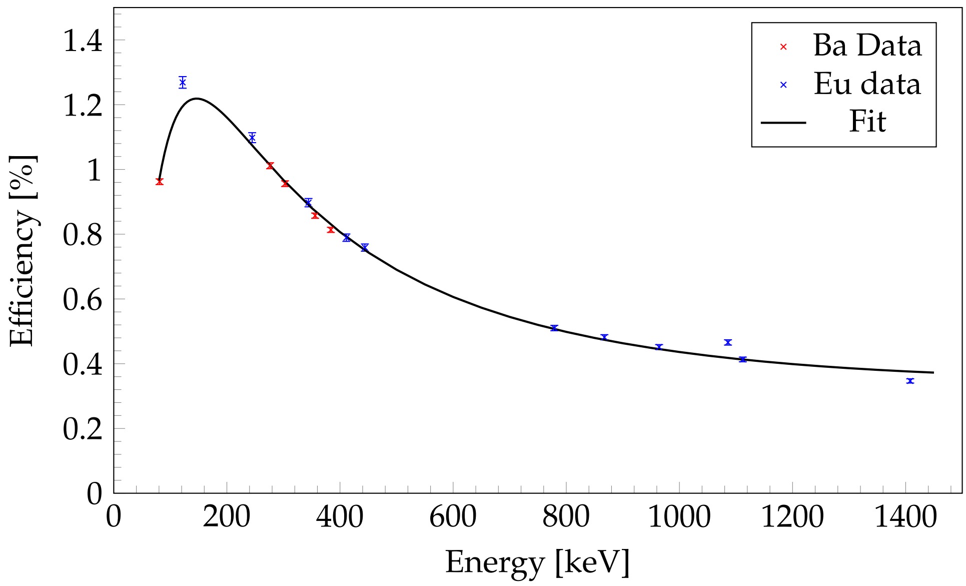


FIGURE 5.13: Efficiency curve of all Clover HPGe detectors with data point for $^{133}$Ba (red), $^{152}$Eu (blue) and the fitting curve (black).

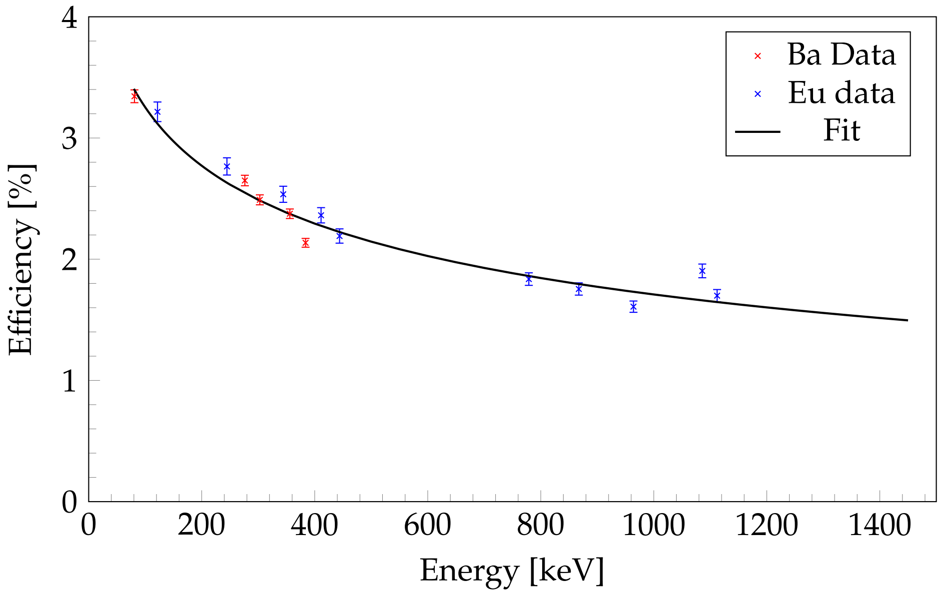


FIGURE 5.14: Efficiency curve of all coaxial HPGe detectors with data point for $^{133}$Ba (red), $^{152}$Eu (blue) and the fitting curve (black).

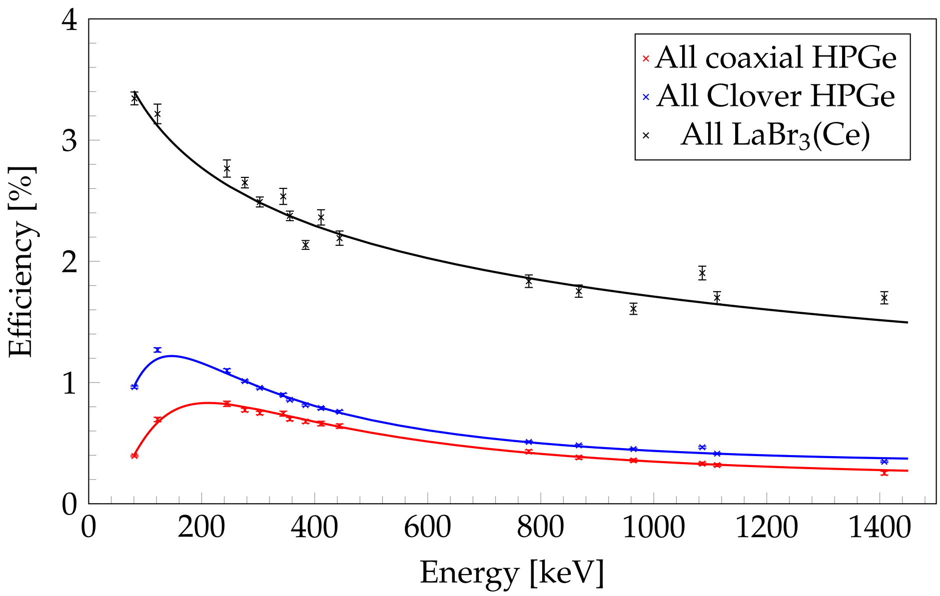


FIGURE 5.15: Efficiency curve of all coaxial HPGe (red), all Clover HPGe (blue) and all $LaBr_3$(Ce) detectors (black) and the associate fitting curves.

### 5.1.3 Time calibration and alignment

As presented in chapter 4, the time relation between a particle event and a $\gamma$-ray event is recorded by the TDC module: pulse height $\propto |t_\gamma - t_{particle}|$. The time signals are calibrated using the ORTEC 462 Time Calibrator. The module correlate the start and stop pulses, resulting peaks in the TDC spectrum separated by a constant period, and hence yield the timescale calibration. To calibrate the TDC spectra, the period was set to 10 ns. Figure 5.16 shows an example of the time calibration spectrum.

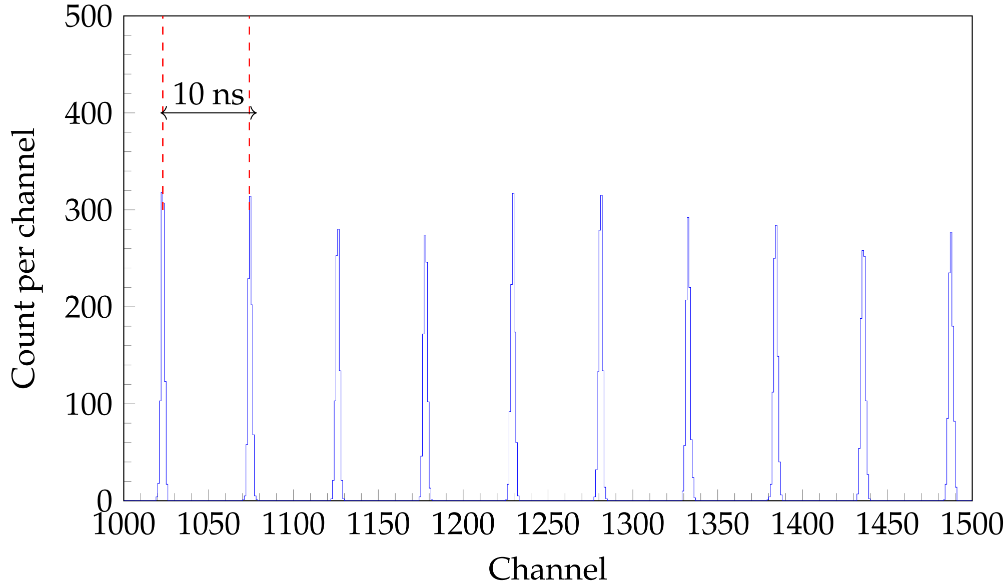


FIGURE 5.16: TDC calibration spectrum for one of the TDC channel. A time calibration module is used to generate peaks equidistantly. The interval between peaks is constant.

A TDC spectrum, which shows the correlation between one $\gamma$-ray channel and one particle channel, consist of a peak sitting on a flat background. The peak corresponds to the prompt events in which a $\gamma$ ray signal and the particle signal are a 'true' coincidence. The background is caused by the random coincidence of a decay $\gamma$ ray with a scattered particle or an $^{254}$Es de-excitation $\gamma$-ray with an elastically (not correlated) scattered particle.

The peak positions of different TDC channels are slightly different due to the different timing properties of the electronics (as shown in Figure 5.17(a), 5.18(a), 5.19(a)). The TDC spectrums were aligned to apply a common time windows for the event-selection process. The alignments are done by first choosing the TDC peak position of one detector/segment as a reference and, second, shifting other TDC spectrum to make their peak position aligned with the reference peak. Alignments are done for the group of coaxial HPGe, clover HPGe and $LaBr_3$(Ce) detectors (as shown in Figure 5.17(b), 5.18(b), 5.19(b)).

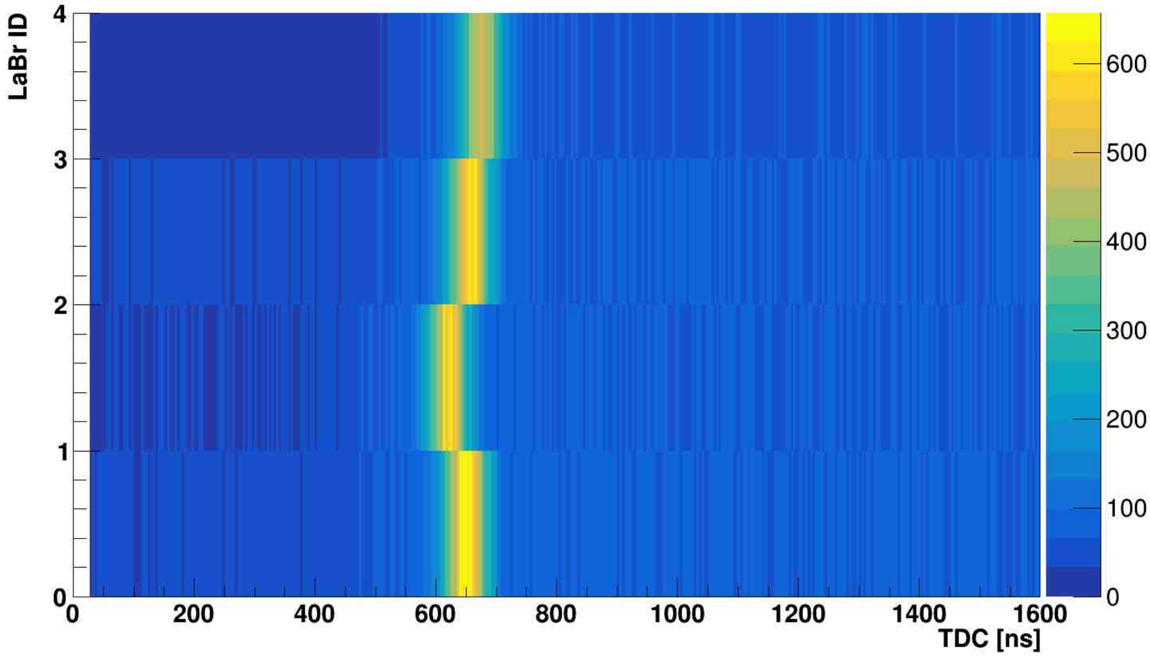


(a)

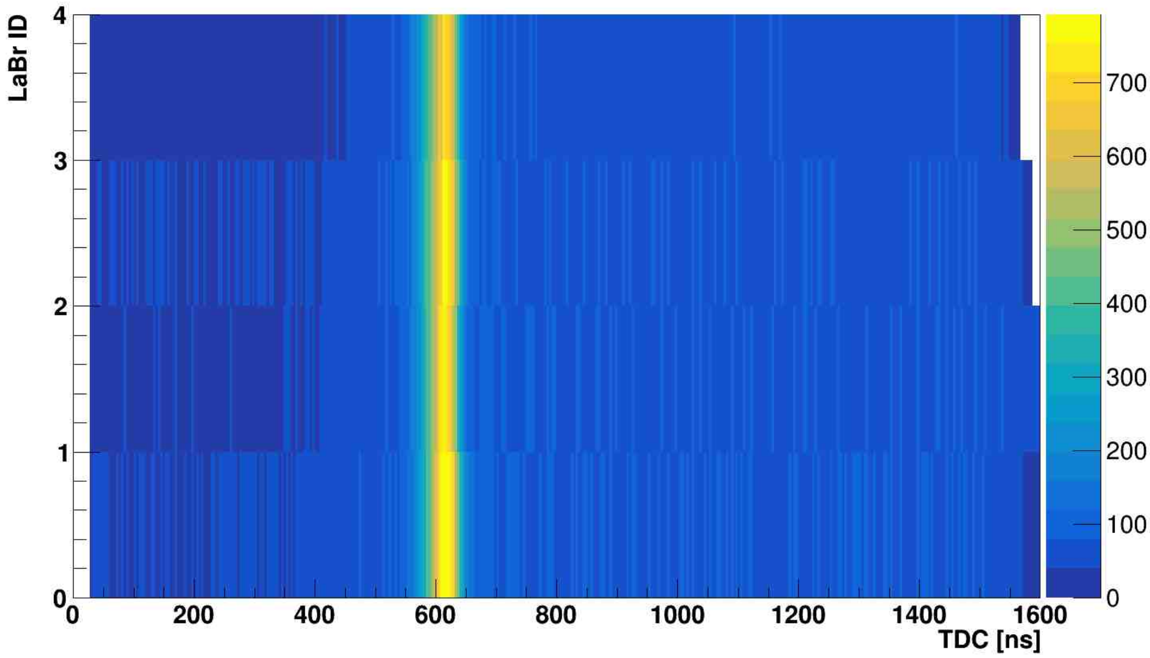


(b)

FIGURE 5.17: Plot of $LaBr_3(Ce)$ detectors TDC before (a) and after (b) alignment

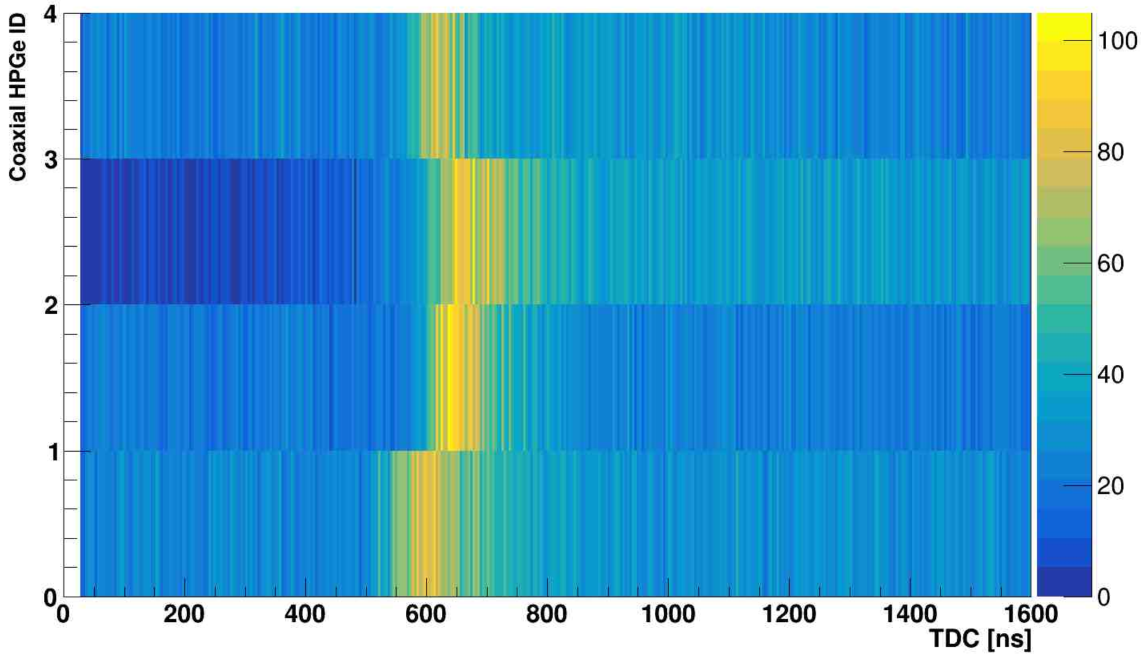


(a)

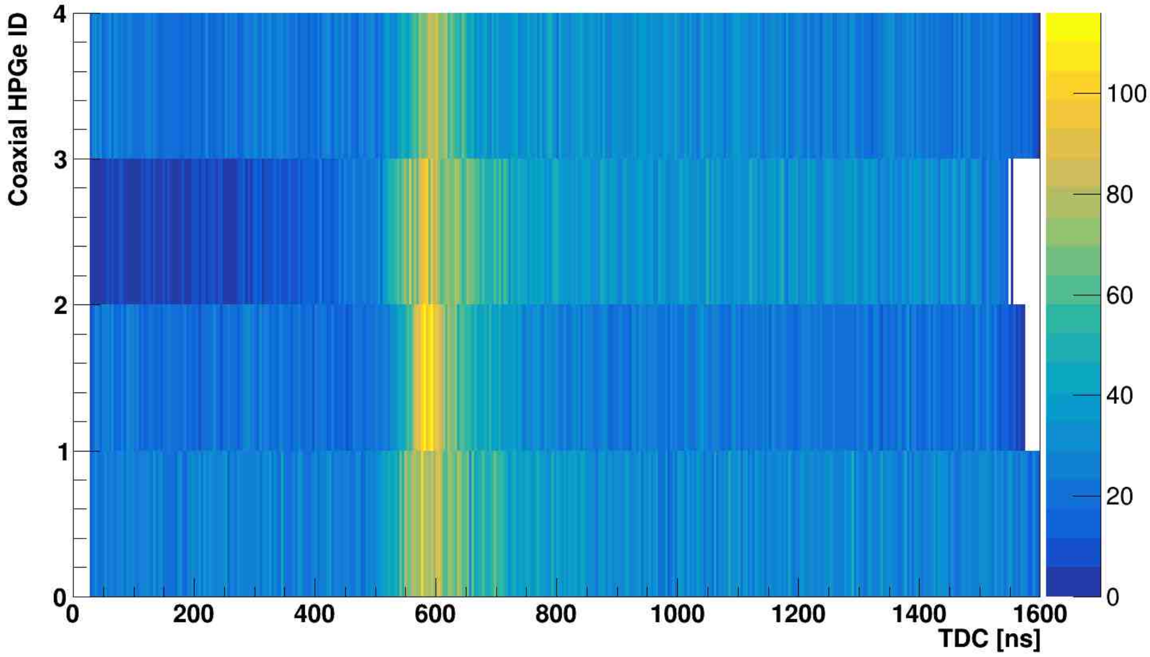


(b)

FIGURE 5.18: Plot of Coaxial HPGe detectors TDC before (a) and after (b) alignment

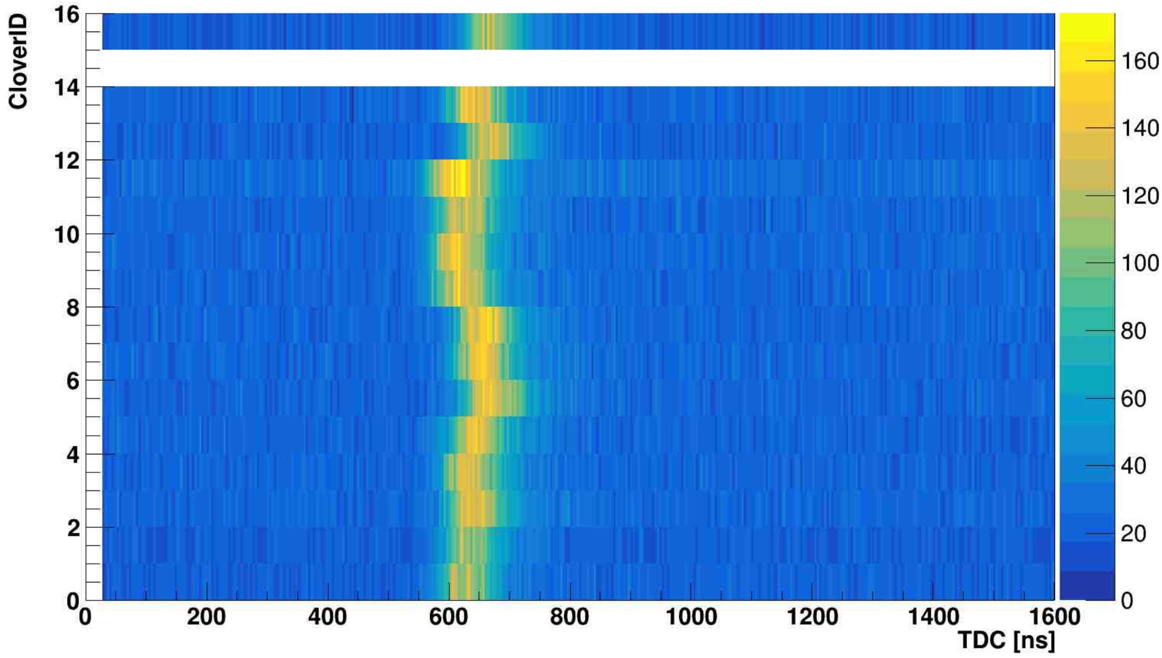


(a)

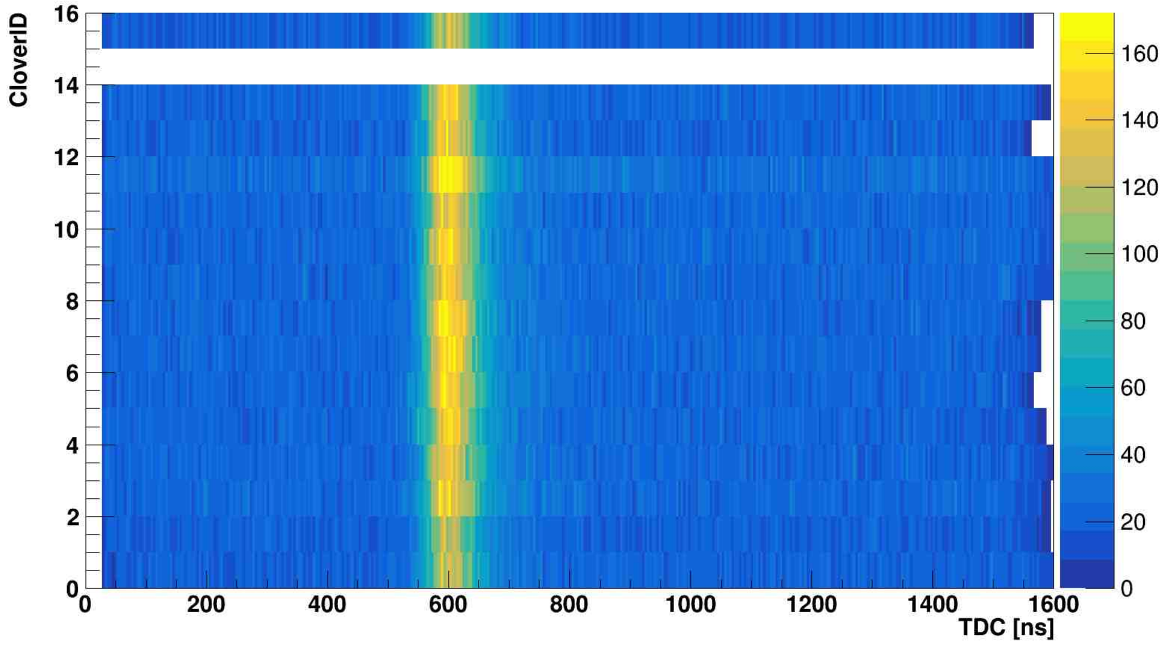


(b)

FIGURE 5.19: Plot of Clover HPGe detector TDC before (a) and after (b) alignment

## 5.2 Event selection

### 5.2.1 Time windows

The time difference between a $\gamma$-ray detector signal, and a particle detector signal, is used to determine whether they are correlated. The prompt and background window for each type of detector are determined as shown in Figure 5.20, 5.21, 5.22. The prompt and background time windows are set to the same width. The random events in the background time window are used to determine the background spectra, which are subtracted from the prompt coincidence spectra, assuming a constant background rate across the correlation time used.

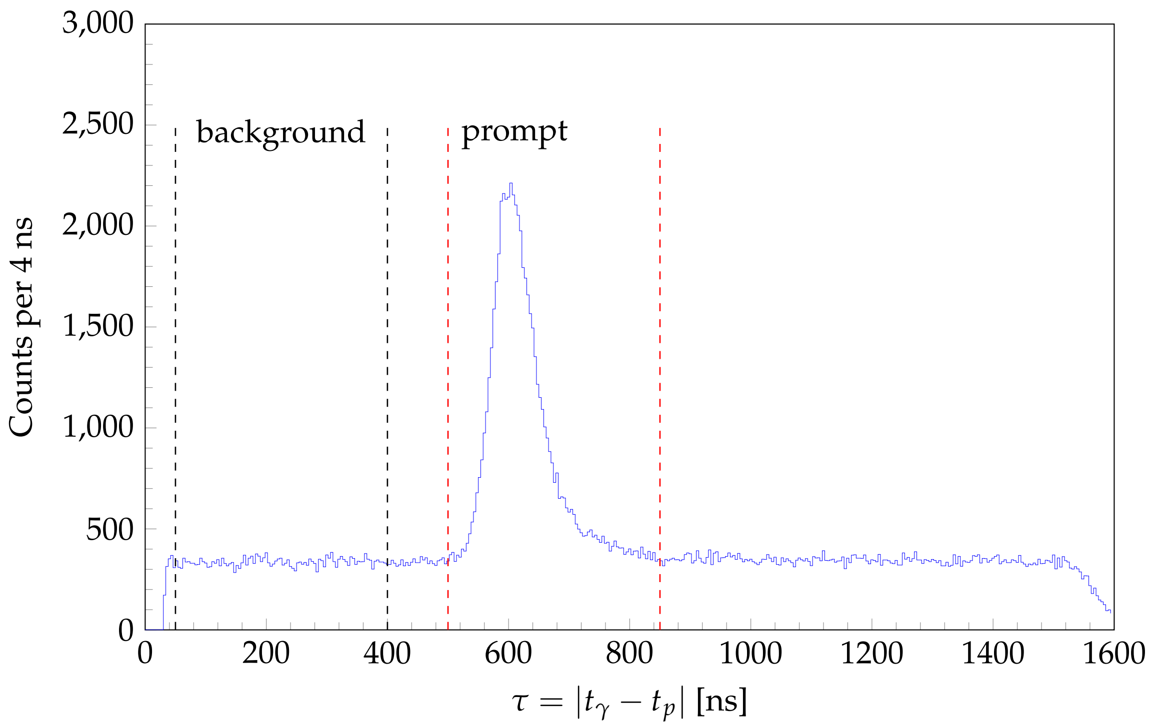


FIGURE 5.20: Particle-$\gamma$ time difference for Clover HPGe detectors. Time window selection for prompt (reaction) events and random background events are shown.

### 5.2.2 Particle identification

Besides the time gates on prompt $\gamma$-ray events, further gates need to be set on the silicon spectrum to select events in which $^{58}$Ni scattered on $^{254}$Es. In this binary inelastic reaction, the energy of the scattered $^{58}$Ni particles is fixed by binary kinematics

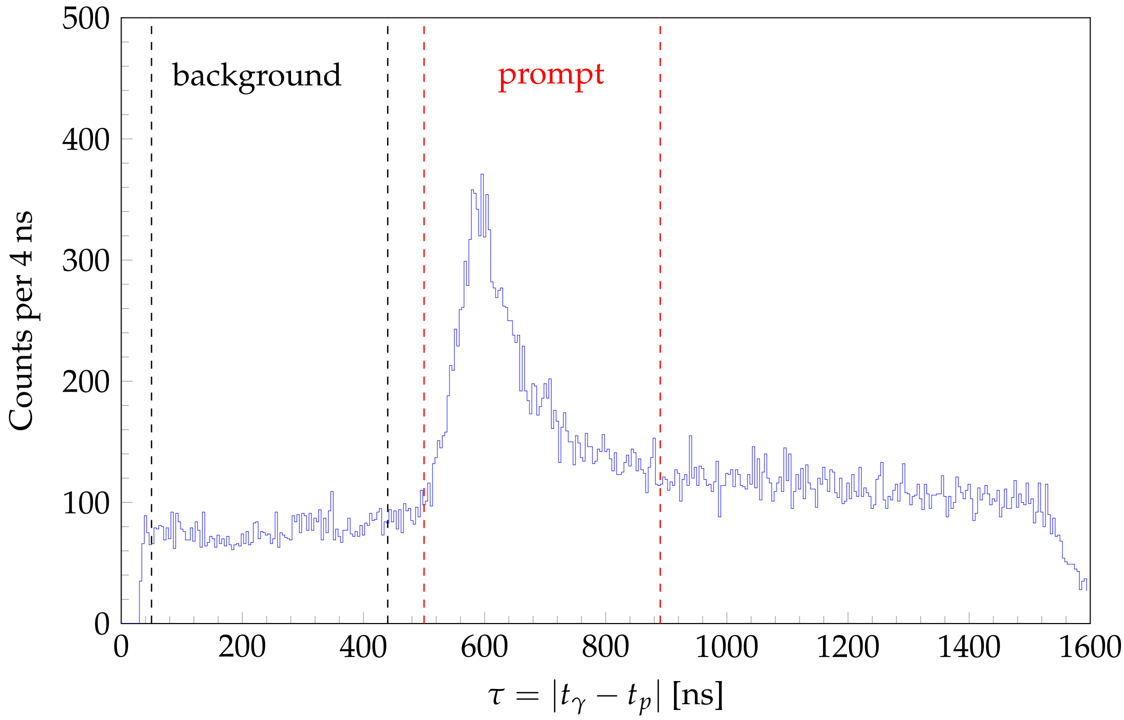


FIGURE 5.21: Particle-$\gamma$ time difference for coaxial HPGe detectors. Time window selection for prompt (reaction) events and random background events are shown.

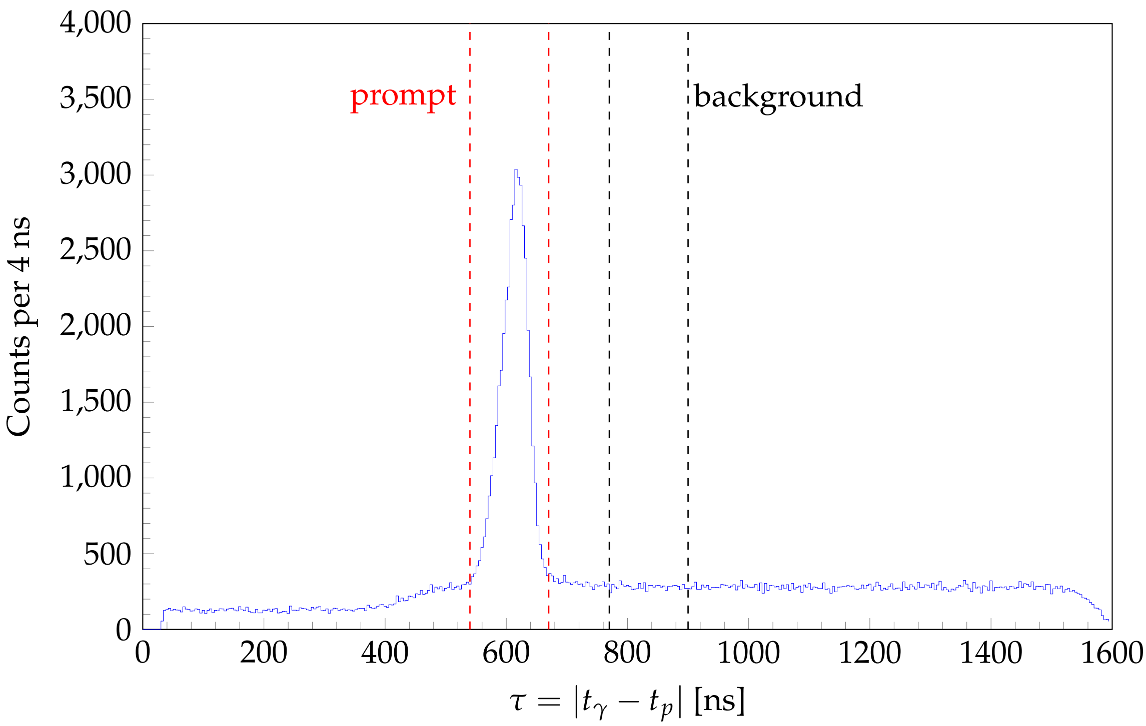


FIGURE 5.22: Particle-$\gamma$ time difference for $LaBr_3$(Ce) detectors. Time window selection for prompt (reaction) events and random background events are shown.

and depends on the scattering angle. However, due to the close geometry and high target radioactivity, the high rates of alpha particles lead to an unusual response of the

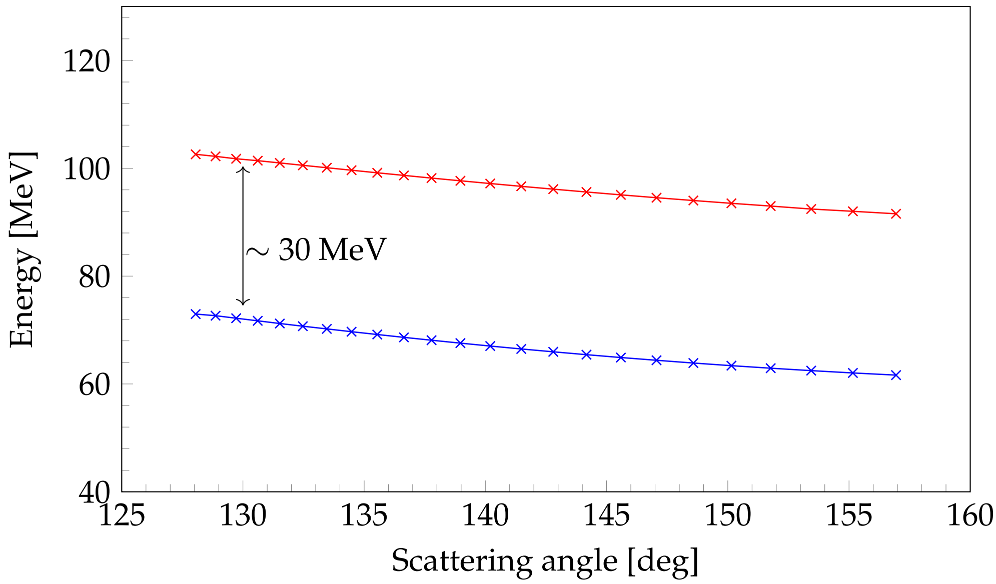


FIGURE 5.23: Kinetic energy of scattered projectiles 250 MeV $^{58}$Ni after hitting $^{254}$Es (red) and $^{nat}$W (blue) within the coverage angle of backward silicon detector. Points are energy values calculated at the angle correspond to the center of each channel. The energy values, including the lost as projectiles pass through the front backing, is calculated using LISE++ software [46].

Si detectors, with high leakage current, reduction of the depletion region, and poor energy resolution. During the experiment, a low-energy threshold was applied to the signal discriminators to exclude the alpha peaks from the target.

As the $\alpha$ peak is cut, the particle spectrum of the backward detector, supposedly, should contain only the event corresponding to $^{58}$Ni scattered on $^{254}$Es. However, it became apparent that trace amounts of tungsten were present in the target. The reason for the presence of tungsten is related to the production of the nickel backing foils between which the Es target is sandwiched. The backing foils were made in a standard evaporation chamber, where the nickel powder was placed in a small tungsten bowl. In previous experiments using actinide targets at the JAEA Tandem, the level of tungsten contamination in the foils was too small to be observed. However, the very small amount of $^{254}$Es which could be electro-deposited makes this tungsten contamination more evident. Therefore, the particle spectrum of the backward detector also includes events in which $^{58}$Ni was scattered on tungsten. Figure 5.23 shows uncalibrated pulse-height of the most inner ring of the backward particle detector. The small peaks on

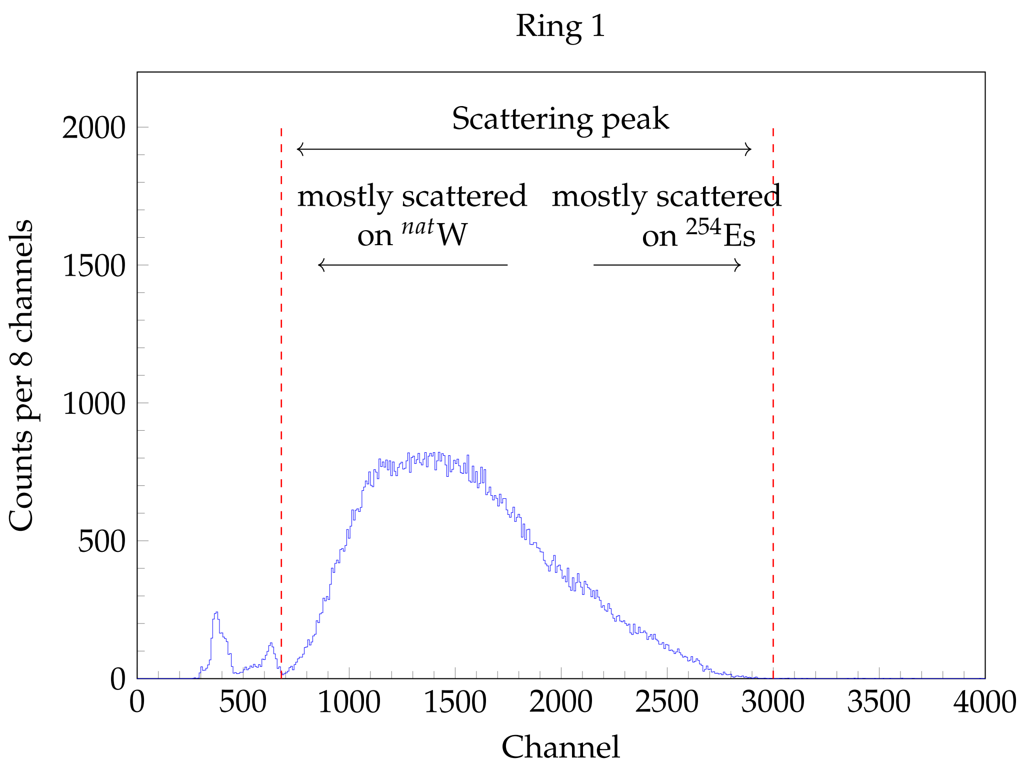
Ring 1
Scattering peak
mostly scattered on $^{nat}$W
mostly scattered on $^{254}$Es
Counts per 8 channels
Channel
0
500
1000
1500
2000
2500
3000
3500
4000

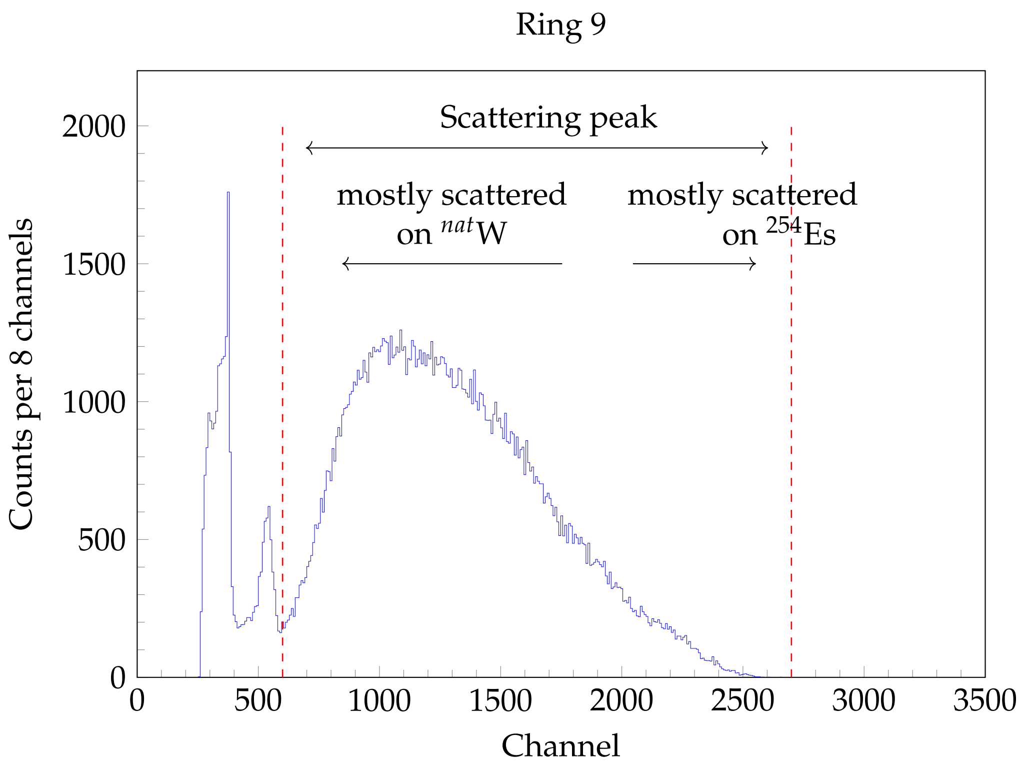
Ring 9
Scattering peak
mostly scattered on $^{nat}$W
mostly scattered on $^{254}$Es
Counts per 8 channels
Channel
0
500
1000
1500
2000
2500
3000
3500

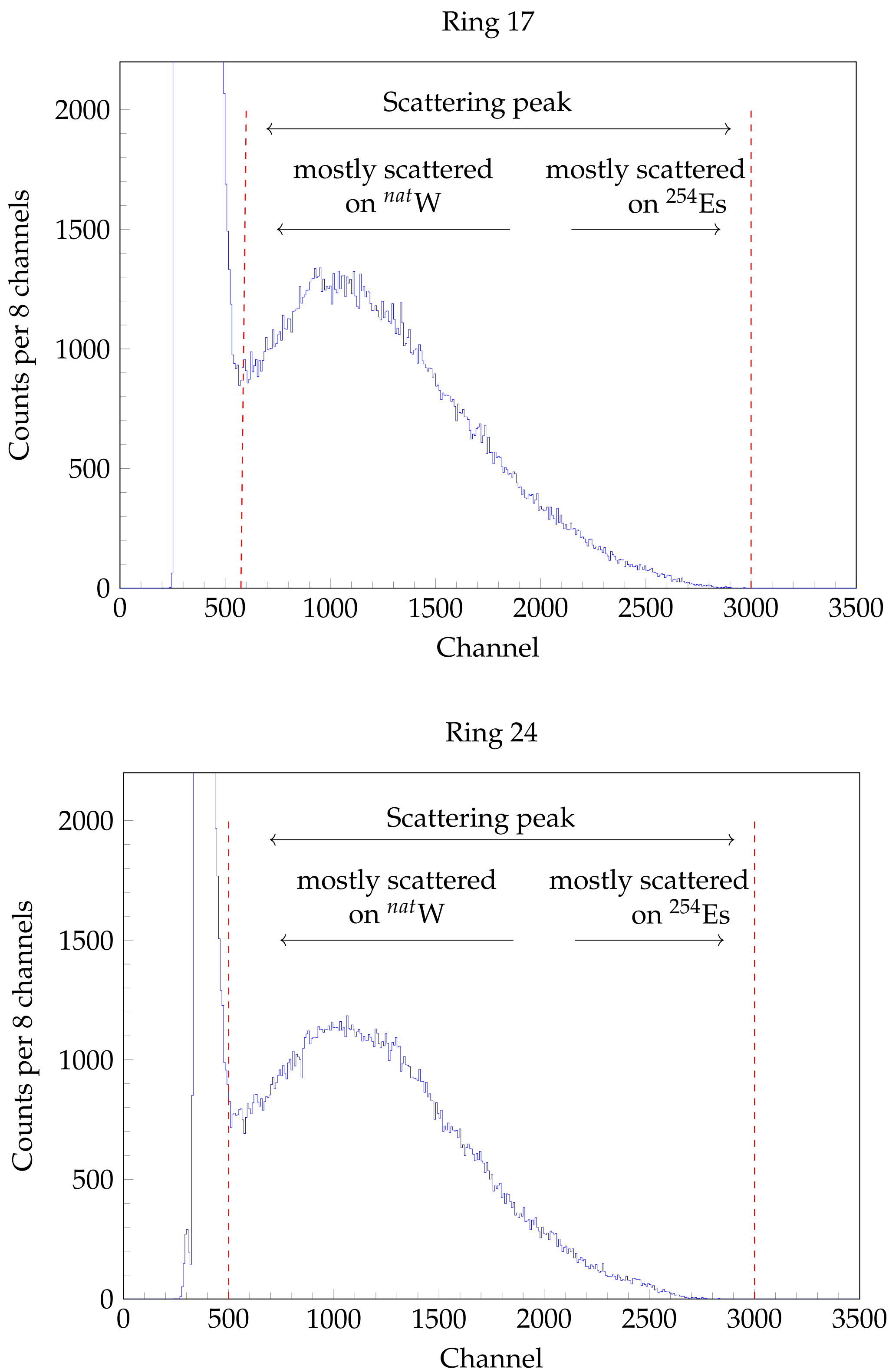


FIGURE 5.24: Spectrum of backward particle detector ring 1, 9, 17, 24 (at scattering angle 159.93°, 144.17°, 134.48°, 128.05° respectively). The threshold is set above $\alpha$-decay peak. The broad region between the red dashed lines corresponds to scattered nickel events. The peaks at the low energy region is the pile-up peak of $\alpha$ events. Because of its lower mass, particles scattered on W should be found at lower energies compared to particles scattered on Es, the Tungsten region is supposed to locate in the lower region of the scattering peak.

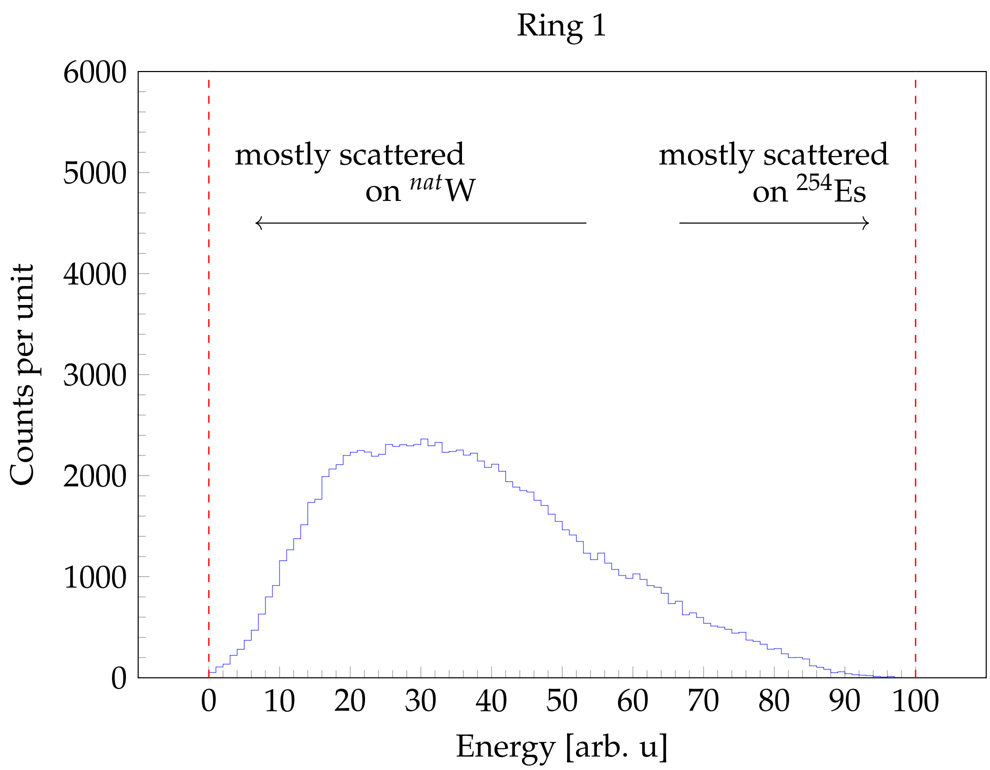
Ring 1
mostly scattered on $^{nat}$W
mostly scattered on $^{254}$Es
Counts per unit
6000
5000
4000
3000
2000
1000
0
0 10 20 30 40 50 60 70 80 90 100
Energy [arb. u]

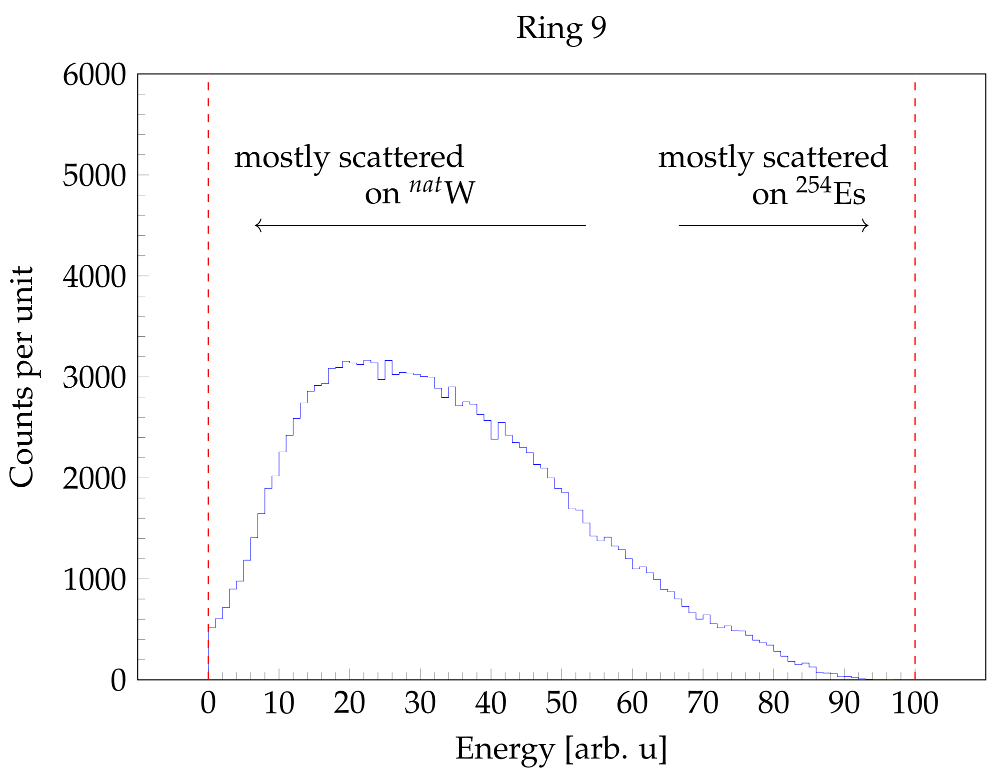
Ring 9
mostly scattered on $^{nat}$W
mostly scattered on $^{254}$Es
Counts per unit
6000
5000
4000
3000
2000
1000
0
0 10 20 30 40 50 60 70 80 90 100
Energy [arb. u]

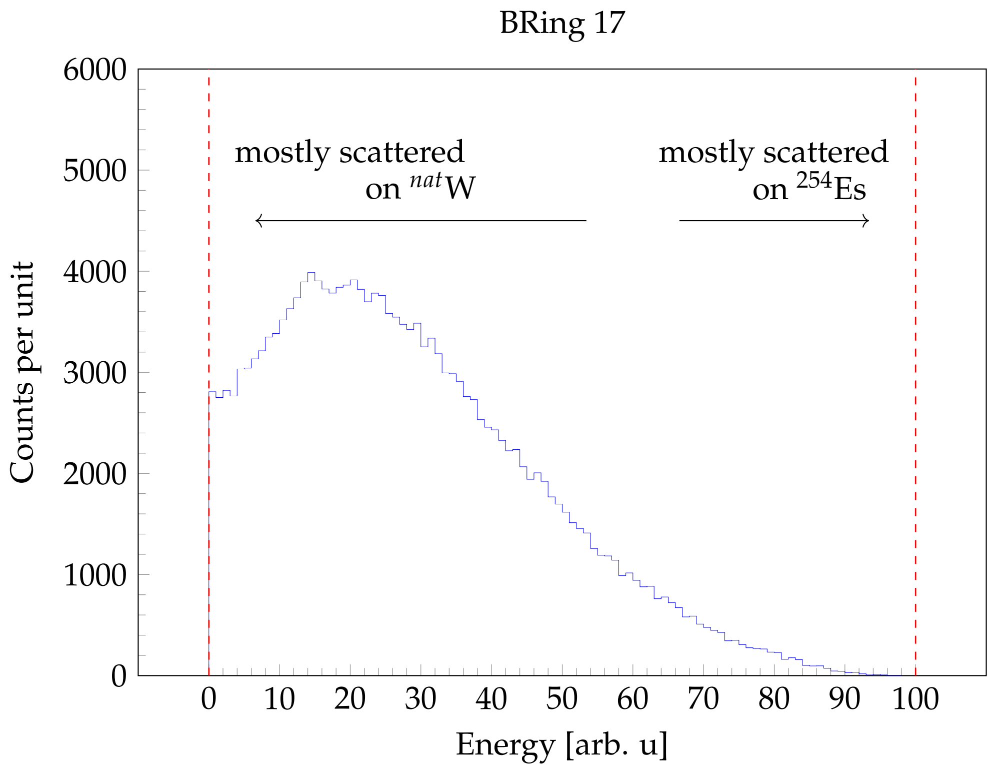


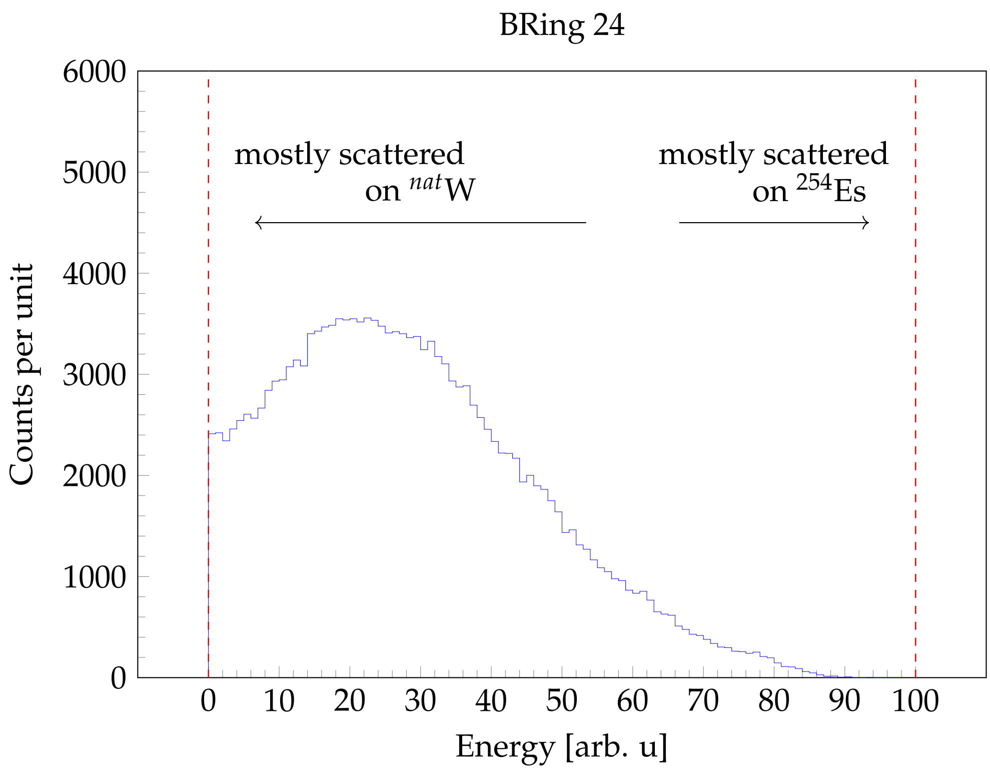


FIGURE 5.25: The normalized spectrum of backward particle detector channel 1, 9, 17, 24 (at scattering angle 159.93°, 144.17°, 134.48°, 128.05° respectively). The spectrum only shows the scattering peak. The range from lower to upper limit of the scattering peak is normalized to the scale 0 to 100.

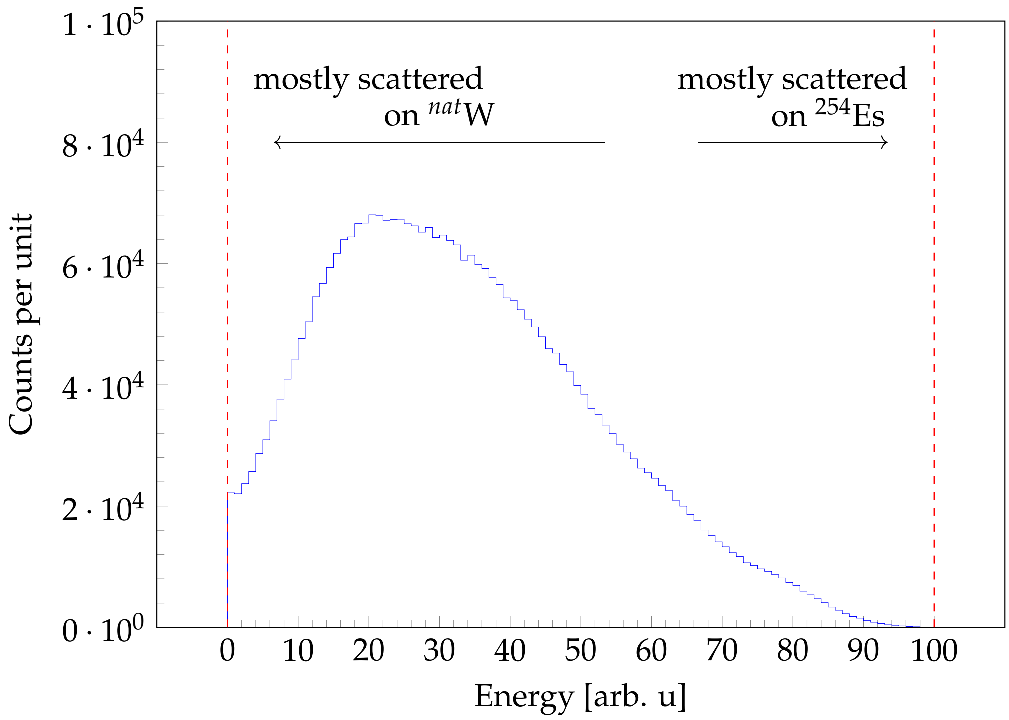


FIGURE 5.26: Spectrum of sum of all particle spectrum after normalized as 0 to 100 scale.The spectrum only shows the scattering peak. The range from lower to upper limit of the scattering peak is normalized to the scale 0 to 100.

the low-energy region correspond to the multiple pile-up signals induced by the $\alpha$ particle irradiation. Due to the poor resolution, it is not possible to clearly discriminate the peaks corresponding to $^{58}$Ni scattered on tungsten or on einsteinium. Rather than "peaks", in the following we will refer to tungsten and einsteinium "regions", to mean regions in the particle spectra where most of the detected events correspond to the detection of $^{58}$Ni scattered on W or Es. There are five naturally occurring isotopes of tungsten (Z=74), i.e., $^{180}$W (0.120%), $^{182}$W (26.50%), $^{183}$W(14.31%), $^{184}$W(30.64%) and $^{186}$W (28.43%). Because of the lower Z and mass number of tungsten compared to $^{254}$Es, reaction kinematics implies that nickel nuclei scattered on tungsten will be less energetic than those scattered on einsteinium. Therefore, one can expect that, to select the de-excited $\gamma$-ray from $^{254}$Es, gates should be set on the upper region of the silicon energy spectra. Due to the already mentioned poor energy resolution, the actual gates were chosen to minimize as much as possible the contaminant $^{nat}$W lines while at the same time keeping the $^{254}$Es peaks. These gates could not be set separately for each

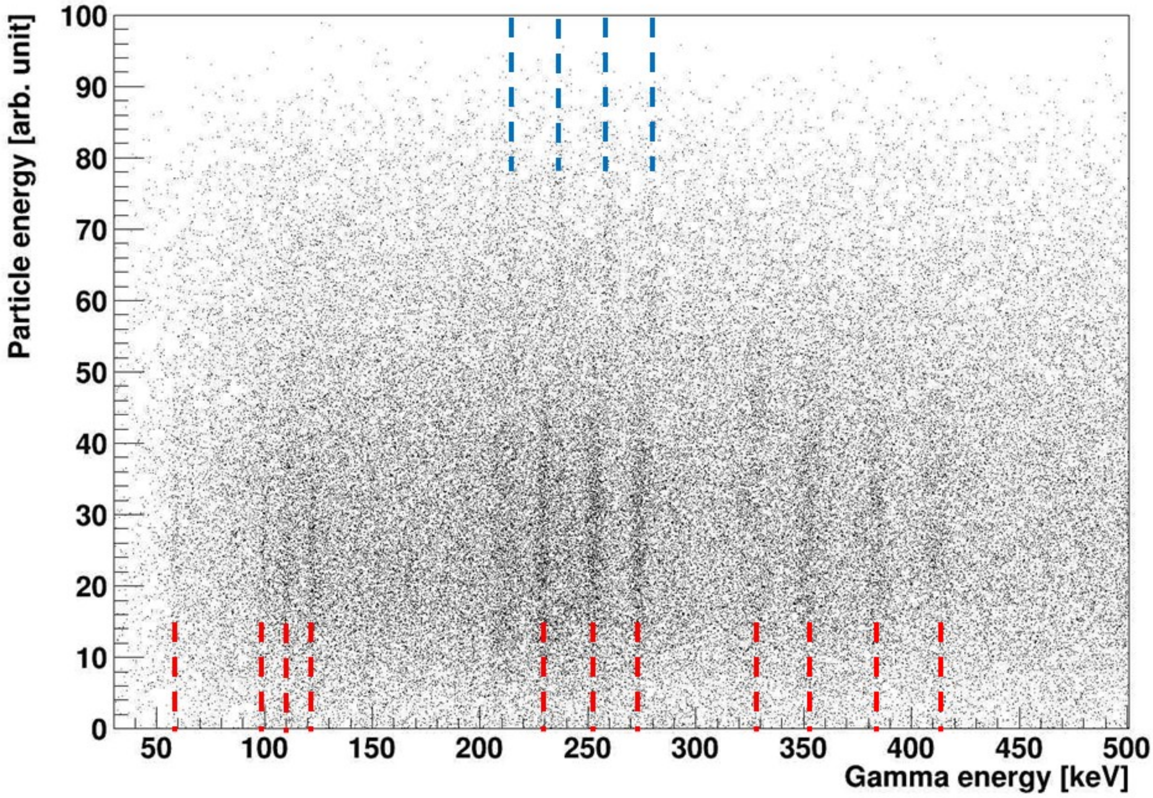


FIGURE 5.27: Plot of all particle energy (arbitrary unit) versus $\gamma$-ray energy from all coaxial HPGe detectors. The TDC-prompt gate and TDC-background gate subtraction are applied. The red, dashed lines represent the de-excited $\gamma$-ray of Tungsten isotopes are correlated with the lower particle energy region. The green dashed line correlate with the higher particle energy region are, exclusively, corresponding to the de-excitation $\gamma$-ray of $^{254}$Es.

individual strip due to the insufficient statistics. However, the non-observation of separate W and Es peaks did not permit to easily calibrate the energy spectrum of each strip. In order to add the Si data, a special treatment, described in the next paragraph, was applied to add the spectra.

Figure 5.26 shows the energy of $^{58}$Ni scattered on $^{nat}$W and $^{254}$Es in the angular range covered by the backward Si detector, calculated using LISE++ [46]. As it can be seen, the curves are separated by $\sim$30 MeV at all angles. It is also reasonable to assume that the energy resolution is roughly the same for all strips. Representative spectra corresponding to ring 1, 9, 17 and 24 are shown in Figure 5.24 For each strip, the region in the spectrum from the lowest channel above the radioactive alpha peak to the highest channel with counts was normalized to an arbitrary range from 0 to

TABLE 5.4: X-rays and $\gamma$-rays peaks in from the spectrum of coaxial HPGe detectors, gating on region [0 : 60] of normalized sum of all particle spectrum as shown in Figure 5.28. Assignment of these peaks and the corresponding energy values from references are also shown. The X-rays assignment is taken from [47]. The $\gamma$-rays assignment is taken from NSDF database [48, 49, 50, 51]. The $^{182}$W $2^+ \rightarrow 0^+$ and $^{183}$W $5/2^- \rightarrow 1/2^-$ transitions (B1-F1) are unresolvable.

| $\gamma$ peak | Energy [keV] | Assignment | Transition | Ref. Energy [keV] |
|---|---|---|---|---|
| A | 59.0(1) | W X-ray | $KL_1$ | 57.420(16) |
| | | | $KL_2$ | 57.98277(14) |
| | | | $KL_3$ | 59.318847(5) |
| B1-F1 | 99.5(1) | $^{182}$W g.s band | $2^+ \rightarrow 0^+$ | 100.10598(7) |
| B2 | 229.2(1) | | $4^+ \rightarrow 2^+$ | 229.3207(6) |
| B3 | 353.1(2) | | $6^+ \rightarrow 4^+$ | 351.02(6) |
| C1 | 110.5(1) | $^{184}$W g.s band | $2^+ \rightarrow 0^+$ | 111.2174(4) |
| C2 | 253.4(1) | | $4^+ \rightarrow 2^+$ | 252.845(10) |
| C3 | 383.2(2) | | $6^+ \rightarrow 4^+$ | 384.250(12) |
| D1 | 122.1(1) | $^{186}$W g.s band | $2^+ \rightarrow 0^+$ | 122.64(2) |
| D2 | 274.1(1) | | $4^+ \rightarrow 2^+$ | 273.93(5) |
| D3 | 411.0(2) | | $6^+ \rightarrow 4^+$ | 412.69(2) |
| B1-F1 | 99.5(1) | $^{183}$W 1/2[510] band | $5/2^- \rightarrow 1/2^-$ | 99.0793(17) |
| F2 | 209.2(2) | | $9/2^- \rightarrow 5/2^-$ | 209.879(12) |
| F3 | 327.6(2) | $^{183}$W 3/2[512] band | $11/2^- \rightarrow 7/2^-$ | 327.77(9) |

100. The normalized spectra for the same rings of Fig. 5.24 are presented in Fig. 5.25. Adding the normalized spectra should not increase the overlap between the W and Es regions.

Figure 5.26 shows the sum of all particle spectrum after this normalization. Figure 5.27 shows the plot of the normalized particle energy (adding all rings) versus the $\gamma$-ray energy detected in the coaxial HPGe detectors (placed at 90 degrees w.r.t. to the beam direction) with the TDC-prompt gate and TDC-background gate subtraction applied. The red dashed lines were drawn to highlight the tungsten gamma-ray lines observed only in the low-energy region. The green dashed lines highlight instead fainter $\gamma$ rays with different energies, observed only in the high region of the particle spectrum. As the following analysis will show, these gamma-rays come from the de-excitation of

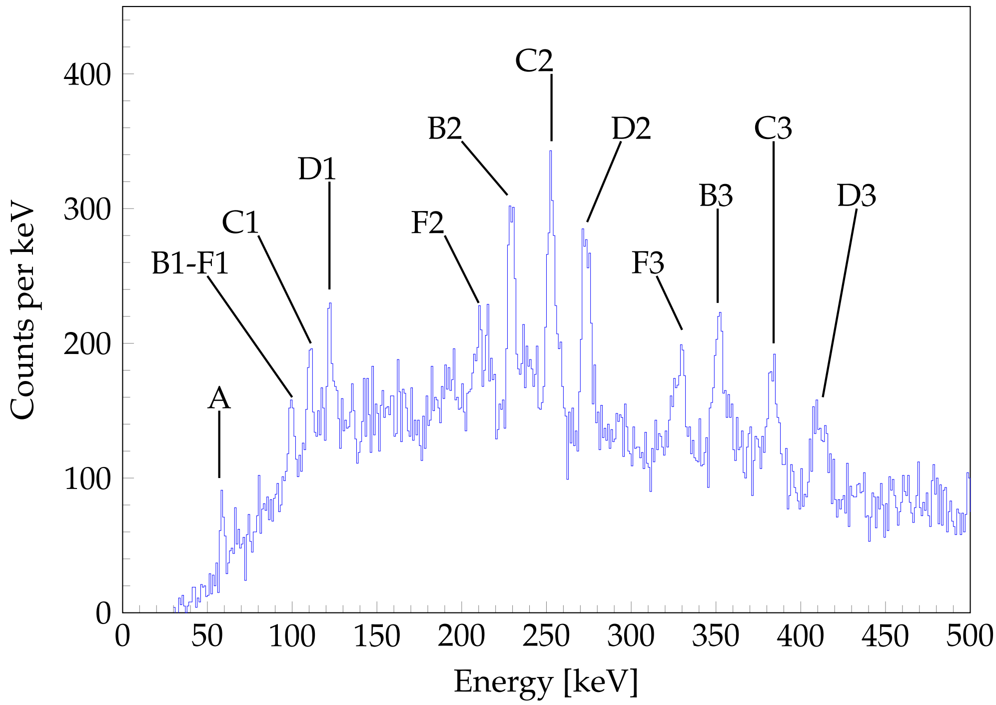


FIGURE 5.28: Spectrum of coaxial HPGe detectors, gating on the region [0 : 60] of sum of all normalized particle spectrum of the backward detector. The TDC-prompt gated is applied. Indexed peaks energy and their assignment are shown in Table 5.4.

$^{254}$Es.

The $\gamma$-ray peaks that appear in the 2-D matrix in Fig 5.27 are easier to see by looking at the projection on the $\gamma$-ray energy axis for different regions of the particle spectrum. Figure 5.28 shows the spectrum of coaxial HPGe detectors, gating on the region going from 0 to 60 in the normalized particle spectrum of all backward rings. Several tungsten peaks are visible, and they are listed in Table 5.4. The observation of X-rays and de-excitation $\gamma$-rays of different naturally occurring tungsten isotopes, confirms the tungsten contamination of the target backing foil and the particle identification of the lower region of silicon spectra.

Figure 5.29 shows the spectrum of coaxial HPGe detectors, gated on the region from 60 to 100 in the added normalized particle spectrum of the backward detector with the TDC-prompt gated applied. The energies of the observed peaks are clearly different from those of W isotopes, and the higher position in the silicon spectrum is evidence of a significantly larger A of the target nuclei, as expected for scattering on Es. The chemical separation of the Es from other actinide isotopes permits to exclude that any other actinide is present in large quantities in the target. This gating region, from 60 to 100 in the normalized particle spectrum, was chosen because it minimizes the contamination of W isotopes and maximizes the visibility of Es peaks in the spectrum. The same particle gate was also applied to obtain the prompt $\gamma$ ray spectra of Clover and $LaBr_3$(Ce) detectors. The analysis of these gated $\gamma$-ray spectra, and the steps taken to place new observed $\gamma$ transitions in the $^{254}$Es level scheme, are described in the next section.

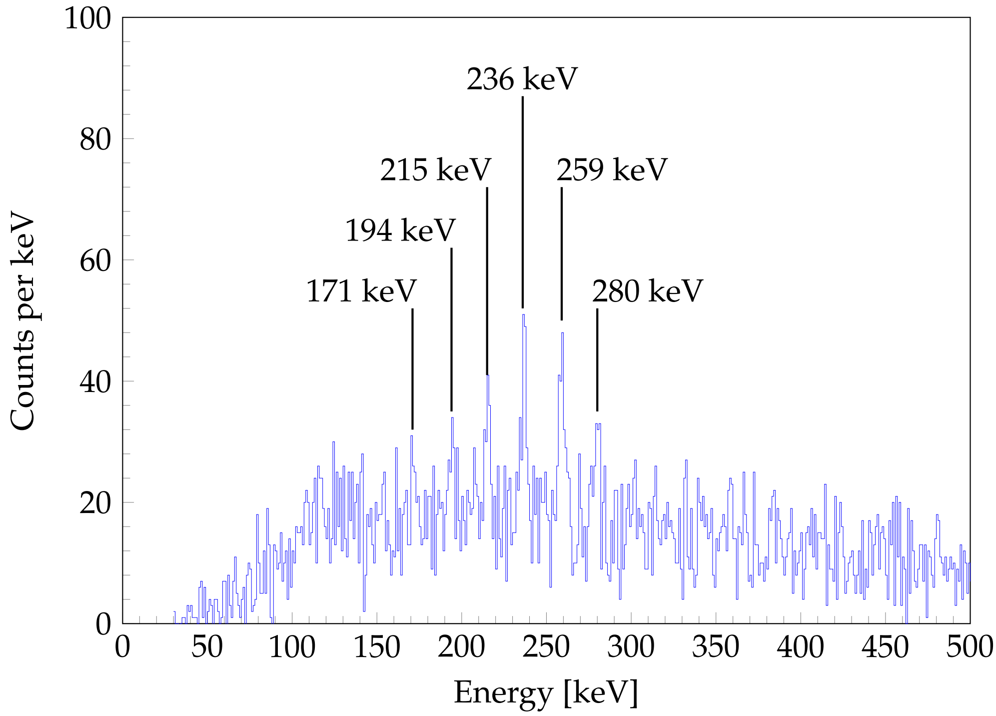


FIGURE 5.29: Spectrum of coaxial HPGe detectors, gating on the region [60 : 100] of sum of all normalized particle spectrum of the backward detector. The TDC-prompt gated is applied. The energy of $\gamma$-ray peaks is well-separated from Tungsten de-excitation $\gamma$-ray energy, indicating observation of the de-excitation $\gamma$-ray of $^{254}$Es.

## 5.3 Spectrum analysis

### 5.3.1 Doppler correction

The velocity of recoiling target nuclei are large enough to cause Doppler shift of the emitted photons. The energy of the detected $\gamma$-ray is shifted according to:

$$E' = E_0 \frac{\sqrt{1-\beta^2}}{1-\beta cos\alpha}, \tag{5.3}$$

where $E_0$ is the energy of the $\gamma$ ray emitted from the nucleus at rest, $\beta$ is the nucleus' velocity in units of c, and $\alpha$ is the angle between the emitted $\gamma$-ray and the radiating nucleus. Using the known position of the detector/segment which is "hit" by the $\gamma$ ray and the segment of the CD detector in which the particle deposits its energy, a correlation between particle angles ($\theta_p$ , $\phi_p$ ) and $\gamma$-ray angles ($\theta_\gamma$ , $\phi_\gamma$ ) can be made:

$$cos\alpha = sin\theta_p sin\theta_\gamma cos(\phi_p - \phi_\gamma) + cos\theta_p cos\theta_\gamma. \tag{5.4}$$

In principle, the direction of motion of the $^{254}$Es recoil can be determined from the direction of the detected scattered nickel. However, in this experiment only the ring signals were recorded, which implies that only the azimuthal angle but not the polar angle of the scattered nickel particles is known. For this reason, it is not possible to determine event-by-event $\theta_p$, and the averaged emission angle $\theta_p$=0 was assumed for all events. Hence, Eq. 5.4 becomes $cos\alpha = cos\theta_\gamma$.

The velocity of the recoil can be determined from the scattering angle of the ejectile, using conservation of momentum, in the assumption that the excitation energy is much smaller than the kinetic energy. The kinetic energy of the recoil $E_t^{lab}$ is can be calculated using the formulae:

$$\begin{aligned} \vartheta_T^{cm} &= \pi - sin^{-1}(\frac{m_P}{m_T} sin\theta_{lab}^P) + \theta_{lab}^P. \\ E_T^{Lab} &= \frac{2m_P m_T}{(m_P + m_T)^2}\,(1 + cos\vartheta_T^{cm})\,E_{beam}. \end{aligned} \tag{5.5}$$

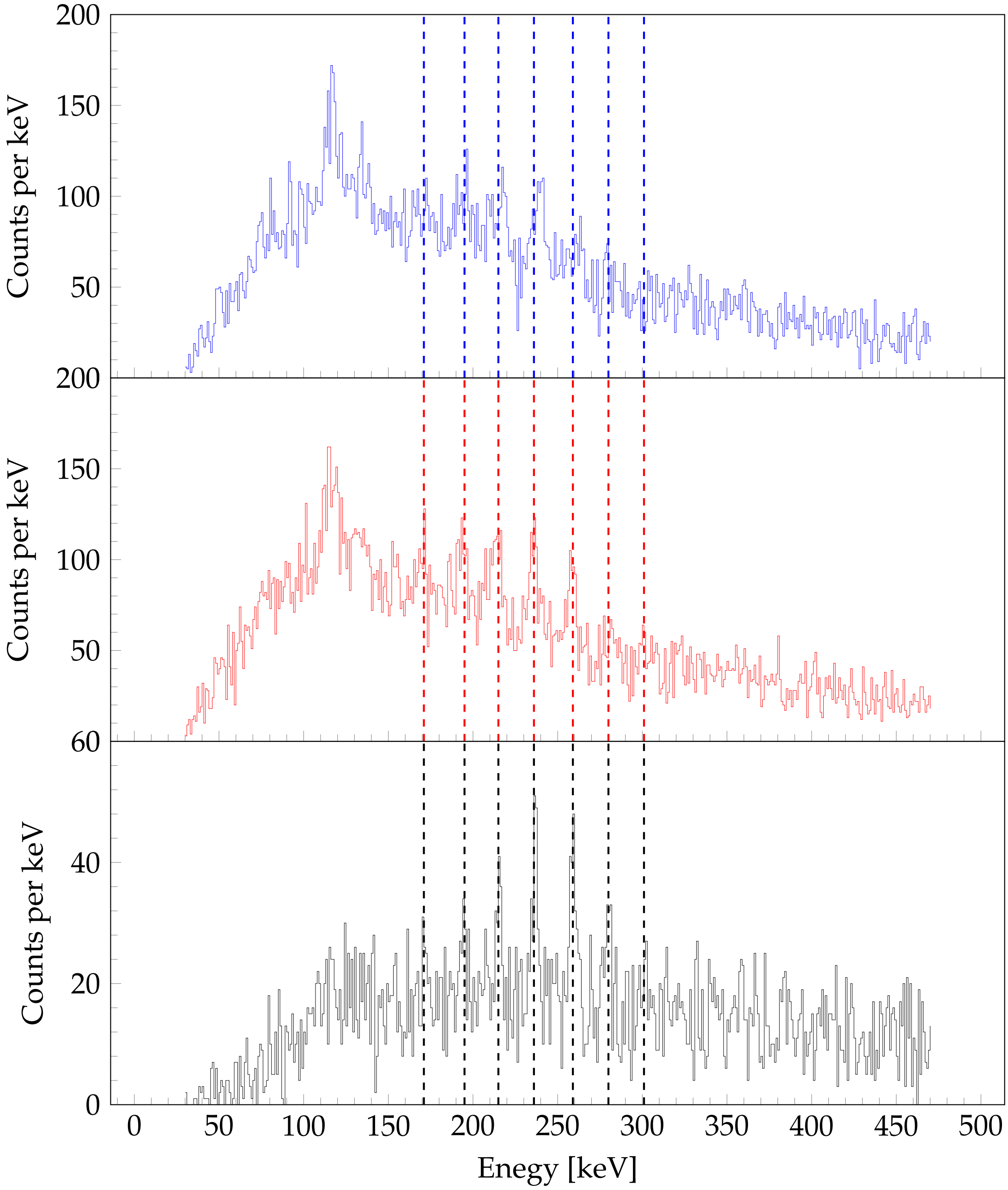


FIGURE 5.30: The $\gamma$-ray spectrum of Clover HPGe detectors after Doppler correction (red) in comparison with the one before Doppler correction (blue) and of coaxial HPGe detector (black). The Doppler correction corrected the energy of the $\gamma$ peaks and improved the peak's energy resolution.

where $m_P$ and $m_T$ are projectile and target mass respectively, $\vartheta_T^{cm}$ is the target recoil angle in the center-of-mass frame, $\theta_{lab}^P$ is projectile scattering angle in the laboratory frame and $E_{beam}$ is beam energy. Subsequently, $\beta$ is calculated using equation 5.6 where

$E_0$ is the rest-mass energy of the target nuclei:

$$\beta = \sqrt{\frac{E_T^{Lab}}{E_0}}. \tag{5.6}$$

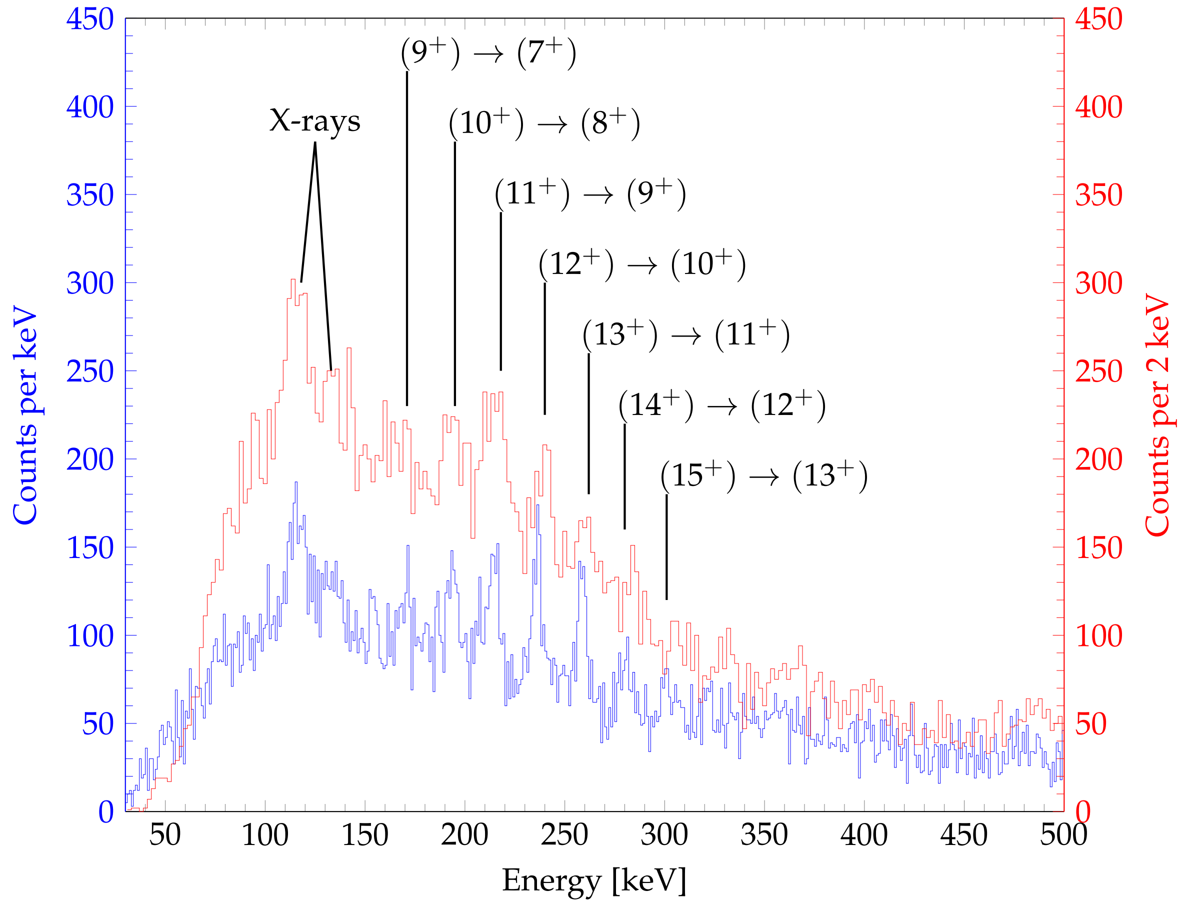


FIGURE 5.31: Background subtracted $\gamma$-ray spectrum of all HPGe detector (coaxial and Doppler correction Clover detectors) (blue) and $LaBr_3$(Ce) detectors (red).

The total spectrum of Clover HPGe detectors before and after Doppler correction are shown in Fig. 5.30. In the same figure, the uncorrected spectrum of coaxial HPGe detectors (which are not affected by the Doppler shift because they are placed at 90 degrees) can also be seen.

Like the coaxial Ge, the $LaBr_3$(Ce) scintillators were also placed at 90 degrees and do not need Doppler correction. Fig 5.31 shows the prompt, background subtracted and Doppler corrected spectrum of all HPGe detectors and the background subtracted spectrum of $LaBr_3$(Ce) scintillators. The $\gamma$-ray peaks were fitted with Gaussian shape

TABLE 5.5: $\gamma$-ray energy of transitions of ground-state rotational band and X-rays of $^{254}$Es. The energy value of X-rays and $(9^+) \rightarrow (7^+)$ is from $\alpha$-decay measurement [25]. The other transition energy values are from the extrapolation with associated initial and final spin (as shown in section 5.3.2). In comparison, the $\gamma$-ray energy value of observed transitions in coaxial HPGe detectors spectrum, Doppler-corrected Clover HPGe detectors spectrum and sum of all HPGe detectors spectrum. These values and associated errors are obtained from fitting the peaks with Gaussian shape. The X-ray peaks are unresolvable. Only limit of $K_\alpha$ peaks and limit of $K_\beta$ peaks in sum of all HPGe detector spectrum are shown.

| Transition | $E_\gamma$ (keV) | | | | |
|---|---|---|---|---|---|
| | Lit. value | Extrapolated using Eq. 5.9 | Coaxial HPGe detector | Clover HPGe detector | Sum of all HPGe detector |
| X-ray $K_\alpha$ | 112.4(2)<br>117.9(2) | | | | 111 - 119 |
| X-ray $K_\beta$ | 133.4(4)<br>136.8(3) | | | | 130 - 138 |
| $(9^+) \rightarrow (7^+)$ | 171.1 (2) | | 172.4 (5) | 169.6 (5) | 170.1 (6) |
| $(10^+) \rightarrow (8^+)$ | | 192.1 | 194.3 (4) | 193.6 (5) | 193.9 (4) |
| $(11^+) \rightarrow (9^+)$ | | 214.1 | 215.3 (3) | 214.4 (4) | 214.7 (3) |
| $(12^+) \rightarrow (10^+)$ | | 236.6 | 236.7 (2) | 236.0 (3) | 236.2 (2) |
| $(13^+) \rightarrow (11^+)$ | | 258.7 | 259.4 (3) | 258.0 (3) | 258.6 (2) |
| $(14^+) \rightarrow (12^+)$ | | 280.2 | 278.8 (4) | 282.0 (9) | 280.0 (7) |
| $(15^+) \rightarrow (13^+)$ | | 301.6 | 301.4 (7) | 302.4 (11) | 301.0 (7) |

and polynomial background using CERN ROOT framework [52]. The centroid of $\gamma$-ray peaks in different spectra are shown in Table 5.5. The efficiency-corrected intensity of $\gamma$-ray transitions are shown in Table 5.6. The assignment of these transitions will be presented in the next section.

### 5.3.2 Gamma peaks assignment and level scheme construction

#### Spin and parity of ground state

As introduced in Chapter 1, the $I^\pi$ of the ground-state of $^{254}$Es was assigned to be $(7^+)$ built on the coupling of one proton and one neutron in the Nilsson orbitals with the configuration $[p : 7/2[633] \otimes n : 7/2[613]]$. Only the lowest 3 states of the g.s. rotational band, i.e., up to spin $(9^+)$ were known prior to this experiment. The K quantum number of a rotational band can be guessed by comparing the level spacing between the band members, as shown by Eq. 5.7:

$$\frac{E_{K+1} - E_K}{E_{K+2} - E_{K+1}} \approx \frac{K+1}{K+2}. \tag{5.7}$$

This method is introduced by Yates et al. [53], which is derived from the general equation for the rotational energy [54].

The comparison can be quantized using the average $\chi^2_{average}$ as defined in equation 5.8:

$$\chi^2_{average} = \frac{1}{N}\sum_{i=1}^{N}\left(\frac{E_{K+i} - E_K}{E_{K+i+1} - E_{K+i}} - \frac{K+i}{K+i+1}\right)^2. \tag{5.8}$$

Figure 5.32 shows the $\chi^2_{average}$ values calculated using the energy of the first 3 states in the rotational band, using different guesses for the $K$ of the band. The $K$ which corresponds to the minimum $\chi^2_{average}$ is the most likely the "true" $K$ quantum number. In this case, $K$ = 6 or 7 yield the smallest $\chi^2_{average}$. The $K$ = 6 case can be excluded, since there is no available Nilsson orbit in the Fermi level near Z = 99 and N = 155 that can be coupled to spin 6 [26]. This is consistent with the previous tentative assignment of the ground state spin of $^{254}$Es. Once the K quantum number is determined, this comparison can also be used to determine whether a new transition belongs to the rotational band or not. In the next section, the assignment for the new observed transition will be introduced.

#### Assignment for newly observed transitions

As presented in section 2.2.1, the members of the ground-state rotational band of $^{254}$Es with K$^\pi$ = (7$^+$) will have I$^\pi$ = 8$^+$, 9$^+$, 10$^+$...

From Eq. 2.15, it follows that if one assumes a constant moment of inertia and small signature splitting, the rotational energy of each excited state can be related to its spin

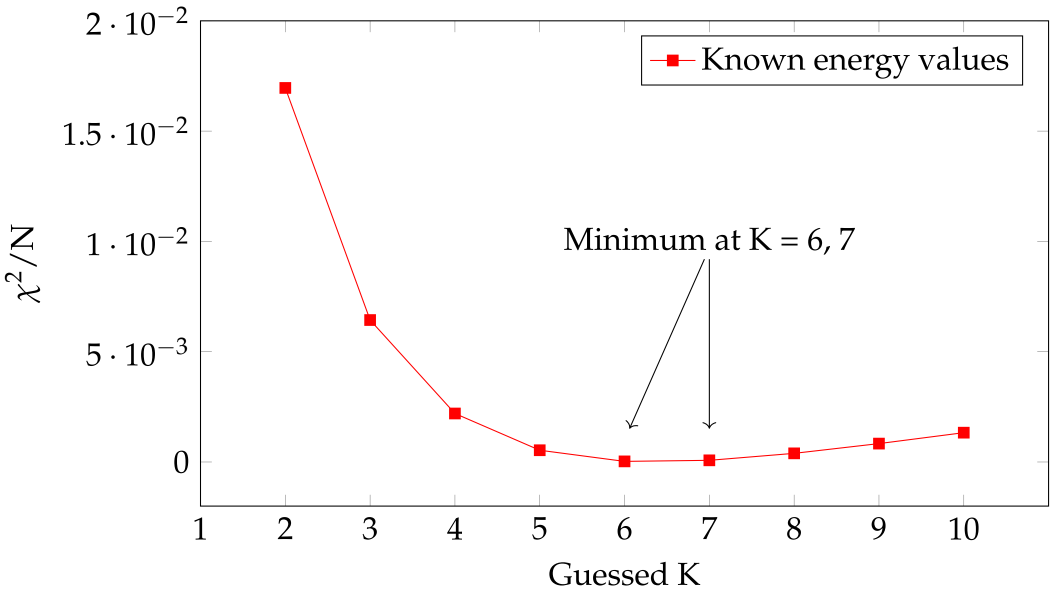


FIGURE 5.32: $\chi^2_{average}$ value of different guessed K values using previously known energy value of the ground-state rotational band of $^{254}$Es (up to ($9^+$)).

using the equation:

$$E_{rot}(I) = AI(I+1) + B. \tag{5.9}$$

This assumption is generally good for low and intermediate lying states and can be used to assign the spin value for newly found transitions [55].

The 3 known lowest excited states of the g.s. band in $^{254}$Es are enough to fit the A and B parameters, which are calculated to be A = 5.033 $\pm$ 0.015 and B = – 281.986 $\pm$ 1.048. Using these parameters, the rotational energy of the higher spin states can be extrapolated. The fit obtained from the known levels in $^{254}$Es is shown in Figure 5.33 where, using the extrapolated rotation energy, the transition energy values with $\Delta I = 2$ are calculated. The good match (less than 2% deviation) between the these calculated transition energies and the energy of the peaks observed in our experiment gives a strong indication that in this Coulomb-excitation experiment, the g.s. band of $^{254}$Es was populated up to spin (15+).

Another argument in support of our interpretation of the placement of the new $\gamma$ rays in the level scheme of $^{254}$Es is provided by the $\chi^2_{average}$ calculated using Eq. 5.8. Following the procedure described in Section 5.3.2, even when including all new

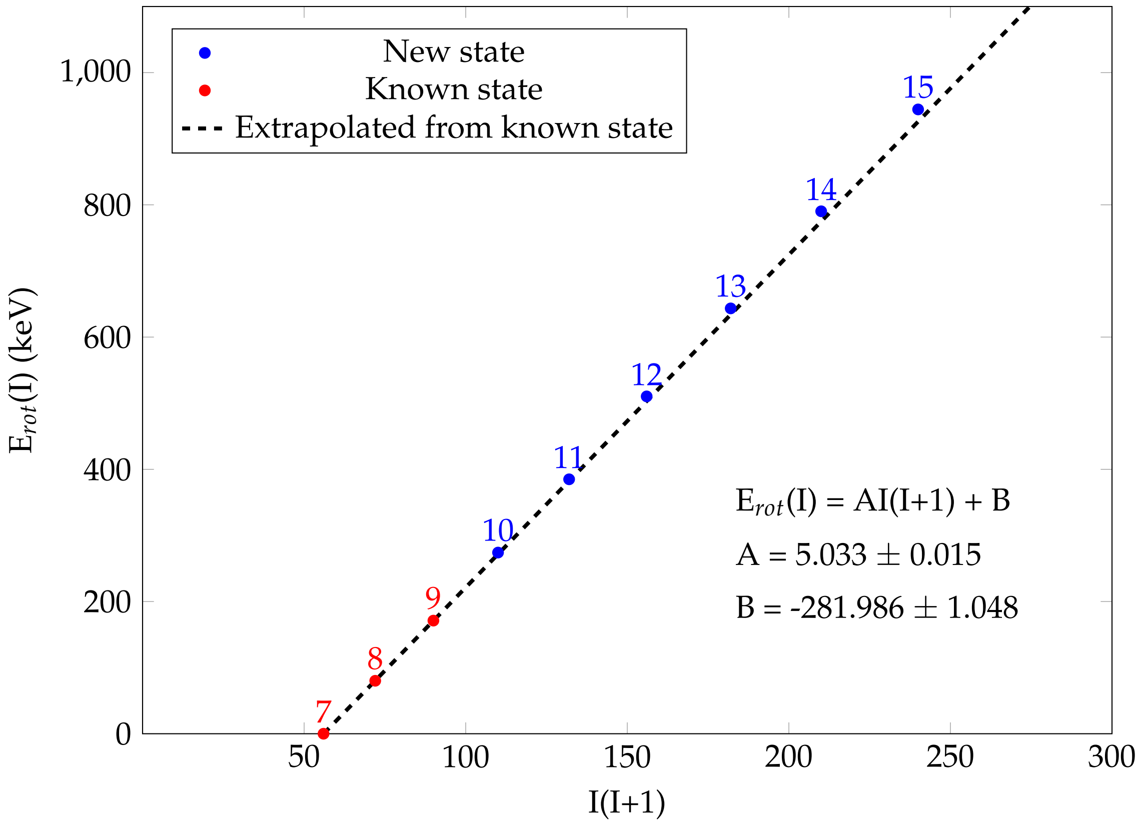


FIGURE 5.33: Rotational energy versus I(I+1). The already known states of the ground state rotational band [25] are shown in red. The dashed line corresponds to the fit obtained using these three states, The energies of the new states populated in this work is shown in blue. The good match between the extrapolation and the deduced states spin and energy strongly supports our assignments.

transitions, the minimum $\chi^2_{average}$ still found at K = 6 or 7. Therefore, it seems the most reasonable and safest assumption that the new observed transitions correspond to the higher-lying $\Delta I$=2 transitions in the g.s. rotational band.

A level scheme of ground-state rotational band is shown in Figure 5.35. The $\gamma$-ray energies and intensities were deduced by Gaussian fits of the peaks in the added spectrum of all HPGe detectors. The values are listed in Table 5.5 and 5.6. The energies of the excited states are determined from the energies of the $\gamma$-ray transitions. The transition with the highest intensity is ($12^+ \rightarrow 10^+$). The lower-lying transitions are less intense, most likely, due to the competition with the ΔI = 1 transitions. Unfortunately, these ΔI = 1 transition were not observed in our experiment. This is due to several reasons. The ($8^+ \rightarrow 7^+$) 80 keV, ($9^+ \rightarrow 8^+$) 90 keV and ($10^+ \rightarrow 9^+$) 104 keV transitions are in the low detection efficiency region of $\gamma$-ray detectors. Other ΔI = 1 transitions

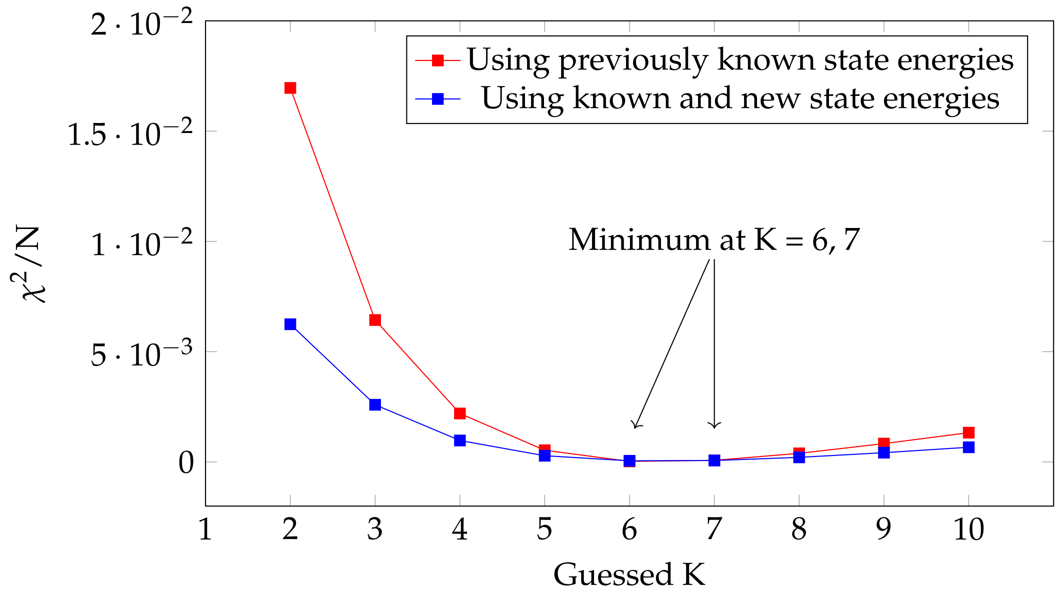


FIGURE 5.34: $\chi^2_{average}$ values of different guessed K values using previously known state energy value of the ground-state rotational band of $^{254}$Es (up to $(9^+)$); and using both known and new state energy deduced from $\gamma$ transitions found in this experiment (up to $(15^+)$).

TABLE 5.6: Efficiency-corrected $\gamma$-ray intensity of observed transitions in sum spectrum of all HPGe detectors and in $LaBr_3(Ce)$ detectors.

| Transition | Intensity | |
|---|---|---|
| | Sum of all HPGe detector | $LaBr_3(Ce)$ |
| $(9^+) \rightarrow (7^+)$ | $8962 \pm 1862$ | |
| $(10^+) \rightarrow (8^+)$ | $16859 \pm 1968$ | $15959 \pm 5091$ |
| $(11^+) \rightarrow (9^+)$ | $21378 \pm 2041$ | $18692 \pm 9226$ |
| $(12^+) \rightarrow (10^+)$ | $24949 \pm 2207$ | $20249 \pm 5678$ |
| $(13^+) \rightarrow (11^+)$ | $22184 \pm 2087$ | $17928 \pm 5941$ |
| $(14^+) \rightarrow (12^+)$ | $9069 \pm 1781$ | $14213 \pm 6452$ |
| $(15^+) \rightarrow (13^+)$ | $6933 \pm 1634$ | $10305 \pm 7732$ |

$(11^+ \rightarrow 10^+)$ 110 keV, $(12^+ \rightarrow 11^+)$ 126 keV and $(13^+ \rightarrow 14^+)$ 133 keV coincide with the X-rays. Also, the low energy value and the mixed E2/M1 multipolarity, result into the large electron conversion.

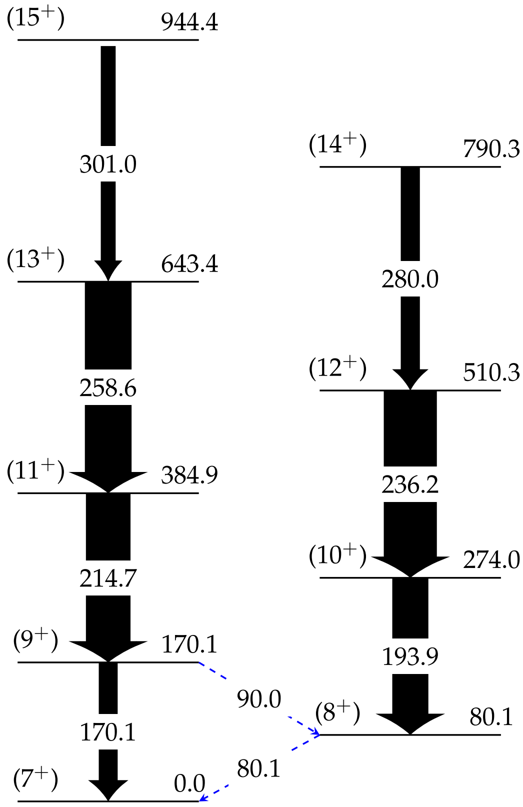


FIGURE 5.35: Level scheme of the ground-state rotational band of $^{254}$Es using newly assigned states and transitions. The transition energies were determined from the centroids of the peaks in the summed spectrum of all HPGe detectors (column 6, Table 5.5). The state energies were determined from the transition energies. The width of the arrows is proportional to the intensity of $\gamma$-ray transitions extracted from the spectrum of the sum of all HPGe detectors (as listed in Table 5.6). Note that low energy transitions proceed also in large part via electron conversion. The low $\gamma$-ray intensity of the lowest transitions is further discussed in Section 5.4.2 and in reference to the GOSIA-calculated intensities shown in Fig. 5.42.

## 5.4 GOSIA calculation

The spectroscopic data extracted in Section 5.3 were analyzed using the GOSIA code, previously described in Section 3.2. A simple schematic diagram of GOSIA calculation process is shown in Figure 5.36. The input required for GOSIA, including detectors geometry, level scheme, $\gamma$-ray yields along with other spectroscopic data, is summarized in Section 5.4.1. The minimization which is the procedure to fit the matrix elements to the data, and the methods used to ensure confidence in the final fit, are described in Section 5.4.2. Finally, the extraction of the error on the fitted matrix elements is described in Section 5.4.3.

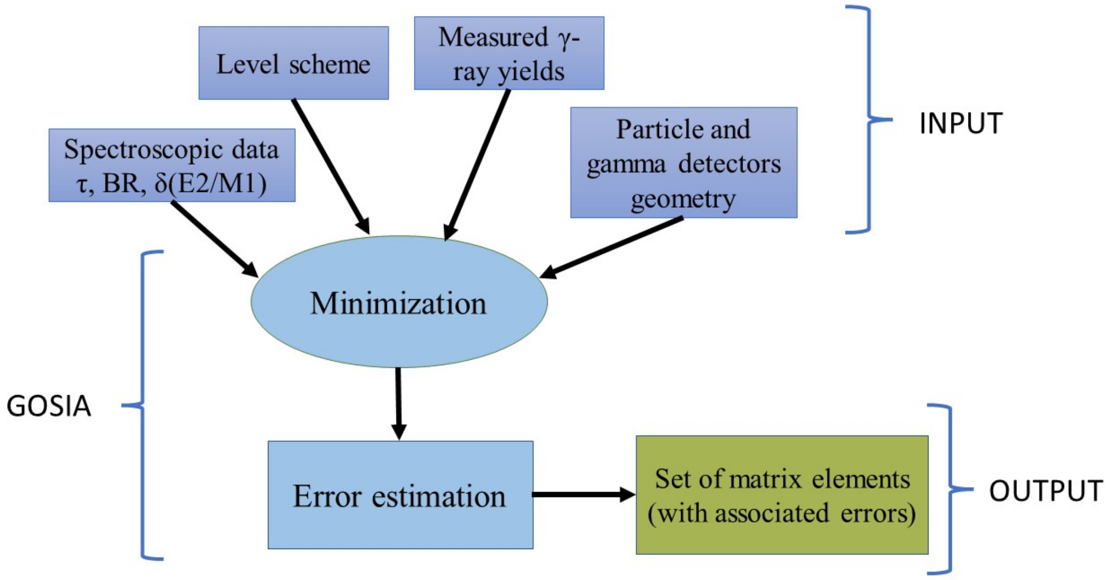


FIGURE 5.36: Schematic diagram of GOSIA calculation

### 5.4.1 Input preparation

#### Energy levels and transitions

For the GOSIA calculation, information on the beam and target species, along with beam energy and scattering angle, are required to determine the kinematics. Furthermore, the nuclear-structure information, energy levels and matrix elements, of the nucleus to be studied must also be defined. Since no excitation of the projectile nucleus was observed, information on the structure of the projectile nucleus is not required.

The $^{254}$Es energy levels (spin-parity and state energy) up to $I^{\pi} = (13^{+})$, which are established in section 5.3.2, are used for the GOSIA input. Although these are only seven levels, they correspond to 23 different transition matrix elements that need to be fitted. These matrix elements consist of five E2($\Delta$I = 2) transitions; six E2($\Delta$I = 1) transitions; six M1($\Delta$I = 1) transitions; and six E2 diagonal matrix elements. The initial values of these matrix elements to be fed as input to the non-linear multi-parameter fit, as well as the possible range that each value can assume, were tested across a wide range to ensure the robustness of the solution and the independence of the final result from the input values. The details of this procedure will be introduced in section 5.4.2.

#### Gamma-ray yields and spectroscopic data

The $\gamma$-ray yield was divided into two different groups of $\gamma$ detectors: $LaBr_3$(Ce) and HPGe (sum of spectrum from coaxial and Clover detectors). Each group consist of two different angular ranges for projectile scattering detection. In total, this input corresponds to four data sets, or ***"experiments"*** [2] as they are called in GOSIA. These sets are listed in Table 5.4.1. The angular range is defined using the detection angles in the laboratory and is assumed to be symmetrical in $\phi$ angle, hence the integration limits in the center-of-mass frame can be calculated by the code unambiguously.

For each experiment, the efficiency-corrected $\gamma$-ray yield, together with the associated uncertainty, for every observed transition is given in a separate file, read by the GOSIA code at run time. The uncertainties in the yields include not only the statistical errors, encapsulating the effect of subtracting background events and cleanliness of the fitted peak, but also a factor which represents the uncertainty on the relative efficiency of the $\gamma$-ray detectors.

Previously measured spectroscopic properties are included as further data points. From the literature, the 171 keV/91 keV relative branching ratio is 100(33)/26(16) and the mixing ratio E2/M1 of $(8^+) \rightarrow (7^+)$ (80.1 keV) transition is 1.25(25) [25, 28].

#### Particle and $\gamma$-ray detectors geometry

The geometry of $\gamma$-ray detectors array is one of the most the important input, as it is required for the treatment of the angular distribution, as described in section 3.2.2. The $\gamma$-ray detector geometry input includes the dimensions of each detector and its coordinates in the laboratory frame (distance from the target and $\theta$, $\phi$ angle to the beam direction, as shown in Table 4.1).

The details of the scattering angle of each ***experiment*** are required for the kinematic calculation and the $\gamma$-ray yield integration over the scattering angle range (as described

[2] The ***experiment*** notation stands for GOSIA's input data set will be set bold-titled to distinguish with conventional "experiment".

TABLE 5.7: Scattering angle range and detector cluster of ***experiment(s)*** expressed in Section 5.4.1; and $\gamma$-ray peak counts and efficiency corrected $\gamma$-ray yields for each observed transition in each ***experiment***.

| Experiment | Detectors | Scattering angle (lab) | Transition | $\gamma$-ray peak counts | Intensity |
|---|---|---|---|---|---|
| 1 | Coaxial HPGe(s) and Clover HPGe(s) | 142.98° - 157.83° | $(10^+) \rightarrow (8^+)$ | $180 \pm 21$ | $9094 \pm 1075$ |
| | | | $(11^+) \rightarrow (9^+)$ | $206 \pm 23$ | $10588 \pm 1196$ |
| | | | $(12^+) \rightarrow (10^+)$ | $235 \pm 32$ | $12380 \pm 1695$ |
| | | | $(13^+) \rightarrow (11^+)$ | $204 \pm 22$ | $11079 \pm 1202$ |
| 2 | $LaBr_3(Ce)$ scintillator | 142.98° - 157.83° | $(10^+) \rightarrow (8^+)$ | $83 \pm 45$ | $2874 \pm 1560$ |
| | | | $(11^+) \rightarrow (9^+)$ | $200 \pm 57$ | $7129 \pm 2034$ |
| | | | $(12^+) \rightarrow (10^+)$ | $186 \pm 64$ | $6820 \pm 2348$ |
| | | | $(13^+) \rightarrow (11^+)$ | $124 \pm 51$ | $4680 \pm 1926$ |
| 3 | Coaxial HPGe(s) and Clover HPGe(s) | 131.99° - 140.83° | $(9^+) \rightarrow (7^+)$ | $100 \pm 19$ | $5025 \pm 960$ |
| | | | $(10^+) \rightarrow (8^+)$ | $161 \pm 26$ | $8134 \pm 1323$ |
| | | | $(11^+) \rightarrow (9^+)$ | $179 \pm 21$ | $9210 \pm 1091$ |
| | | | $(12^+) \rightarrow (10^+)$ | $169 \pm 21$ | $8903 \pm 1114$ |
| | | | $(13^+) \rightarrow (11^+)$ | $156 \pm 18$ | $8472 \pm 983$ |
| 4 | $LaBr_3(Ce)$ scintillator | 131.99° - 140.83° | $(10^+) \rightarrow (8^+)$ | $106 \pm 43$ | $3670 \pm 1491$ |
| | | | $(11^+) \rightarrow (9^+)$ | $234 \pm 103$ | $8340 \pm 3673$ |
| | | | $(12^+) \rightarrow (10^+)$ | $223 \pm 74$ | $8177 \pm 2715$ |
| | | | $(13^+) \rightarrow (11^+)$ | $152 \pm 67$ | $5737 \pm 2530$ |

in section 3.2.3). The scattering angles are calculated from the size of the particle detector and its distance to the target (as shown in section 4.3.2) and are shown in Table 5.7.

### 5.4.2 Fitting procedure

The minimization involved a total of 17 experimental yields for eleven different E2($\Delta$I = 2) transitions over four ***experiments*** (tabulated in Table 5.7) plus the 2 additional spectroscopic data. Unfortunately, the experimental yields for the $\Delta$ I = 1 transitions are not included, as they cannot be observed in the spectrums with sufficient statistic. A total of 23 matrix elements are varied in the fit. The initial values of the E2 matrix elements (transitional and diagonal) are estimated from an assumed quadrupole deformation using the rigid-rotor model (using equations 2.25 and 2.21). The matrix element of $\langle 7||M1||8\rangle$ is estimated from the estimated $\langle 7||E2||8\rangle$ matrix element and the mixing ratio of the $(8^+) \rightarrow (7^+)$ transition.

As the ΔI = 1 transition yields cannot be included and there is no estimation for the M1 matrix elements, a procedure is performed to ensure that the fit converges. First, only the E2 matrix elements (transitional and diagonal) are included. At this stage, the M1 matrix elements are ignored. The GOSIA fit result with this setup will give the initial values of such matrix elements for the next step. In the second step, the E2 matrix elements (transitional and diagonal) are fixed to the results value from the first step and matrix elements for M1(ΔI = 1) transitions are included. The results of E2 matrix elements in the first step and the M1 matrix elements in the second step are used as input for the third step. In the third step, all matrix elements are freed. The results of the third step are used to run the error estimation procedure to achieve the final results.

**Independence of the fit**

Using initial values estimated from the rigid-rotor model and an assumed quadrupole deformation is a "model dependent" approach and can lead to a misleading result. It is crucial to ensure that the final fit is independent to the initial parameters. To do this, several tests are performed using initial values estimated from different values of the assumed deformation.

The fits were tested using the assumed deformation in a range $\beta_2 = 0.21 - 0.36$ as the deformation of neighboring isotopes is around $\beta_2 = 0.3$. The limits of E2 matrix elements are set in a wide range of $\pm$ 100% of the initial value. The M1 matrix elements are set to be varied within $\pm 10$ $\mu_N$. The limit of the E2 matrix elements in the error estimation step are set to be $\pm$ 70% of the initial value; and $\pm 10$ $\mu_N$ for the M1 matrix elements. The results of matrix elements and the associated errors from different tests of assumed deformation are shown in Figures 5.37, 5.38, 5.39 and 5.39. These different

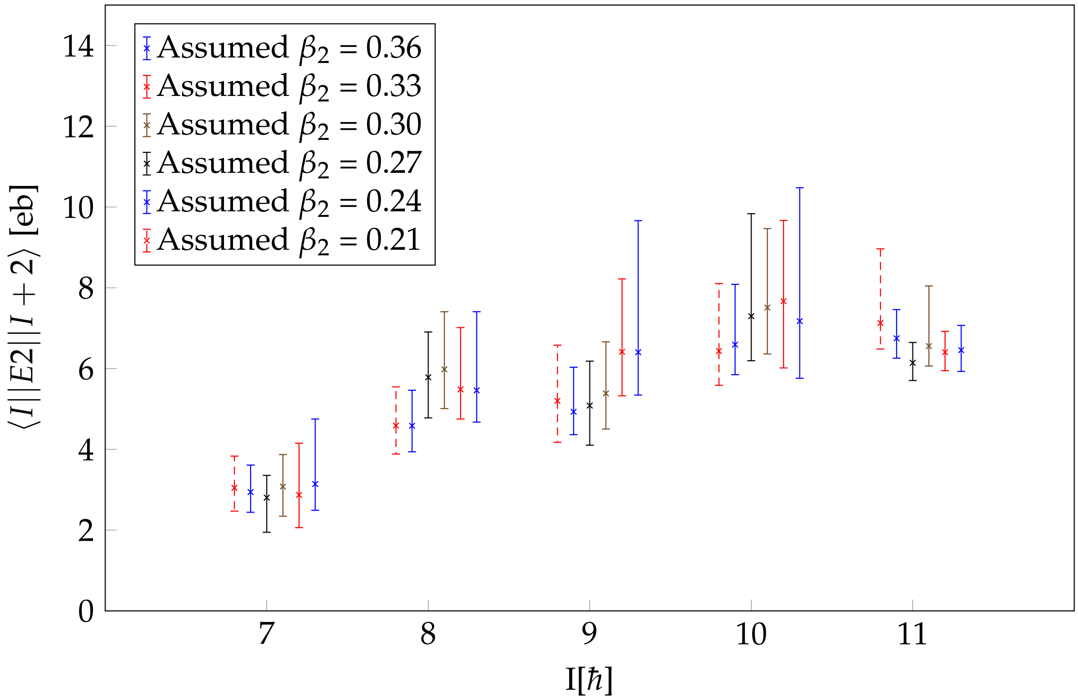


FIGURE 5.37: Magnitude of E2(ΔI = 2) matrix elements extracted from GOSIA with initial parameters which are estimated from different assumed deformation.

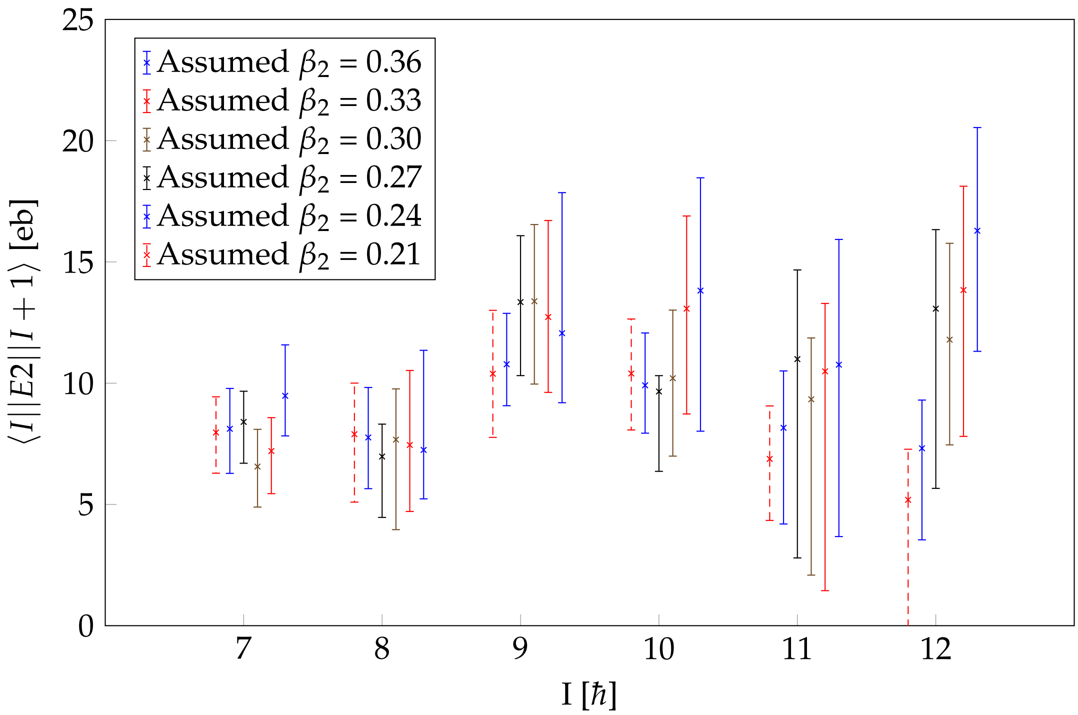


FIGURE 5.38: Similar to Figure 5.37 but for E2(ΔI = 1) matrix elements.

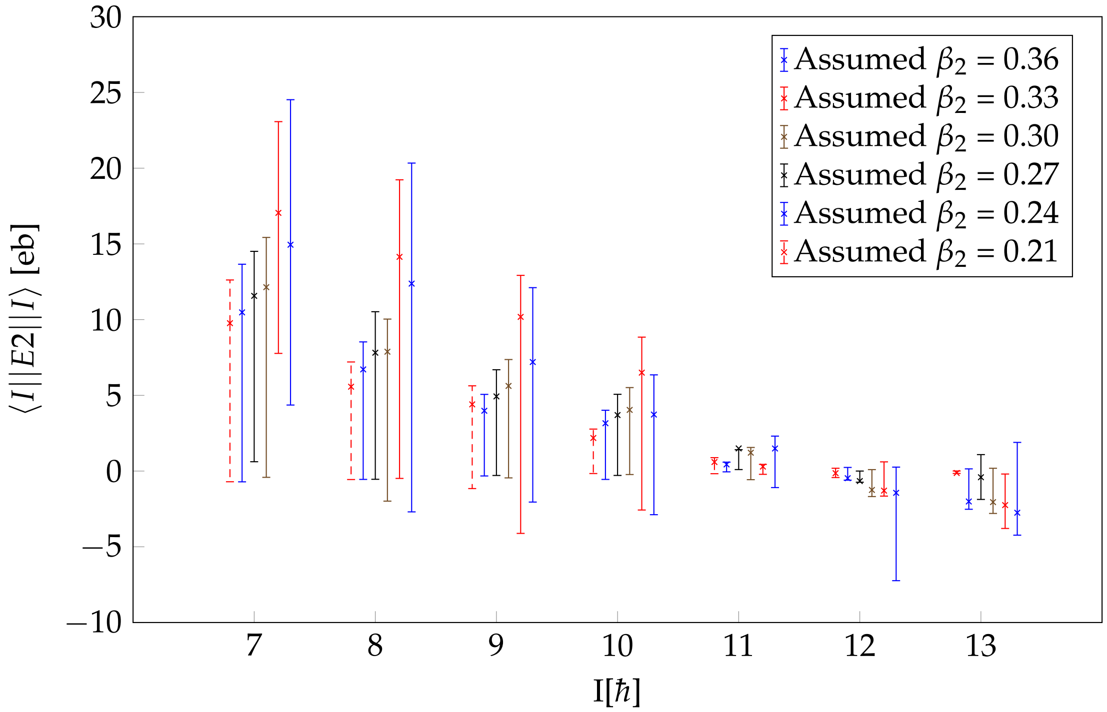


FIGURE 5.39: Similar to Figure 5.37 but for diagonal matrix elements

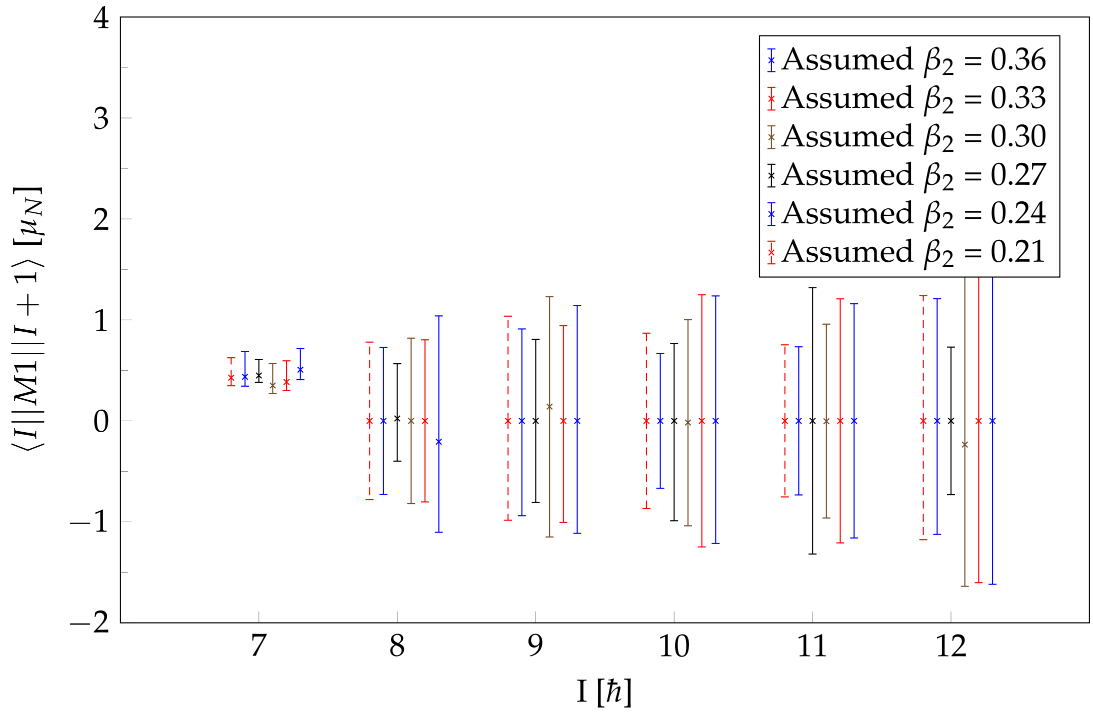


FIGURE 5.40: Similar to Figure 5.37 but for M1 matrix elements

tests converged with the chi-squared value ($S$ in equation 3.33) that fluctuates in a very small range as $S_{min}$ = 0.30557 at assumed $\beta_2$ = 0.21 to $S_{max}$ = 0.313253 at $\beta_2$ = 0.30. The results from different test, within the error, are consistent, and their chi-squared value are almost the same, show that the fit of these test converged in to a same minimum.

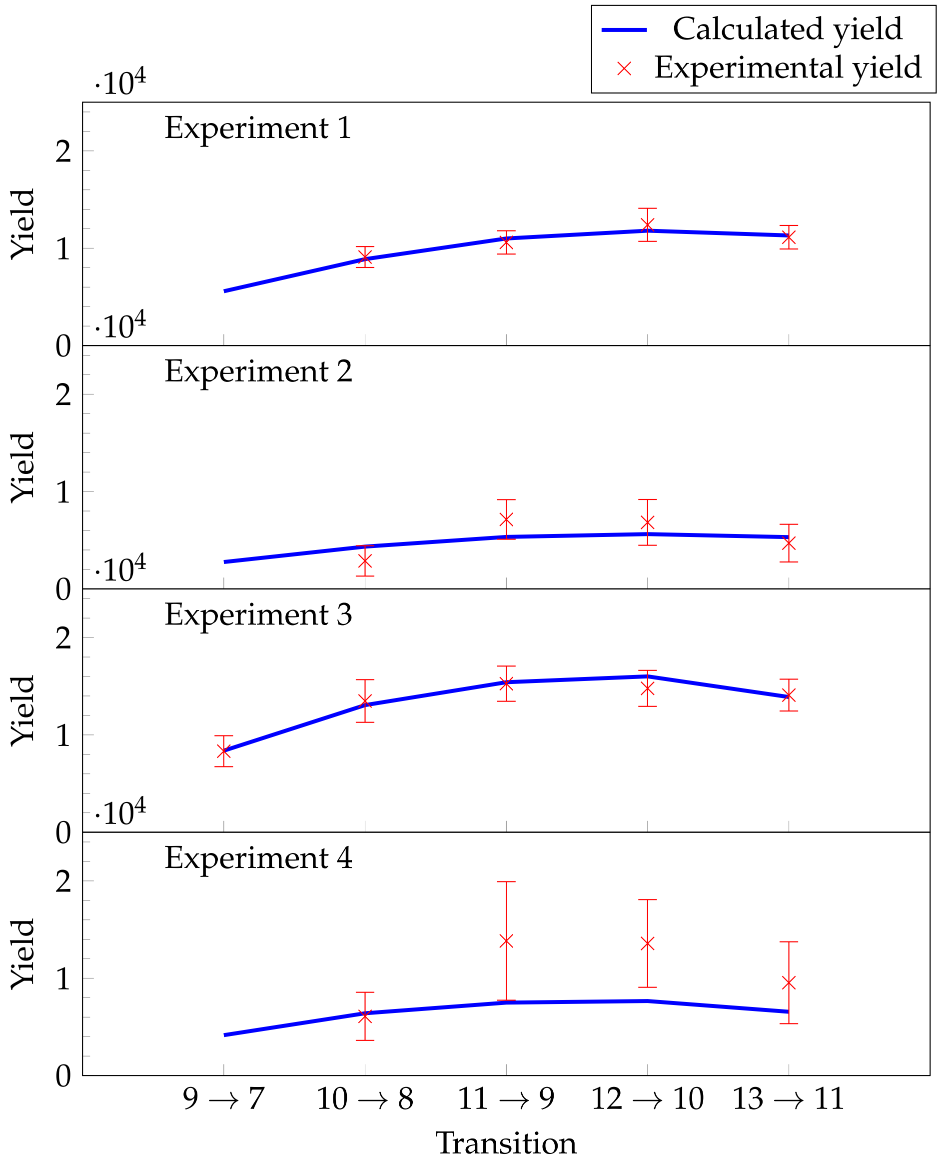


FIGURE 5.41: $\gamma$-ray yield results from GOSIA fit compare to the experimental yields for different ***experiment***. The experimental yields with corresponding scattering angle and detector group of each ***experiment*** are tabulated in Table 5.7. The calculated $\gamma$-ray yields are from the solution with assumed $\beta_2$ = 0.24.

Figure 5.41 shows the comparison between the experimental and the calculated $\gamma$-ray yields for the 4 different data-sets (***experiment(s)***) listed in Table 5.7. The yields calculated from the GOSIA solution with initial assumed $\beta_2$ = 0.24 are shown by the blue lines in Figure 5.41.

In additional, GOSIA also provides the calculated $\gamma$-ray yields of the $\Delta$I = 1 transitions that were not observed in $\gamma$-ray spectrum. Figure 5.42 shows the level schemes with the calculated $\gamma$-ray intensities corresponding to ***experiment*** 1 and 3 deduced from the GOSIA solution with initial assumed $\beta_2$ = 0.24.

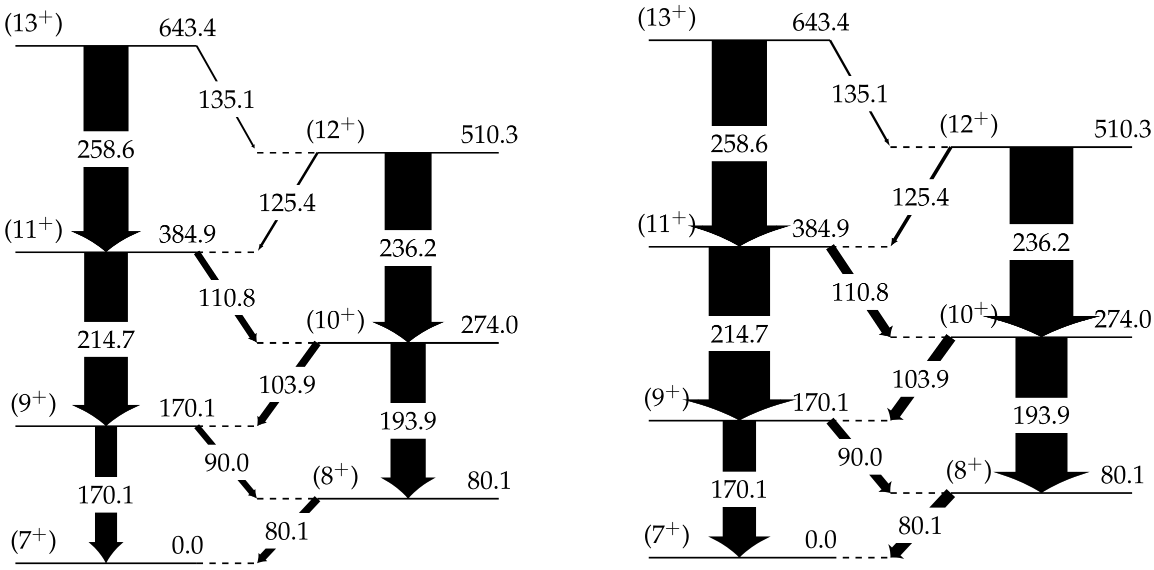


(a) ***experiment*** 1 (b) ***experiment*** 3

FIGURE 5.42: Calculated level scheme of the ground-state rotational band of $^{254}$Es where the $\gamma$-ray intensities correspond to those calculated by GOSIA. Note that internal conversion is not included. The width of the arrows is proportional to the intensity of $\gamma$-ray transition that are deduced from GOSIA solution with assumed $\beta_2$ = 0.24. The intensity are shown HPGe detectors at two different scattering angles (as ***experiment*** 1 (a) and ***experiment*** 3 (b) in Table 5.7). See text for further details.

The $\gamma$-ray yield of the $\Delta$I = 1 transitions (as shown in Figure 5.42) were estimated to be significantly smaller than the $\Delta$I = 2 transitions. The small $\Delta$I = 1 transition intensities are due to the very large internal conversion coefficient ($\alpha_{IC}$). For example, the 80.1keV ($8^+ \rightarrow 7^+$) transition has internal conversion coefficients for E2 and M1 multipolarity of $\alpha_{IC}(E2)$ = 68.5 and $\alpha_{IC}(M1)$ = 18.0, respectively [56]. With the mixing ratio $\delta_{E2/M1}$ = 1.25, the total internal conversion coefficient is $\alpha_{IC}$ = 37.71 [56]. This value of $\alpha_{IC}$ is ten times larger than the $\alpha_{IC}$ = 3.29 [56] for the 170.1 keV ($8^+ \rightarrow 7^+$).

The $\Delta$I = 1 transitions were not observed in the $\gamma$-ray spectrum because of the low $\gamma$-ray yield and low detection efficiency. For example, the highest yield 80.1 keV

($8^+ \rightarrow 7^+$) and lowest yield 135.1 keV ($13^+ \rightarrow 12^+$) transitions, deduced from the GOSIA solution with an initial assumed $\beta_2$ = 0.24, are estimated to have only about 26 and 10 counts, respectively, in the sum spectrum of all HPGe detectors for angular range from 142.98° to 157.83° (as shown in Table 5.7 **experiment** 1). Instead, for the E2 transitions, a few hundred counts are predicted and were indeed observed in the $\gamma$-ray spectrum as shown in Fig. 5.31. The observed $\gamma$-ray peak counts and the efficiency corrected intensities are listed in Table 5.7. Indeed, inspection of this spectrum reveals faint indications of peaks at energies near 80 and 90 keV. However, the estimated counts of ΔI = 1 transitions are not significantly larger than the background level, and it makes difficult to identify these peak in the spectrum. The small number of counts estimated by the GOSIA calculation are consistent and compatible with our data. Moverover, the energy of several ΔI = 1 transitions coincide with $^{254}$Es X-rays energy, and it is difficult to resolve from them.

TABLE 5.8: Magnitude of the matrix element of E2 (($7^+$) $\rightarrow$ ($9^+$)) transitions from the GOSIA solution of different set of initial values, which assumed from different quadrupole deformation.

| Assumed $\beta_2$ | $\langle 7^+ \| E2 \| 9^+ \rangle$ eb | | |
|---|---|---|---|
| 0.21 | 3.05 | -0.58 | +0.79 |
| 0.24 | 2.94 | -0.50 | +0.67 |
| 0.27 | 2.80 | -0.86 | +0.55 |
| 0.30 | 2.83 | -0.95 | +0.96 |
| 0.33 | 2.81 | -0.63 | +0.80 |
| 0.36 | 3.14 | -0.65 | +0.81 |

From the results of matrix elements E2($I \rightarrow I+2$), the deformation of $^{254}$Es at the state $I$ can be deduced using Equations 2.21 and 2.25. Figure 5.43 shows the quadrupole deformation of $^{254}$Es in the ground-state and excited states. The deformation values are deduced from the GOSIA solution with assumed $\beta_2$ = 0.24. The

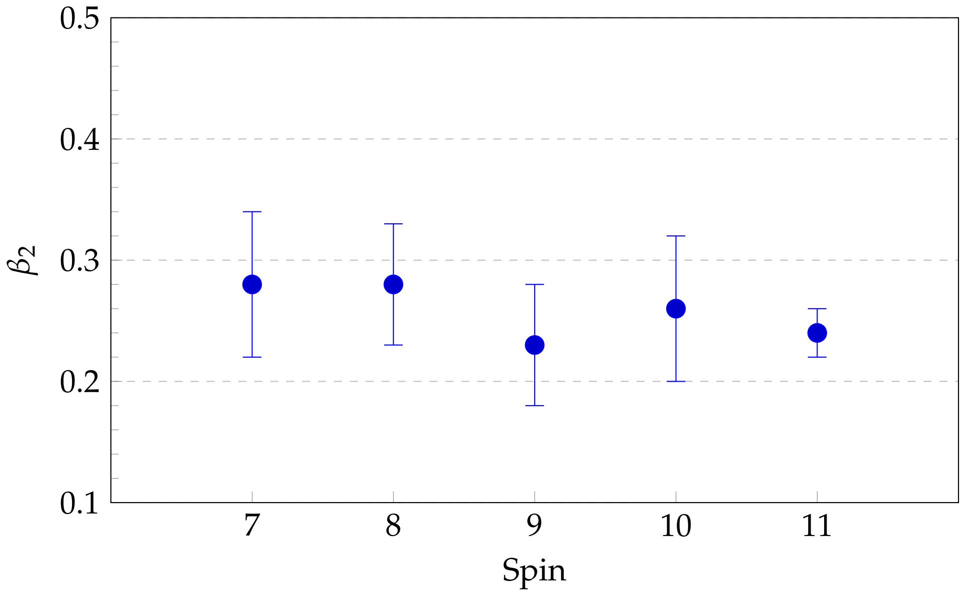


FIGURE 5.43: The quadrupole deformation of $^{254}$Es as function of spin. The deformation values are deduced from the results of matrix elements E2($\Delta$I = 2) from the solution with assumed $\beta_2$ = 0.24, using Equations 2.21 and 2.25.

deformation values, within the error bar, are nearly constant and do not show any clear increasing or decreasing trend.

To deduce the quadrupole deformation at the ground state of $^{254}$Es, the magnitude of the E2 matrix element of the transition $(7^+) \rightarrow (9^+)$ is needed. The final result is chosen to the solution with the smallest error of the matrix element of the E2($(7^+) \rightarrow (9^+)$) transition, which corresponds to the initial assumption $\beta_2$ = 0.24. The magnitude of the matrix element of E2 ($(7^+) \rightarrow (9^+)$) transitions from the GOSIA solution of different sets of initial values that were assumed from different quadrupole deformation are tabulated in Table 5.8. The difference between solutions is considered as an additional systematic error, and is calculated as in the equations 5.10 below.

$$\begin{aligned} \sigma_-^{sys} &= |\overline{x} - x_{min}|, \\ \sigma_+^{sys} &= |\overline{x} - x_{max}|, \end{aligned} \tag{5.10}$$

where $\overline{x}$ is the central value of the matrix element of the E2 ($(7^+) \rightarrow (9^+)$) transitions in the solution corresponding to the initial assumption $\beta_2$ = 0.24, while $x_{min}$ and $x_{max}$ are the smallest and largest ones among solutions. The overall uncertainty is calculated as:

$$\sigma_{\pm} = \sqrt{(\sigma_{\pm}^{sys})^2 + (\sigma_{\pm}^{stat})^2}. \tag{5.11}$$

The final result of the matrix element of the E2($(7^+) \rightarrow (9^+)$) transition to be $2.94^{+0.70}_{-0.52}$ eb. Using Equations 2.21 and 2.25, the transitional electric quadrupole moment and the quadrupole deformation of $^{254}$Es in the ground state are extracted to be $Q_0 = 12.2^{+2.9}_{-2.1}$ eb and $\beta_2 = 0.28^{+0.07}_{-0.05}$, respectively.

## Summary

In summary, the $\gamma$-ray spectroscopy and the GOSIA calculation have been described for the $^{254}$ Es Coulomb excitation experiment. Several new $\gamma$-ray transitions are observed and are assigned to be the members of $^{254}$Es ground-state rotational band. A level scheme, which includes newly observed transitions with corresponding assigned spin-parity and the extracted intensities from the $\gamma$-ray spectrum, was built. The GOSIA calculation was used to deduce the matrix elements involved in the Coulomb excitation experiment of $^{254}$Es using newly assigned $\gamma$-ray transitions. From the extracted E2 matrix element of $(7^+) \rightarrow (9^+)$ by the GOSIA calculation, the quadrupole deformation of $^{254}$Es was deduced. The results of new transitions and deduced matrix elements will be discussed in the next chapter.

# Chapter 6

# Discussion

In this chapter, the results of the Coulomb-excitation $\gamma$-ray spectroscopy of $^{254}$Es will be discussed and compared to the neighboring nuclei. In the first section, the discussion will focus on the calculated moment of inertia. The deformation of $^{254}$Es, deduced from the ground-state band energies will be examined and compared to the systematics of the region in Section 6.2. Section 6.3 presents the results of recent theoretical calculations that were performed for $^{254}$Es. Furthermore, very recent experimental results obtained from laser spectroscopy will also be introduced and compared to our experimental result. The last section discusses the assignment of ground-state single-particle orbitals configuration of $^{254}$Es, in the light of the quadrupole deformation determined in this work.

## 6.1 Moment of Inertia

In this experiment, seven transitions of the ground-state band of $^{254}$Es were observed, from $(9^+) \rightarrow (7^+)$ to $(15^+) \rightarrow (13^+)$. The spin of the states of the g.s. band were assigned using the $E_{rot} \propto I(I+1)$ rule as presented in Section 5.3.2. Furthermore, the search of the K quantum number with the minimum Chi-square indicates K = 6 or 7 as the most likely K value for the band, which further supports the correctness of our assignments. From the transition energies and spins, the kinematic and dynamic moments of inertia $\mathscr{I}^{(1)}$ and $\mathscr{I}^{(2)}$ of the ground-state band of $^{254}$Es can be calculated with equations 2.17 and 2.18. The moments of inertia of $^{254}$Es against the rotational frequency $\omega$ are plotted in figure 6.1. In the same figure, the moments of inertia of $^{252}$Cf are given for comparison. They are calculated from transition energies and spins published in Refs [57, 58].

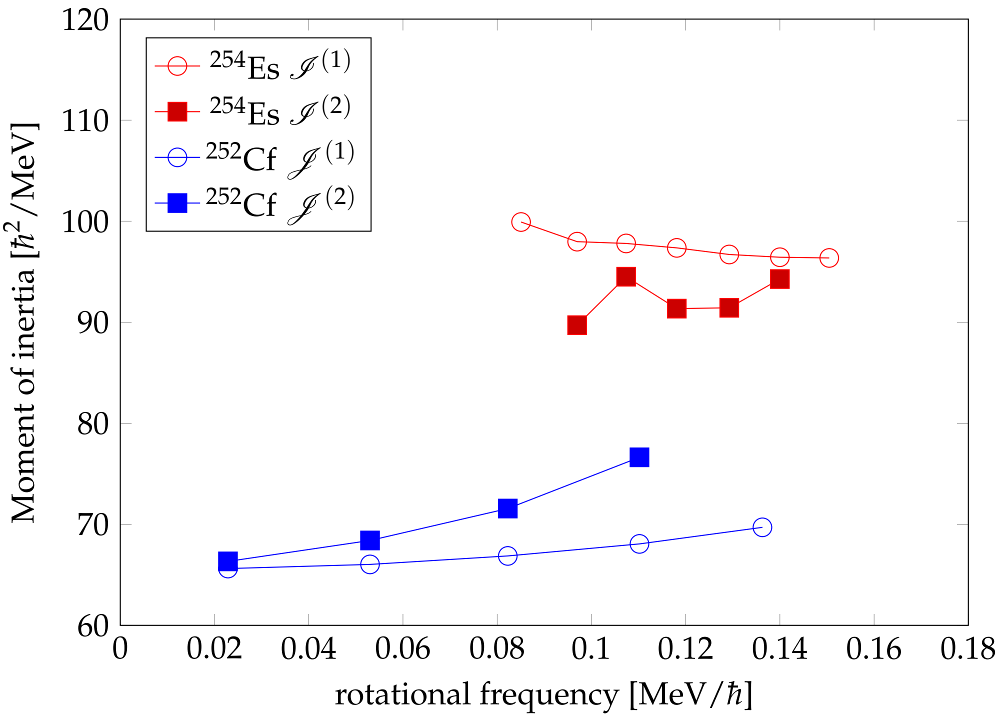


FIGURE 6.1: Kinematic and dynamic moment of inertia of the ground-state rotational band of $^{254}$Es.

As shown in figure 6.1, the kinematic moment of inertia of the ground-sate band of $^{254}$Es $\mathscr{I}$ = 99.92 $\hbar^2$ / MeV (defined as $\mathscr{I}$ value calculated from the first $\Delta$I =2 transition) is significantly larger than that of the neighboring even-even nucleus $^{252}$Cf $\mathscr{I}$ = 65.62 $\hbar^2$/MeV. One needs to examine therefore whether such an increase is due to a sharp change in global nuclear properties like the amount of quadrupole deformation, or whether this increase can be traced back to the contribution of individual nucleons.

In several cases, the kinematic moment of inertia in odd-odd nuclei were found to be systematically larger than those of the ground-state bands of neighboring even-even nuclei [59]. First of all, one needs therefore to examine whether the difference in the moment of inertia between $^{254}$Es and $^{252}$Cf can be described in terms of the contribution of the last unpaired neutron and protons, using the relation:

$$\delta\mathscr{I}(\Omega_n,\Omega_p) \approx \delta\mathscr{I}(\Omega_n) + \delta\mathscr{I}(\Omega_p). \tag{6.1}$$

where $\delta(\Omega_n)$ and $\delta(\Omega_n)$ depend on the specific orbital occupied by each valence neutron or proton, respectively. Empirically, these quantities are normally determined from the corresponding configuration in the neighboring odd-A nucleus. An example interpretation of the moment of inertia of odd-odd nuclei ${}^{166}_{67}\mathrm{Ho}_{99}$, by Bohr and Mottelson in Ref. [59], p.121, shows a satisfactory agreement.

The guessed ground-state configuration of ${}^{254}$Es consists in the coupling of a proton in the $h_{11/2}$ 7/2[633] with a neutron in the $i_{13/2}$ 7/2[613] orbital. This assignment was based on the systematics and has not yet been confirmed, due to the poor knowledge of the underlying single-particle orbitals in heavy nuclei. In the following, the additive contribution $\delta\mathscr{I}_p$ in the proton orbit 7/2[633] and $\delta\mathscr{I}_n$ in the neutron orbit 7/2[613] are determined from the corresponding configuration in odd-proton nucleus ${}^{251}$Es and the odd-neutron nucleus ${}^{253}$Cf, respectively.

The reason why ${}^{251}$Es was chosen instead of the neighboring ${}^{253}$Es is that the experimental data on ${}^{253}$Es appear not to be reliable. For example, the first $\Delta I$=2 transition of the g.s. band was not observed, and its energy was indirectly deduced from $\alpha$-decay energy data with a large uncertainty: 80(8) keV. The corresponding moment of inertia calculated from this transition results to be 25% larger than that of ${}^{254}$Es, while the logic suggests that it should be smaller. Therefore, the better known state energies and spins of the $\pi$ 7/2[633] band in ${}^{251}$Es were used instead. The resulting $\delta\mathscr{I}_p$ for the proton orbit 7/2[633] in ${}^{251}$Es is $\delta\mathscr{I}_p$ = $\mathscr{I}({}^{251}_{99}\mathrm{Es}_{152})$ - $\mathscr{I}({}^{250}_{98}\mathrm{Cf}_{152})$ with $\mathscr{I}({}^{251}_{99}\mathrm{Es}_{152})$ = 94.65 $\hbar^2$/MeV and $\mathscr{I}({}^{250}_{98}\mathrm{Cf}_{152})$ = 70.22 $\hbar^2$/MeV.

The value $\delta\mathscr{I}_n$ for the neutron orbit 7/2[613] in ${}^{253}$Cf is $\delta\mathscr{I}_n = \mathscr{I}({}^{253}_{98}\mathrm{Cf}_{155}) - \mathscr{I}({}^{252}_{98}\mathrm{Cf}_{154})$ with $\mathscr{I}({}^{252}_{98}\mathrm{Cf}_{152})$ = 65.62 $\hbar^2$/MeV and $\mathscr{I}({}^{253}_{98}\mathrm{Cf}_{152})$ = 73.20 $\hbar^2$/MeV. Their moments of inertia are calculated from the state energies and spins of the ground-state band taken from Refs. [58], [60].

In summary, these empirical estimates yield $\delta\mathscr{I}_p$ = **24.43** $\hbar^2$/MeV and $\delta\mathscr{I}_n$ = **7.58**

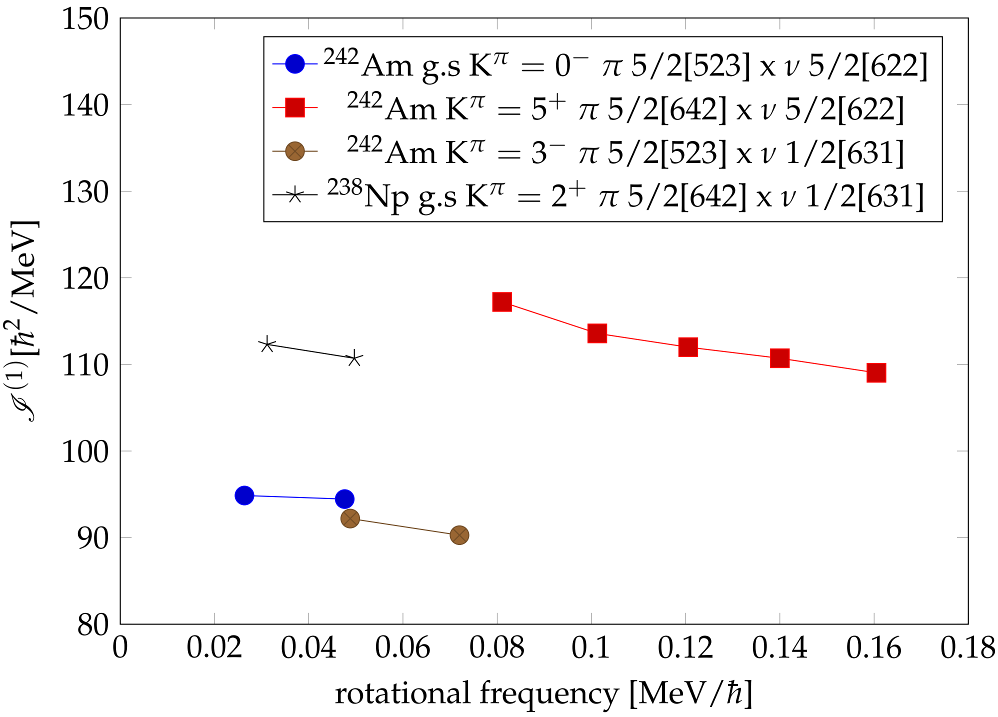


FIGURE 6.2: Experimental kinematic moment of inertia $\mathscr{I}^{(1)}$ of the rotational bands of odd-odd nuclei $^{242}$Am and $^{238}$Np with the same decreasing trend as $^{2}$54Es. The experimental data are taken from Refs. [61], [62].

$\hbar^2$ / MeV, respectively, resulting in a total expected the total increase of $\delta\mathscr{I}$ = **32.01** $\hbar^2$/MeV. The observed increment $\delta\mathscr{I} = \mathscr{I}(^{254}_{99}\text{Es}_{155}) - \mathscr{I}(^{252}_{98}\text{Cf}_{154})$ = **34.30** $\hbar^2$/MeV is very close to the calculated value. This close match in turn strongly suggests that the difference between the moment of inertia of $^{254}$Es and $^{252}$Cf is mainly due to the contribution of the two unpaired nucleons. In turn, if $^{254}$Es can be described as a deformed $^{252}$Cf core plus one neutron and one proton, it means that the ground-state deformation of $^{254}$Es can be expected to be very similar to that of $^{252}$Cf. The discussion of the ground-state deformation of $^{254}$ Es in the heavy actinide region deformation will be given in Section 6.2.

In addition to the absolute value of the moment of inertia, it is also interesting to consider how it changes as higher spin states are populated. The kinematic moment of inertia of $^{254}$Es and $^{252}$Cf are plotted in Figure 6.1 versus the rotational frequency $\omega$. While the moment of inertia of $^{252}$Cf exhibits the increasing trend, that of $^{254}$Es decreases with higher rotational frequencies. Indeed, in most even-even nuclei and

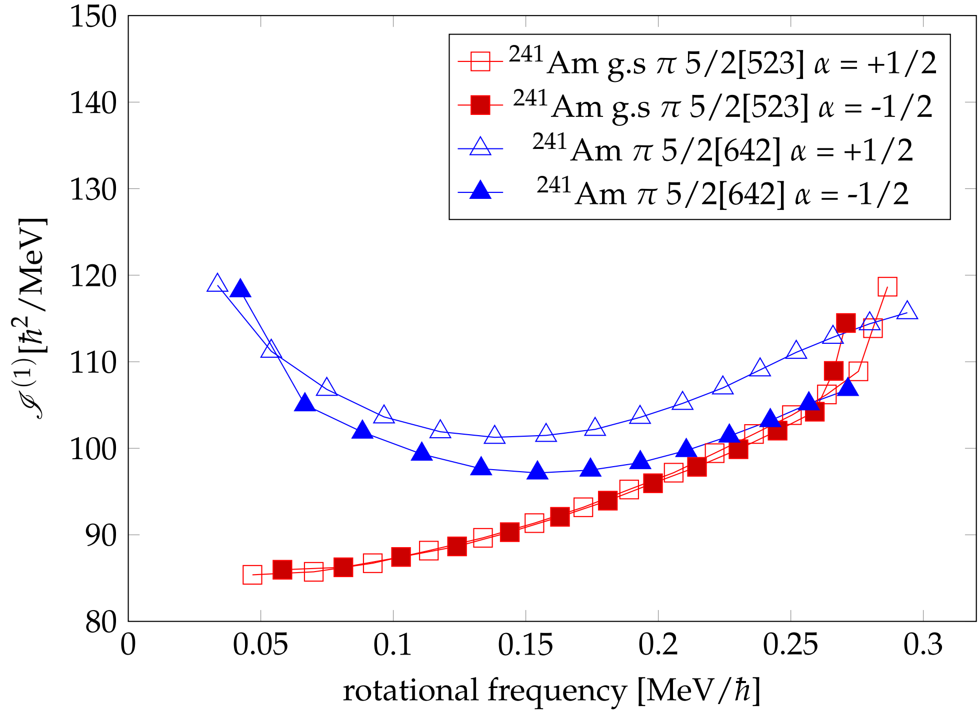


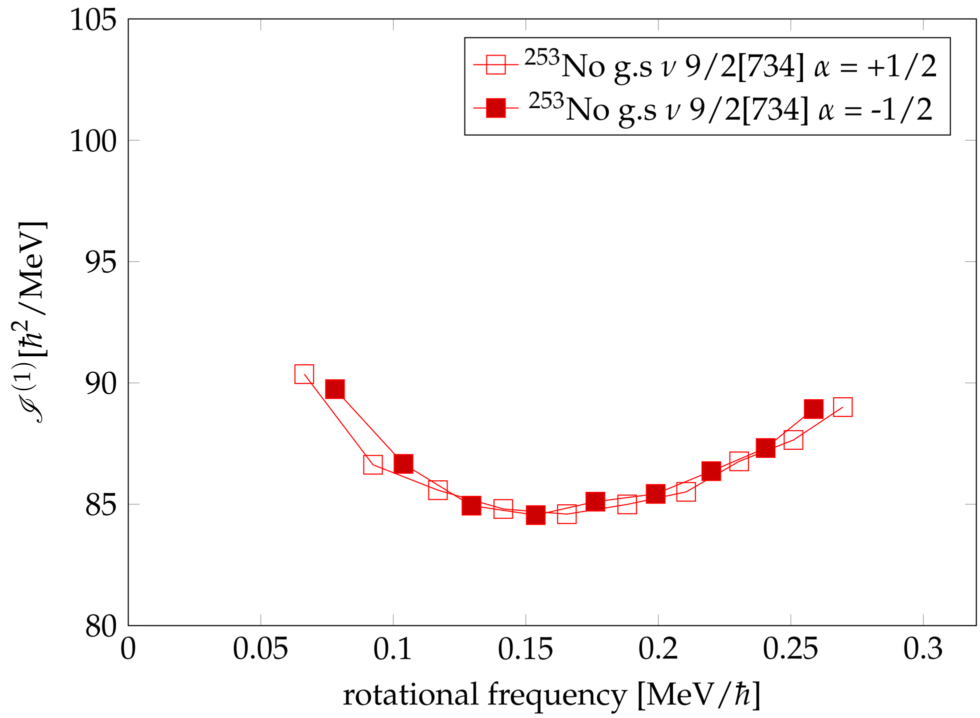


FIGURE 6.3: Experimental kinematic moment of inertia $\mathscr{I}^{(1)}$ of the rotational bands of odd-proton $^{241}$Am and odd-neutron $^{253}$No. The experimental data taken from Refs. [63], [64].

odd-A nuclei, the kinematic moment of inertia normally increases with $\omega$. This is usually explained by two factors: the first is that the faster rotation induces a small increase in deformation, which leads to a larger moment of inertia; in addition, rotational motion, via the Coriolis force, competes with the pairing force, and a reduction of pairing is equivalent to making the nucleus more rigid, increasing the moment of inertia.

The decreasing trend of moment of inertia in $^{254}$Es, although rare, is not unique. In the actinide region, several odd-A and odd-odd nuclei exhibit a decreasing trend of the moment of inertia at low spins. Examples are found in odd-odd nuclei like $^{242}$Am and $^{238}$Np (shown in Fig. 6.2) and odd-A nuclei like $^{241}$Am and $^{253}$No (shown in Fig. 6.3).

A possible explanation for the decreasing trend of the moment of inertia at low frequencies in odd actinides is the link to the occupation of high-j orbitals by the last unpaired nucleon(s). The occupation of a high-j orbital results in a "blocking" effect, by which the unpaired nucleon is less likely to participate in pair breaking or pair formation as rotational frequency increases. This effect impacts the nucleons' alignment with the rotational axis, leading the moment of inertia to increase more slowly or even decrease as the rotational frequency increases. The blocking effect is dominant at low frequency. As the nuclei spin faster, the global effect induced by the rotational motion prevails and eventually leads to an increasing trend.

For example, the moments of inertia of $^{241}$Am $\pi 5/2[642]$ band and of $^{253}$No ground-state band $\nu 9/2[734]$ initially decrease and then increase again after reach minimum at $\omega \approx 0.15$ MeV/$\hbar$. The number of states populated in $^{254}$Es permits to map the evolution of its kinematic moment of inertia only up to a frequency of $\sim 0.15$ MeV/$\hbar$. Most likely, the moment of inertia of $^{254}$Es can also be expected to change to an increasing trend at higher frequencies.

The behavior of the moment of inertia with rotational frequency is consistent with the interpretation that the unpaired nucleons occupy high-j orbitals. The sensitivity of the moment of inertia to the specific orbitals occupied by the nucleons is what makes this kind of study essential to obtain a more precise mapping of the single-particle orbits in the region.

One of the most notable experimental results that Coulomb excitation provide is the determination of the ground-state deformation. This will be described in the next section, as well as the comparison with theoretical predictions of the ground-state deformation of $^{254}$Es.

## 6.2 Ground-state deformation of $^{254}$Es

As already presented in Section 5.4, the quadrupole deformation of $^{254}$Es deduced from the lowest E2(ΔI=2) transition matrix element is $\beta_2 = 0.28^{+0.07}_{-0.05}$. This result is presented together with the quadrupole deformation of neighboring even-even actinide isotopes of Pu, Cm and Cf in Fig. 6.4. The deformation determined in this work has a magnitude consistent with neighboring actinides. Despite the large uncertainty, mainly due to the statistical limitations caused by the tiny amount of highly radioactive target material, the measured value supports the view of a nearly constant quadrupole deformation in this region. In turn, this is consistent with the interpretation of the moment of inertia discussed in Section 6.1, and supports the description of odd-odd $^{254}$Es as a $^{252}$Cf core plus one proton and one neutron.

At this stage, it also seems worth mentioning the results of a very recent laser spectroscopy experiment, which was carried out roughly at the same time as my research. In the experiment, which was carried out at RISIKO mass separator in Mainz, Germany, the hyperfine structure of $^{253-255}$Es was studied and led to the assignment of a spin value of 7 for the ground state of $^{254}$Es. Also, the spectroscopic electric quadrupole moment of $^{254}$Es was determined to be $Q_s$ = 9.6(1.2) eb. Taking their result, it is possible to calculate the intrinsic quadrupole moment using equation 2.23 with K = I = 7 for ground-state band, results in $Q_0(^{254}\text{Es})$ = **14.3(1.8)** eb. Subsequently, using equation 2.25, the quadrupole deformation of $^{254}$Es is deduced to be $\beta_2$ = **0.33(4)**. This result, within the error, is consistent with the result of deformation of $^{254}$Es from this work. Also, given that these are two independent results, it is also possible to take a weighted

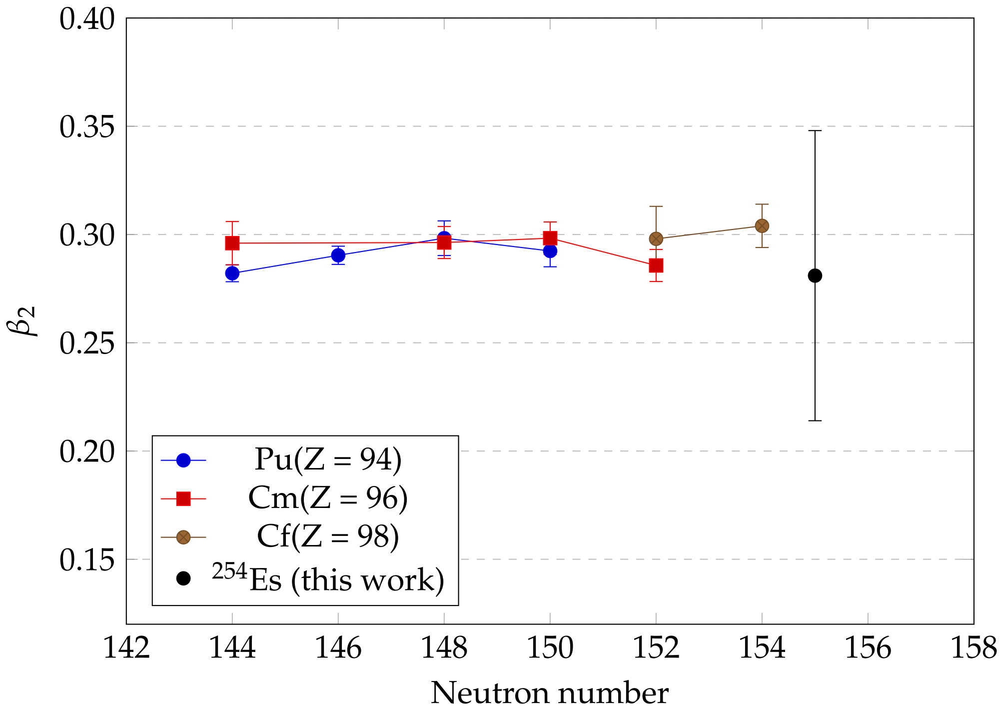


FIGURE 6.4: The quadrupole deformation $\beta_2$ of $^{254}$Es obtained in this work in comparison with the adopted $\beta_2$ values for neighboring even-even isotopes of Pu, Cm, Cf [24].

average. By approximating our uncertainty to a symmetric $\sigma$ of 0.06, the weighted average is $\beta_2 =$ **0.315(24)**.

## 6.3 Comparison with recent theoretical calculation

A theoretical calculation of the deformation and rotational properties of $^{254}$Es was recently made by A.V. Afanasjev (Department of Physics and Astronomy, Mississippi State University, USA) using the cranked relativistic Hartree-Bogoliubov (CRHB) theory and Lipkin-Nogami method with NL1 parametrization [65].

The kinematic moment of inertia and transition quadrupole moments were calculated. The theoretical moment of inertia is plotted together with the experimental data in Fig. 6.5. The calculated moment of inertia also exhibits the decreasing trend of the kinematic moment of inertia, although the calculated values are smaller than the experimental data. This underestimation is most likely due to an overestimation of the pairing strength in the calculation.

The calculated transition quadrupole moment is almost constant with a slight increase with rotational frequency: $Q_0$ = 13.25 eb at $\omega$= 0.02 MeV, and $Q_0$ = 13.40 eb at $\omega$ = 0.16 MeV. The average value is $Q_0$=13.33 eb. The corresponding quadrupole deformation is $\beta_2$ = 0.306 at $\omega$ = 0.02 MeV and $\beta_2$ = 0.308 at $\omega$ = 0.16 MeV, and the average value is $\beta_2$ = 0.307.

The calculated $\beta_2$ , the $\beta_2$ determined in this work and the $\beta_2$ deduced from the recent laser spectroscopy experiment are plotted in Fig. 6.6 together with the quadruple deformation of neighboring isotopes. The theoretical value follows the systematics and is very close to the weighted average obtained from the two experimental results. This good match supports the goodness of our measurement. By fixing the quadrupole deformation, this result also corroborates our interpretation of the ground-state configuration of $^{254}$Es and the identification of high-j orbitals in the Fermi level of this nucleus.

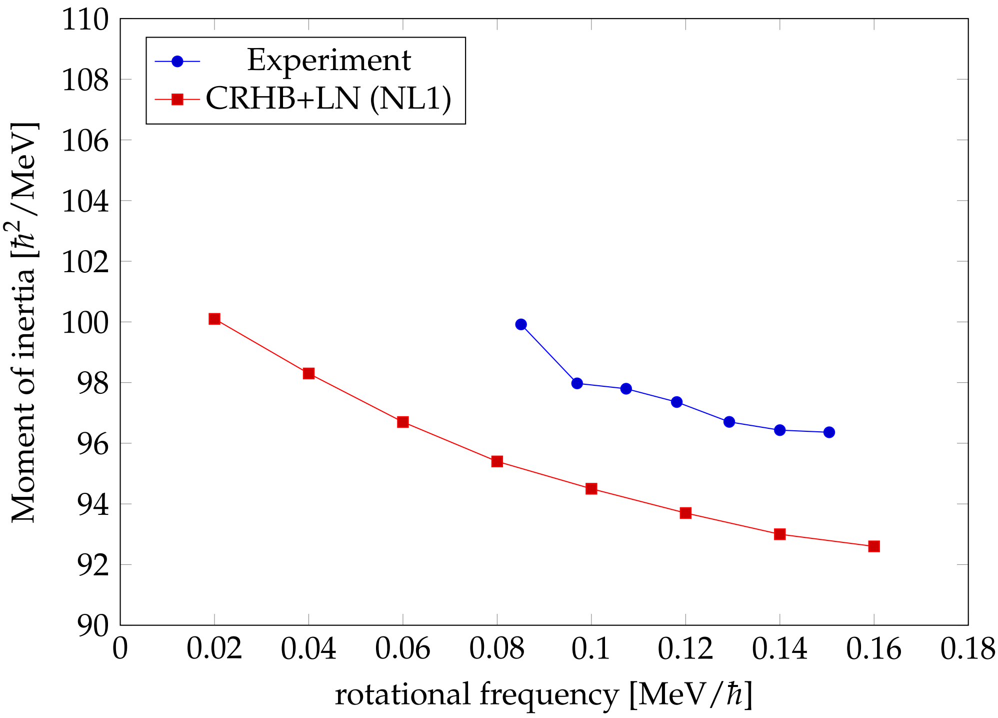


FIGURE 6.5: The moment of inertia of $^{254}$Es calculated with cranked relativistic Hartree-Bogoliubov theory in comparison with the experimental data.

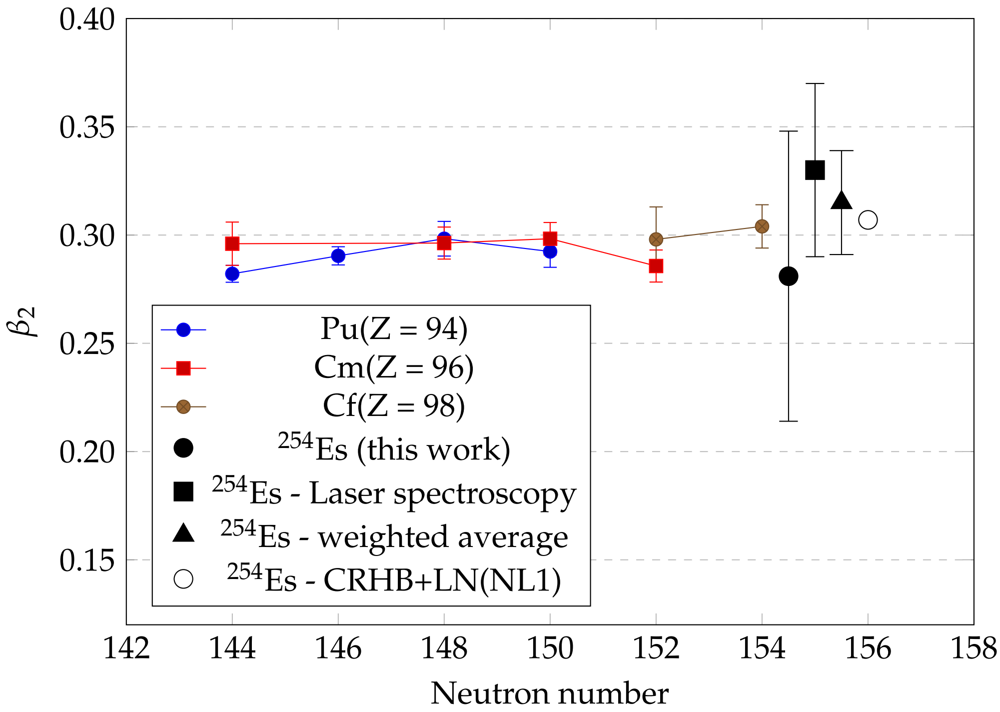


FIGURE 6.6: The result of quadrupole deformation $\beta_2$ of $^{254}$Es from this work and in comparison with result deduced from laser spectroscopy experiment [26] and in comparison with the adopted $\beta_2$ values for neighboring even-even isotopes of Pu, Cm, Cf [24]

## 6.4 Single-particle orbitals assignment

As mentioned in the introduction, a good mapping of the single-particle energies of high-j orbitals in the region of heavy actinides is particularly important, since the location of high-j orbits in the island of stability is strongly linked to where the next spherical shell gaps will be formed. Experimental data of state spin parity and deformation would help to improve the current knowledge of high-j orbitals in the actinide region, and is essential to obtain more reliable extrapolations to the still inaccessible IoS. In this section, from the experimental results of $^{254}$Es obtained in this work, we will try to extract information about the single-particle orbitals of $^{254}$Es.

As already mentioned before, the ground state spin of $^{254}$Es was assigned to be I=7. The quadrupole deformation of $^{254}$Es was determined to be $\beta_2 = \mathbf{0.28^{+0.07}_{-0.05}}$. Laser spectroscopy experiments yielded a value of $\beta_2$ = **0.33(4)** [27]. The weighted mean of the two independent measurement is calculated to be $\beta_2$ = **0.315(24)**. Using the knowledge of the quadrupole deformation, the single-particle orbitals of $^{254}$Es can be identified using the Nilsson diagram. In this work, the single particle energy diagram for the mass region A > 228, calculated by R. R. Chasman [23], is used. The weighted average of $\beta_2$ values, which has a smaller uncertainty, is used for this purpose.

The left panel of Figure 6.7 shows proton orbitals calculated for a momentum dependent Woods-Saxon potential plotted as a function of quadrupole deformation by Chasman et al. [23], zoomed in the Z = 100 region with quadrupole deformation $\beta_2$ = 0.2 - 0.4. As indicated in the projection at the deformation value of $\beta_2$ = 0.315 (in the right panel diagram of Figure 6.7), the 99$^{th}$ proton would be located in the high-j $i_{13/2}$ - 7/2[633] orbital and 97$^{th}$ - 98$^{th}$ pair is located in the $f_{7/2}$ - 3/2[521] orbital.

A similar plot for the neutron orbitals is shown in Figure 6.8. As shown in the diagram on the left panel of Figure 6.8, in the region of deformation $\beta_2$ = 0.315, several close-lying orbitals are located above the N = 152 energy gap. Except for the $h_{11/2}$ - 1/2[761] orbital, the other orbitals are found to be very close to each other. The orbitals ordering for at $\beta_2$ = 0.315 is shown on the right panel diagram of Figure 6.8. Following the ordering, the 155$^{th}$ neutron should occupy the $g_{7/2}$ - 1/2[620] orbital, while the

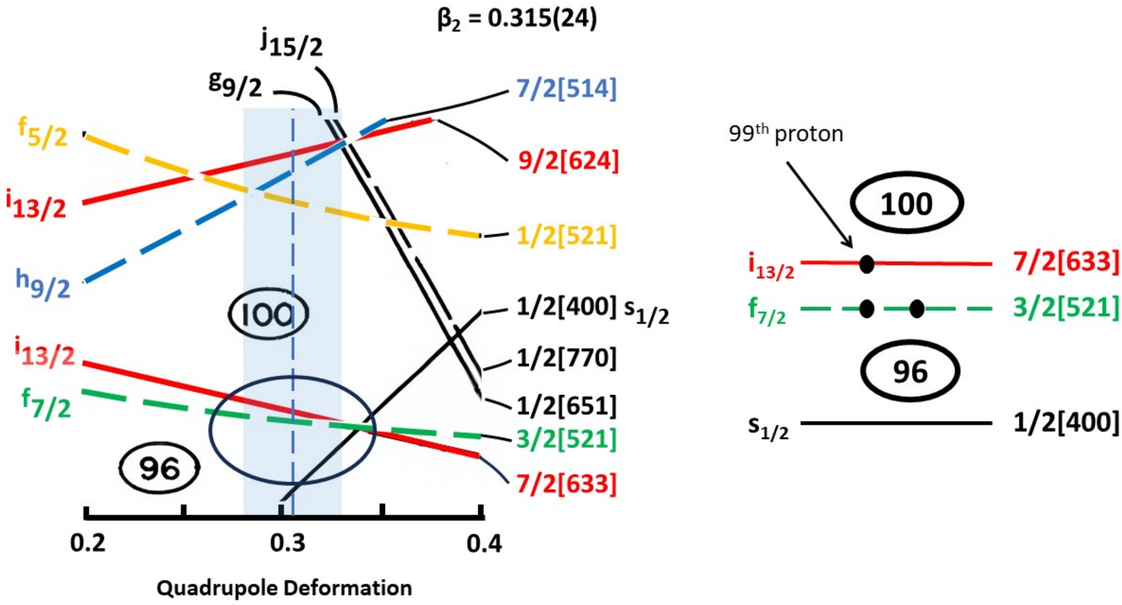


FIGURE 6.7: Left: Proton single-particle level calculated for a momentum dependent Woods-Saxon potential as a function of quadrupole deformation by Chasman et al. [23], zoomed in the Z = 100 region and quadrupole deformation $\beta_2$ = 0.2 - 0.4. The vertical, blue dashed line and the light blue shaded area surrounding it correspond respectively to the deformation value and its uncertainty $\beta_2$ = **0.315(24)**. Right: Proton single-particle orbitals for Z = 96 – 100 corresponding to $\beta_2$ = 0.315 (the black circle in the left panel, position of orbitals don't indicate their energy).

$153^{th}$ and $154^{th}$ neutron should occupy the $h_{11/2}$ - 1/2[761] orbital.

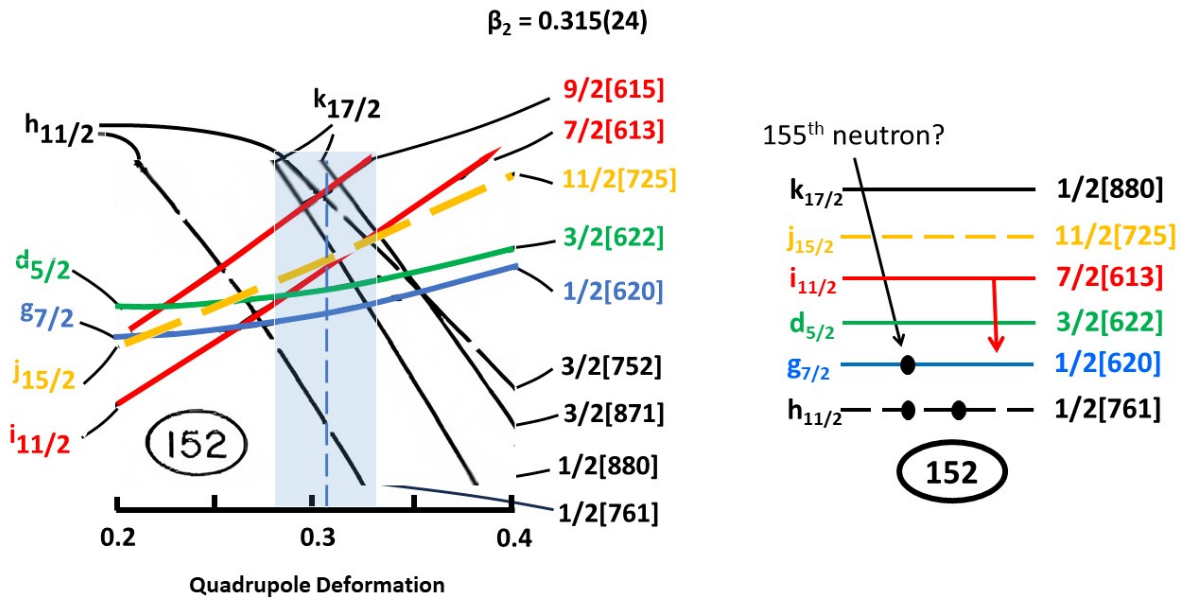


FIGURE 6.8: Left: Neutron single-particle level from momentum dependent Woods-Saxon potential as a function of quadrupole deformation [23], zoomed in the region above N = 152 energy gap and quadrupole deformation $\beta_2$ = 0.2 - 0.4. The shade blue with vertical blue dashed line indicates the deformation value and its uncertainty $\beta_2$ = **0.315(24)**. Right: Neutron single-particle orbitals in the region above N =152 energy gap corresponding to $\beta_2$ = 0.315 (position of orbitals don't indicate their energy).

It is easy to see, however, that the combination of a 7/2 proton orbital with a 1/2 neutron orbital is not compatible with a ground-state spin of 7. Knowledge of the $\beta_2$ is therefore a useful to determine the set of most likely orbitals, but care should be taken in obtaining independent tests of the correct orbital assignments. If one examines the orbitals extracted from the Nilsson diagrams near the Fermi level for a $\beta_2$=0.315, it emerges that there are only two pairs of orbitals that can couple to give a spin I = 7 ground state. The possible configuration are p 7/2[633] $\otimes$ n 7/2[613] and p 3/2[521] $\otimes$ n 11/2[725]. The latter case is however unlikely, as the n 11/2[725] configuration is not observed in any of the neighboring odd-neutron nuclei. Therefore, the most likely ground-state configuration of $^{254}$Es is p 7/2[633] $\otimes$ n 7/2[613].

With the most likely ground-state configuration of $^{254}$Es p 7/2[633] $\otimes$ n 7/2[613], the proton configuration agrees with the proton orbitals order and the placement of the $99^{th}$ shown in Figure 6.8. Also, with the proton configuration p 7/2[633], the $99^{th}$

proton occupying the $i_{13/2}$ orbital has higher angular momentum than the $f_{7/2}$ orbital occupied by the $97^{th}$ - $98^{th}$ pair. This proton placement matches the condition of the "blocking" effect, which is a possible explanation of the decreasing trend of the moment of inertia at low frequencies (as shown in Section 6.1). The neutron configuration instead does not agree with the neutron orbitals ordering and the placement of the $155^{th}$ shown in Figure 6.8. It suggests that the energy of the neutron $i_{11/2}$ - 7/2[633] orbital in the region near quadrupole deformation $\beta_2$ = 0.315 may be too high in this Chasman's calculation [23].

In summary, using the quadrupole deformation and the single particle energy diagram from Chasman's paper, the ground state configuration of $^{254}$Es was assigned. It also helps to locate the proton orbitals around Z = 100 and neutron orbitals around N = 152. There is a discrepancy of neutron orbitals location to have ground-state spin of $^{254}$Es to be 7. Moreover, in those orbitals appear near the neutron configuration of $^{254}$Es in this interpretation, the $h_{11/2}$ - 1/2[761] and $k_{17/2}$ - 1/2[880] orbitals, in some models, are associated with the N = 184 spherical shell gap, which is predicted to play an important role in the formation of the island of stability. These single-particle orbitals assignment would give some hint, even though not directly, about the location of the high-j orbits in the island of stability.

# Chapter 7

# Summary and Outlook

The nuclear structure of the heavy actinide $^{254}$Es has been studied using "safe" Coulomb excitation $\gamma$-ray spectroscopy. The ground-state band of $^{254}$Es was established up to I$^{\pi}$ = (15$^{+}$).

From the energies and spins of the ground-state band levels, the moment of inertia of $^{254}$Es was calculated, and found to exhibit a large value compared to the neighboring even-even nuclei, as well as a decreasing trend. The large moment of inertia was interpreted in terms of a deformed $^{252}$Cf core plus the individual contributions of the last odd proton and neutron. The occupation of high-j orbitals by the last unpaired nucleons was also found to be responsible for the decreasing trend of the moment of inertia as rotational frequency increases. Such a decreasing trend, although with smaller magnitude, was also predicted by recent cranked relativistic Hartree-Bogoliubov calculation.

From the yields of $\gamma$-ray transitions, in conjunction with previously measured spectroscopic data, the electromagnetic matrix elements of transitions were determined, using GOSIA. From these determined matrix elements, the quadrupole deformation is deduced to be $\beta_2 = 0.28^{+0.07}_{-0.05}$. The result of $\beta_2$ value, within the error, is consistent with the deformation deduced from the laser spectroscopy experiment and the theoretical calculation. This result fits well into the systematics of the deformation of nuclei in the heavy actinide and contributes to a more complete picture of the nuclear structure in this region.

The deformation of $^{254}$Es was obtained with quite large uncertainty due to several experimental challenges of the study of $^{254}$Es. There is very small amount of material available and the high background from $\alpha$ and $\gamma$ ray decay. Also, the $\Delta$I = 1 transitions have low energy and large internal conversion makes it difficult to observe.

To improve the results obtained, more $\gamma$-ray data as well as other spectroscopic data of $^{254}$Es such as life-time, branching ratio, mixing ratio, etc. need to be collected. More $\gamma$-ray data will help to improve the statistics and to perform $\gamma$-$\gamma$ coincidence to confirm the level scheme. The spectroscopic data and low-energy M1 transitions, if observed with sufficient statistics, will give more input data point to the GOSIA calculation.

Knowledge of the ground-state spin and deformation of $^{254}$Es not only helps to assign the configuration of $^{254}$Es but also improves the current knowledge of high-j orbitals in the actinide region. This is valuable information to promote more reliable predictions of nuclear structure on the island of stability.

Furthermore, a more accurate knowledge of single-particle energies of high-j orbitals in the region of heavy actinides and provides experimental benchmarks to test different of theoretical predictions of SHE. The study of odd-A and odd-odd nuclei, although usually complicated by a more fragmented level scheme, is particularly important because it permits to focus on the behavior of the unpaired nucleon(s) and the orbital occupied. The $\gamma$ ray spectroscopy of the odd-A heavy actinide $^{243}$Am and $^{249}$Bk are is also being considered in collaboration between Research Center for Nuclear Physics and Advanced Science Research Center, JAEA.

# List of Figures

# List of Tables

# Bibliography

[1] D Ackermann and Ch Theisen. "Nuclear structure features of very heavy and superheavy nuclei—tracing quantum mechanics towards the 'island of stability'". In: *Physica Scripta* 92 (8 May 2017), p. 83002. DOI: 10.1088/1402-4896/aa7921. URL: https://dx.doi.org/10.1088/1402-4896/aa7921.

[2] R Smolańczuk, J Skalski, and A Sobiczewski. "Spontaneous-fission half-lives of deformed superheavy nuclei". In: *Phys. Rev. C* 52 (4 May 1995), pp. 1871–1880. DOI: 10.1103/PhysRevC.52.1871. URL: https://link.aps.org/doi/10.1103/PhysRevC.52.1871.

[3] Robert Smolańczuk. "Properties of the hypothetical spherical superheavy nuclei". In: *Phys. Rev. C* 56 (2 May 1997), pp. 812–824. DOI: 10.1103/PhysRevC.56.812. URL: https://link.aps.org/doi/10.1103/PhysRevC.56.812.

[4] Sigurd Hofmann et al. "On the discovery of new elements (IUPAC/IUPAP Provisional Report)". In: *Pure and Applied Chemistry* 90 (11 2018), pp. 1773–1832. DOI: doi:10.1515/pac-2018-0918. URL: https://doi.org/10.1515/pac-2018-0918.

[5] S G Nilsson et al. "On the spontaneous fission of nuclei with Z near 114 and N near 184". In: *Nuclear Physics A* 115 (3 1968), pp. 545–562. ISSN: 0375-9474. DOI: https://doi.org/10.1016/0375-9474(68)90748-3. URL: https://www.sciencedirect.com/science/article/pii/0375947468907483.

[6] Sven Gösta Nilsson et al. "On the nuclear structure and stability of heavy and superheavy elements". In: *Nuclear Physics A* 131 (1 1969), pp. 1–66. ISSN: 0375-9474. DOI: https://doi.org/10.1016/0375-9474(69)90809-4. URL: https://www.sciencedirect.com/science/article/pii/0375947469908094.

[7] S G Nilsson, S G Thompson, and C F Tsang. "Stability of superheavy nuclei and their possible occurrence in nature". In: *Physics Letters B* 28 (7 1969), pp. 458–461. ISSN: 0370-2693. DOI: https://doi.org/10.1016/0370-2693(69)90514-0. URL: https://www.sciencedirect.com/science/article/pii/0370269369905140.

[8] Walter Mosel Ulrich and Greiner. "On the stability of superheavy nuclei against fission". In: *Zeitschrift für Physik A Hadrons and nuclei* 222 (3 May 1969), pp. 261–282. ISSN: 0939-7922. DOI: 10.1007/BF01392125. URL: https://doi.org/10.1007/BF01392125.

[9] C Y Wong. "Additional evidence of stability of the superheavy element 310126 according to the shell model". In: *Physics Letters* 21 (6 1966), pp. 688–690. ISSN: 0031-9163. DOI: https://doi.org/10.1016/0031-9163(66)90127-2. URL: https://www.sciencedirect.com/science/article/pii/0031916366901272.

[10] E Rost. "Proton shell-model potentials for lead and the stability of superheavy nuclei". In: *Physics Letters B* 26 (4 1968), pp. 184–187. ISSN: 0370-2693. DOI: https://doi.org/10.1016/0370-2693(68)90335-3. URL: https://www.sciencedirect.com/science/article/pii/0370269368903353.

[11] A Sobiczewski, F A Gareev, and B N Kalinkin. "Closed shells for Z > 82 and N > 126 in a diffuse potential well". In: *Physics Letters* 22 (4 1966), pp. 500–502. ISSN: 0031-9163. DOI: https://doi.org/10.1016/0031-9163(66)91243-1. URL: https://www.sciencedirect.com/science/article/pii/0031916366912431.

[12] Hans-Peter Duerr. "Relativistic Effects in Nuclear Forces". In: *Phys. Rev.* 103 (2 May 1956), pp. 469–480. DOI: 10.1103/PhysRev.103.469. URL: https://link.aps.org/doi/10.1103/PhysRev.103.469.

[13] T H R Skyrme. "CVII. The nuclear surface". In: *The Philosophical Magazine: A Journal of Theoretical Experimental and Applied Physics* 1 (11 1956), pp. 1043–1054. DOI: 10.1080/14786435608238186. URL: https://doi.org/10.1080/14786435608238186.

[14] D Vautherin and D M Brink. "Hartree-Fock calculations with Skyrme's interaction". In: *Physics Letters B* 32 (3 1970), pp. 149–153. ISSN: 0370-2693. DOI: https://

doi.org/10.1016/0370-2693(70)90458-2. URL: https://www.sciencedirect.com/science/article/pii/0370269370904582.

[15] D Vautherin, M Veneroni, and D M Brink. "A Hartree-Fock calculation for the stability of super-heavy nuclei". In: *Physics Letters B* 33 (6 1970), pp. 381–384. ISSN: 0370-2693. DOI: https://doi.org/10.1016/0370-2693(70)90609-X. URL: https://www.sciencedirect.com/science/article/pii/037026937090609X.

[16] Y K Gambhir, P Ring, and A Thimet. "Relativistic mean field theory for finite nuclei". In: *Annuals of Physics* 198 (1 1990), pp. 132–179. ISSN: 0003-4916. DOI: https://doi.org/10.1016/0003-4916(90)90330-Q. URL: https://www.sciencedirect.com/science/article/pii/000349169090330Q.

[17] S Ćwiok et al. "Shell structure of the superheavy elements". In: *Nuclear Physics A* 611 (2 1996), pp. 211–246. ISSN: 0375-9474. DOI: https://doi.org/10.1016/S0375-9474(96)00337-5. URL: https://www.sciencedirect.com/science/article/pii/S0375947496003375.

[18] Sigurd Hofmann. "Super-heavy nuclei". In: *Journal of Physics G: Nuclear and Particle Physics* 42 (11 May 2015), p. 114001. DOI: 10.1088/0954-3899/42/11/114001. URL: https://dx.doi.org/10.1088/0954-3899/42/11/114001.

[19] Meng Wang et al. "The AME 2020 atomic mass evaluation (II). Tables, graphs and references*". In: *Chinese Physics C* 45 (3 May 2021), p. 30003. DOI: 10.1088/1674-1137/abddaf. URL: https://dx.doi.org/10.1088/1674-1137/abddaf.

[20] *ENSDF: Evaluated Nuclear Structure Data File*. URL: https://www.nndc.bnl.gov/ensdf/.

[21] A Ghiorso et al. "Evidence for Subshell at N=152". In: *Phys. Rev.* 95 (1 May 1954), pp. 293–295. DOI: 10.1103/PhysRev.95.293. URL: https://link.aps.org/doi/10.1103/PhysRev.95.293.

[22] S G Nilsson. "Binding states of individual nucleons in strongly deformed nuclei". In: *Kong. Dan. Vid. Sel. Mat. Fys. Med.* 29N16 (1955), pp. 1–69.

[23] R R Chasman et al. “Survey of single-particle states in the mass region A > 228”. In: *Rev. Mod. Phys.* 49 (4 May 1977), pp. 833–891. DOI: 10.1103/RevModPhys.49.833. URL: https://link.aps.org/doi/10.1103/RevModPhys.49.833.

[24] B Pritychenko et al. “Erratum to “Tables of E2 transition probabilities from the first 2+ states in even–even nuclei” [At. Data Nucl. Data Tables 107 (2016) 1–139]”. In: *Atomic Data and Nuclear Data Tables* 114 (2017), pp. 371–374. ISSN: 0092-640X. DOI: https://doi.org/10.1016/j.adt.2016.08.002. URL: https://www.sciencedirect.com/science/article/pii/S0092640X16300298.

[25] K J Moody et al. “Decay properties of heavy mendelevium isotopes”. In: *Nuclear Physics A* 563 (1 1993), pp. 21–73. ISSN: 0375-9474. DOI: https://doi.org/10.1016/0375-9474(93)90010-U. URL: https://www.sciencedirect.com/science/article/pii/037594749390010U.

[26] M. Sainath, K. Venkataramaniah, and P. C. Sood. “Low-lying intrinsic structures in 254Es”. In: *European Physical Journal A* 31 (2 Feb. 2007), pp. 135–140. ISSN: 14346001. DOI: 10.1140/epja/i2006-10201-y.

[27] S Nothhelfer et al. “Nuclear structure investigations of 253-255Es by laser spectroscopy”. In: *Phys. Rev. C* 105 (2 May 2022), p. L021302. DOI: 10.1103/PhysRevC.105.L021302. URL: https://link.aps.org/doi/10.1103/PhysRevC.105.L021302.

[28] Balraj Singh. “Adopted levels, gammas for 254Es”. In: *Nucl. Data Sheets 156, 1* (2019).

[29] L. S. Goodman, H. Diamond, and H. E. Stanton. “Nuclear and atomic moments and hyperfine-structure parameters of $^{253}$Es and $^{254m}$Es”. In: *Phys. Rev. A* 11 (2 Feb. 1975), pp. 499–504. DOI: 10.1103/PhysRevA.11.499. URL: https://link.aps.org/doi/10.1103/PhysRevA.11.499.

[30] David Lawrence Hill and John Archibald Wheeler. “Nuclear Constitution and the Interpretation of Fission Phenomena”. In: *Phys. Rev.* 89 (5 May 1953), pp. 1102–

1145. DOI: 10.1103/PhysRev.89.1102. URL: https://link.aps.org/doi/10.1103/PhysRev.89.1102.

[31] Peter Ring and P Schuck. *The Nuclear Many-Body Problems*. Vol. 103. May 1980. DOI: 10.1063/1.2915762.

[32] K Alder et al. "Study of Nuclear Structure by Electromagnetic Excitation with Accelerated Ions". In: *Rev. Mod. Phys.* 28 (4 May 1956), pp. 432–542. DOI: 10.1103/RevModPhys.28.432.

[33] Kurt Alder and Aage Winther. "Electromagnetic excitation : theory of Coulomb excitation with heavy ions". In: (1975). URL: https://cir.nii.ac.jp/crid/1130000796901468032.

[34] D Cline et al. *GOSIA USER MANUAL FOR SIMULATION AND ANALYSIS OF COULOMB EXCITATION EXPERIMENTS*. 2012. URL: https://www.pas.rochester.edu/~cline/Gosia/Gosia_Manual_20120510.pdf.

[35] D Cline. "Nuclear Shapes Studied by Coulomb Excitation". In: *Annual Review of Nuclear and Particle Science* 36 (1 1986), pp. 683–716. DOI: 10.1146/annurev.ns.36.120186.003343.

[36] E Karlsson. "Angular correlation methods in gamma-ray spectroscopy: A. J. Ferguson, (North-Holland Publishing Company, Amsterdam, 1965) 230 pp., 50/-". In: *Nuclear Instruments and Methods* 37 (1965), p. 355. DOI: https://doi.org/10.1016/0029-554X(65)90395-2.

[37] D ALBURGER. "XII - GAMMA-RADIATION FROM CHARGED PARTICLE BOMBARDMENT; COULOMB EXCITATION". In: ed. by K A I SIEGBAHN. Elsevier, 1968, pp. 745–768. DOI: https://doi.org/10.1016/B978-0-7204-0083-0.50025-0.

[38] A Winther and J de Boer. "A Computer Program for Multiple Coulomb Excitation". In: *California Institute of Technology, Technical Report* (1965).

[39] *Tandem Accelerator home page*. URL: https://ttandem.jaea.go.jp/index-eng.html.

[40] *Tandem accelerator facility, Nuclear Science Research Institute, JAEA*. URL: https://www.jaea.go.jp/english/04/ntokai/kasokuki/kasokuki_04.html.

[41] Jun Chen. "Nuclear Data Sheets for A=138". In: *Nucl. Data Sheets* 146 (2017), pp. 1–386. DOI: 10.1016/j.nds.2017.11.001.

[42] *Double sided multi element circular detector - S3*. URL: http://www.micronsemiconductor.co.uk/product/s3/#.

[43] I Ahmad et al. "Two-quasiparticle states in 250Bk studied by decay scheme and transfer reaction spectroscopy". In: *Phys. Rev. C* 77 (5 May 2008), p. 54302. DOI: 10.1103/PhysRevC.77.054302. URL: https://link.aps.org/doi/10.1103/PhysRevC.77.054302.

[44] Y A AKOVALI. "Nuclear Data Sheets for A = 250, 254, 258, 262, 266". In: *Nuclear Data Sheets* 94 (1 2001), pp. 131–225. ISSN: 0090-3752. DOI: https://doi.org/10.1006/ndsh.2001.0018. URL: https://www.sciencedirect.com/science/article/pii/S0090375201900183.

[45] J K Tuli. "Evaluated nuclear structure data file". In: *Nuclear Instruments and Methods in Physics Research Section A: Accelerators, Spectrometers, Detectors and Associated Equipment* 369 (2 1996), pp. 506–510. ISSN: 0168-9002. DOI: https://doi.org/10.1016/S0168-9002(96)80040-4. URL: https://www.sciencedirect.com/science/article/pii/S0168900296800404.

[46] O.B. Tarasov and D. Bazin. "LISE++". In: *NIM B* (2008), pp. 4657–4664. URL: http://www.nscl.msu.edu/lise.

[47] Richard D. Deslattes et al. *X-ray Transition Energies (version 1.2)*. 2005. DOI: https://dx.doi.org/10.18434/T4859. URL: https://www.nist.gov/pml/x-ray-transition-energies-database.

[48] Balraj Singh. "Adopted levels, gammas for 182W". In: *Nucl. Data Sheets 130, 21* (2015).

[49] Coral M. Baglin. "Adopted levels, gammas for 184W". In: *Nucl. Data Sheets 111, 275* (2010).

[50] J. C. Batchelder and M. S. Basunian A. M. Hurst. "Adopted levels, gammas for 186W". In: *Nucl. Data Sheets 183, 1* (2022).

[51] Coral M. Baglin. "Adopted levels, gammas for 183W". In: *Nucl. Data Sheets 134, 149* (2016).

[52] Rene Brun and Fons Rademakers. "ROOT — An object oriented data analysis framework". In: *Nuclear Instruments and Methods in Physics Research Section A: Accelerators, Spectrometers, Detectors and Associated Equipment* 389.1 (1997). New Computing Techniques in Physics Research V, pp. 81–86. ISSN: 0168-9002. DOI: https://doi.org/10.1016/S0168-9002(97)00048-X. URL: https://www.sciencedirect.com/science/article/pii/S016890029700048X.

[53] S. W. Yates et al. "Particle-phonon interactions in $^{248}$Cf and $^{249}$Cf". In: *Phys. Rev. C* 12 (2 Aug. 1975), pp. 442–450. DOI: 10.1103/PhysRevC.12.442. URL: https://link.aps.org/doi/10.1103/PhysRevC.12.442.

[54] B.R. Mottelson Kgl. Danske Videnskab. Selskab. A. Bohr. "Mat.-fys. Medd." In: 16 (1953), p. 27.

[55] P. Holmberg and P.O. Lipas. "A new formula for rotational energies". In: *Nuclear Physics A* 117.3 (1968), pp. 552–560. ISSN: 0375-9474. DOI: https://doi.org/10.1016/0375-9474(68)90830-0. URL: https://www.sciencedirect.com/science/article/pii/0375947468908300.

[56] T. Kibédi et al. "Evaluation of theoretical conversion coefficients using BrIcc". In: *Nuclear Instruments and Methods in Physics Research Section A: Accelerators, Spectrometers, Detectors and Associated Equipment* 589.2 (2008), pp. 202–229. ISSN: 0168-9002. DOI: https://doi.org/10.1016/j.nima.2008.02.051. URL: https://www.sciencedirect.com/science/article/pii/S0168900208002520.

[57] R. Takahashi et al. "In-beam $\gamma$-ray spectroscopy of $^{248,250,252}$Cf by neutron-transfer reactions using a Cf target". In: *Phys. Rev. C* 81 (5 May 2010), p. 057303. DOI: 10.1103/PhysRevC.81.057303. URL: https://link.aps.org/doi/10.1103/PhysRevC.81.057303.

[58] A.M Mattera et al. “Adopted levels, gammas for 252Cf”. In: *Nucl. Data Sheets 172, 543* (2021).

[59] Aage Bohr and Ben R Mottelson. *Nuclear Structure Volume II*. World Scientific, 1997.

[60] W. Browne and J. K. Tuli. “Adopted levels, gammas for 253Cf”. In: *Nucl. Data Sheets 114, 1041* (2013).

[61] M.J. Martin and C.D. Nesaraja. “Adopted levels, gammas for 242Am”. In: *Nucl. Data Sheets 186, 261* (2022).

[62] W. Browne and J. K. Tuli. “Adopted levels, gammas for 238Np”. In: *Nucl. Data Sheets 127, 191* (2015).

[63] C.D. Nesaraja. “Adopted levels, gammas for 241Am”. In: *Nucl. Data Sheets 130, 183* (2015).

[64] W. Browne and J. K. Tuli. “Adopted levels, gammas for 253No”. In: *Nucl. Data Sheets 114, 1041* (2013).

[65] A. V. Afanasjev. “private communication”. In: ().